UNIVERSITY OF CALIFORNIA
RIVERSIDE

Magnetic Pattern Fabrication and Characterization for Next Generation
High Density Magnetic Recording System

A Dissertation submitted in partial satisfaction
of the requirements for the degree of

Doctor of Philosophy
in

Electrical Engineering

by

Beomseop Lee

March 2011

Dissertation Committee:

 Dr. Sakhrat Khizroev, Chairperson
 Dr. Roger K. Lake
 Dr. Cengiz Ozkan

The Dissertation of Beomseop Lee is approved

_____

_____

_____

Committee Chairperson

University of California, Riverside

ACKNOWEDGEMENTS

DEDICATION

I dedicate my work to my lovely family, parents, brother and all my relatives. ,I am especially grateful to Ashley (Yena) and Andrew (Himchan) for their profound understanding and support, with endless patience and tolerance,   for achieving my academic goals. I also acknowledge and appreciate everyone's sacrifice responsible for my accomplishments.

Also I want to express my full appreciation to my friend Dr. Hyri Engin Akin for his support on personal and professional levels.

Thank you, Jay Jeong and Chris Yun.

ABSTRACT OF DISSERTATION

Magnetic Pattern Fabrication and Characterization for Next Generation High Density
Magnetic Recording System

by

Beomseop Lee

Doctor of Philosophy, Graduate Program in Electrical Engineering
University of California, Riverside, March 2011
Dr. Sakhrat Khizroev, Chairperson

In this dissertation thesis, I will discuss the fundamental basic technology necessary

for continuing the prosperity status of 21st century electronic devices; Lithography. I

will give an overview of the concepts of scanning electron microscopy (SEM) and

development of direct electron beam lithography (D-EBL) for magnetic bit patterned

media (BPM), capable of achieving magnetic recording areal densities above 1

terabit/in^2. Furthermore, I will present the peripheral equipment mainly used for

developing innovative processes.

One of the main challenges in developing direct electron beam lithography technique

for fabricating magnetic bit patterned media, which I was faced with was not only to

reduce the minimum feature size below 10 nm but also to ensure an adequately small

pitch size of less than 26 nm. The latter is the critical value for the side of a square

pattern period (assuming a 1:1 bit-aspect ratio (BAR)) necessary to achieve over 1

terabit/in^2 density in hard disk industry. The main concern was to overcome the

technical limitations associated with a relatively wide electron beam tail. For instance,

according to Gaussian distribution, even a "5-nm" electron beam spot size can have a "tail" of over 50 nm because of beam scattering and secondary effect. Another limitation in the spatial resolution of EBL resulted from the interaction of the electron beam with stray magnetic fields emanating from the transitions in the BPM film under study. Throughout my research I comparatively studied a number of EBL processes, the results from which led me into selecting a lift-off based EBL process on films spin-coated with a hydrogen silsesquioxane (HSQ) negative-tone e-beam resist. Using this process, we successfully transferred large-scale square periodic arrays of nano-"dots" with a sub-13-nm diameter and a sub-26-nm pitch, as required for densities above 1 terabit-per-square-inch, into continuous magnetic films made of exchange-coupled Co/Pd perpendicular multi-layers. Furthermore, I used the same EBL process to transfer ultra-high-density patterns not only in conventional single-layer recording media but also into potentially next-generation 3-D structures consisting of several independent magnetic layers. Meanwhile, I fabricated Magnetic Force Microscopy probes for analyzing magnetic properties of nanometer size patterns. This process requires high sensitivity of the resolution and high coercivity at same time. Finally, I will discuss the results from a special magnetic force microscopy (MFM), scanning electron microscopy (SEM), Atomic Force Microscopy (AFM), focused magneto-optical Kerr Effect (F-MOKE) measurements developed to study the EBL-fabricated ultra-high-density BPM media.

Table of Contents

Figures

Tables and Graphs

Chapter 1. Introduction –
The Efforts for High Density in Electronics Devices

1. Moore's Law

Since Gordon Moore, Intel co-founder, spoke in 1965, "The number of transistors incorporated in a chip will approximately double every 24 months."[1] This well-known phrase as "Moore's Law", forecasting the trend in electronics industry, has been a fundamental business model in last 45 years industry especially in high performance technology. Over four decades passing, many highly cutting-edge industries have pushed Moore's law to its limits by achieving double the transistor density with high functional performance and decreasing costs simultaneously. Following this trend in 20th century has been made possible by downscaling device feature size, however the increasing demands for advanced technology from the market in 21st century and the continuous aggressive scaling have brought device size into the nanoscale regime, which poses a fundamental barrier for continuing this trend as device feature size approaches the atomic dimensions. Continuing Moore's Law over 45 years means that the rate of progress could spread its powers to almost all other industries as well as in the semiconductor industry and keeping the trend continuity now requires new innovative paradigm, not only in dimensions scaling for high density, but by incorporating novel materials throughout the whole integrated circuit design and by employing their unique physical and structural features. Based on the prediction (figure 1.1 and 1.2) in semiconductor field, transistor gate length is expected to reach 22 nm or less in 2011. Moreover, the physical limitation of Moore's

Law in atomic structures will be reached around 2020 [1], the same is true for "Moore's Law" with the term used outside its strict definition to describe a similar trend in the progress of memory storage, computing, networking and communication devices industries.. Therefore, it is imperative that modern scientists focus their research efforts on generating innovative means for sustaining Moore's Law.

In this dissertation, I discuss the issues that we are currently facing and the concept developed to maintain the technological trend in the hard disk technology field, and I will introduce an innovative method for achieving high density devices with various types of magnetic materials.
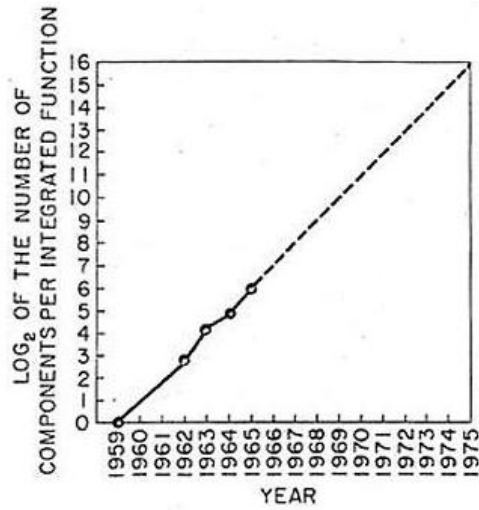
Figure 1.1: Number of components per integrated function for minimum cost per component extrapolated vs time [2]
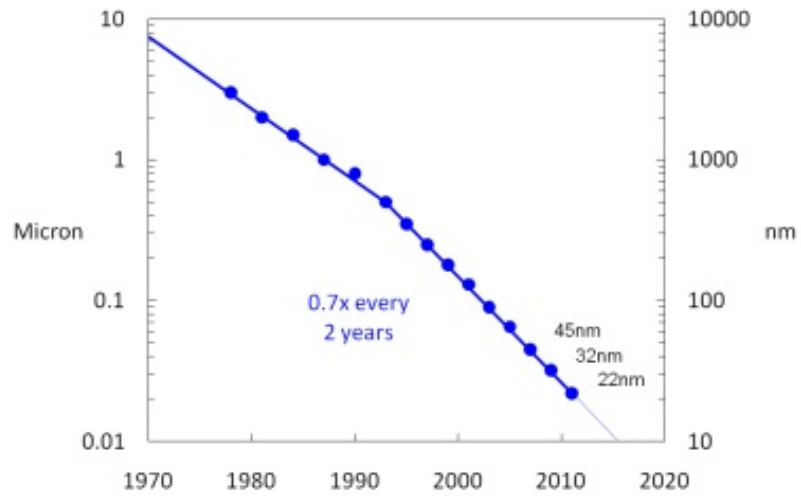
Figure 1.2: Transistor dimensions scale to improve performance, reduce power and reduce cost per transistor. (www.intel.com)

In order to continue the tendency, stated by Moore's Law, in modern electronics and information technology, I present innovative lithographic procedures which play pivotal roles in the fabrication-of advanced electronic devices; furthermore, I describe some alternative procedure methods in this dissertation. Generally, lithography is mainly focusing on reducing dot-pitch, to improve and extend the product efficiency from the optical projection technology such as ultra-violet lithography (UV-lithography), while developing other next generation concepts for when present lithography methods are no longer economically competitive with the alternative technologies. Optical projection lithography currently has occupied 193 nm wavelengths with immersion lenses, together with various novel approaches of multi-exposure methods are facing serious technical hurdles. For the improvement of lithographic ability and keeping its capability in the next generation nano-scale fabrication technology, there are several process areas, which must be innovated; discovering new resist materials and developing new processing steps, exposure equipment, mask fabrication process, next generation mask fabrication equipment and mask materials, metrology equipment for Critical Dimension (CD) measurement, overlay control and defect inspection processes and equipment, etc [3]. Despite the many challenges mentioned above, I will mainly present the tangible approaches for high density lithography by direct electron beam lithography (D-EBL), and show the performance results with Scanning Electron Microscopy (SEM) from various innovative procedures, after addressing some of the emerging problems in lithography. First, I will point out the hard disk industrial market trends and needs at the current time. Secondly, I will describe fundamental physics of electron beam performance, and explain background information such as superparamagnetic limitation, scaling

law, and new recording form; a perpendicular recording from conventional longitudinal technology and discuss the alternative technologies of performing high density; Discrete Track Recording (DTR), Heat Assistant Magnetic Recording (HAMR), and mainly Bit Patterned Media (BPM). The successful fabrication of BPM necessitates that I start my research work from polymer (resist) characterization, because there are many specific resists with different properties, which are currently used in industry and for research purposes, however, selecting the proper resist is critical for achieving high density, i.e. smallest feature size at optimal pitch.

First of all, I need to investigate various lithography process parameters. Based on my over five years experimental experiences, I reach to conclusion that the result of lithography process was very sensitive and can be affected by various factors. I will go over this topic in detail in the following chapter. In addition, I will introduce not only the performance capability of high density of magnetic storage with Bit Patterned Media (BPM) concept, but also the 3-Dimensional Magnetic Recording concept, to exponentially increase the potential of magnetic media recording with innovative fabrication procedures. Finally, I will discuss the analysis results of the achievements, from Atomic Force Microscopy (AFM), Magnetic Force Microscopy (MFM), Magneto-Optic Kerr Effect Microscopy (MOKE), and Scanning Electron Microscopy (SEM).

Year of Production	2009	2010	2011	2012	2013	2014	2015	2016	2017	2018	2019	2020	2021	2022	2023	2024
DRAM ½ pitch (nm) (contacted)	52	45	40	36	32	28	25	23	20	18	16	14	13	11	10	9
Flash ½ pitch (nm) (un-contacted poly)	37.6	31.8	28.3	25.3	22.5	20.0	17.9	15.9	14.2	12.6	11.3	10.0	8.9	8.0	7.1	6.3
MPU/ASIC Metal 1 (M1) ½ Pitch (nm) (contacted poly)	54	45	38	32	27	24	21	19	17	15	13	12	11	9	8	8
MPU physical gate length (nm) (after etch)	29	27	24	22	20	18	17	15	14	13	12	11	10	9	8	7
MPU gate ½ pitch length (nm)	47	41	35	31	28	25	22	20	18	16	14	12	11	10	9	8
Resist Characteristics *																
Resist mask requirement for gate resolution and gate CD control (nm, 3-sigma) ***=†	3.0	2.8	2.5	2.3	2.1	1.9	1.7	1.6	1.5	1.3	1.2	1.1	1.0	0.9	0.8	0.8
Resist thickness (nm, single layer) ###	80-145	70-130	60-115	55-100	50-90	45-80	40-75	35-65	30-60	25-50	25-45	20-40	20-40	15-35	10-25	10-25
EUV temperature sensitivity (nm/C)	1.5	1.5	1.5	1.5	1	1	1	1	1	1	1	1	1	1	1	1
Backside particle density (particles/cm²)	0.26	0.26	0.26	0.26	0.26	0.26	0.26	0.26	0.26	0.26	0.26	0.26	0.26	0.26	0.26	0.26
Back surface particle diameter lithography and measurement tools (nm)	100	100	100	100	75	75	75	50	50	50	50	50	50	50	50	50
Defects in spin-coated resist films (#/cm²) /†	0.01	0.01	0.01	0.01	0.01	0.01	0.01	0.01	0.01	0.01	0.01	0.01	0.01	0.01	0.01	0.01
Minimum defect size in spin-coated resist films (nm)	30	30	20	20	20	20	10	10	10	10	10	10	10	10	10	10
Defects in patterned resist films, gates, contacts, etc. (#/cm²)	0.01	0.03	0.02	0.02	0.02	0.02	0.01	0.01	0.01	0.01	0.01	0.01	0.01	0.01	0.01	0.01
Minimum defect size in patterned resist films (nm)	30	30	20	20	20	20	10	10	10	10	10	10	10	10	10	10
Low frequency line width roughness (nm, 3-sigma) <8% of CD *****	3.7	3.2	2.8	2.5	2.2	2.0	1.8	1.6	1.4	1.3	1.1	1.0	0.9	0.8	0.7	0.6
Correlation Length (nm) *******	29.2	25.8	23.3	21.4	19.6	18.6	17.0	15.5	12.5	12.8	11.5	10.2	8.3	6.9	7.9	8.9
Defects in spin-coated resist films for double patterning (#/cm2)	0.005	0.005	0.005	0.005	0.005	0.005	0.005	0.005	0.005	0.005	0.005	0.005	0.005	0.005	0.005	0.005
Backside metals density for double patterning (#/cm2)	0.14	0.14	0.14	0.14	0.14	0.14	0.14	0.14	0.14	0.14	0.14	0.14	0.14	0.14	0.14	0.14

Manufacturable solutions exist, and are being optimized

Manufacturable solutions are known

Interim solutions are known

Manufacturable solutions are NOT known

Table 1.1: International Technology Roadmap for Semiconductors (ITRS) annual report for lithography expectation [3]

6

2. Alternative Next Generation Technologies for High Areal Density – Then, Now, and Into the Future.

In this section, I will shortly mention the alternative next generation technologies for performing high areal density storage. First, Heat-Assisted Magnetic Recording (HAMR)[4] is basically similar to magneto-optical recording with controlling the magnetic energy barrier with thermal gradient. HAMR is managing the intrinsic magnetic character such as magnetization saturation (Ms), magnetic anisotropy (Ku) in materials such as FePt, and coercivity (Hc), decrease dramatically to zero when materials are heated over their Curie temperature (Tc). When writing over the heated areas, the Hc is below the writing field and loses its magnetic energy barrier and it is then rapidly cooled down to the ambient temperature when the laser heating field is removed from the heated spot. As -far as the adiabatically affected areas are larger than the local demagnetization field, the magnetization direction of each material's grains will follow the applied direction of the heat field. The most pronounced difference between optical recording and HAMR is that in the latter method magneto resistive elements are used for reading back the stored information for having higher SNRs than optical recording method and achieving higher areal density[5][6]. Though, HAMR technology is used with high magnetic anisotropy materials, such as Fe/Pt related materials and can achieve high areal density, it also suffers from some technical difficulties such as: focusing light to sub 30 nm spot with sufficient energy of a few mW, which is challenging for fabrication, in addition achieving sub 5 nm grains with high magnetic anisotropy and high coercivity media fabrication is another

big challenge to overcome. Due to the challenges mentioned above, this method can obtain areal densities of $\sim$ 350 Gb/in^2 with a 10 % allowed jitter noise with perpendicular recording system [7].

The second alternative technology for achieving high density storage is Discrete Track Recording (DTR)[8][9], which stacks the signals along a single track and physically separating it from other tracks. However, it might take too much time to pattern a single disk and the bit transition noise is still determined by the reversal of magnetization direction in adjacent grains.
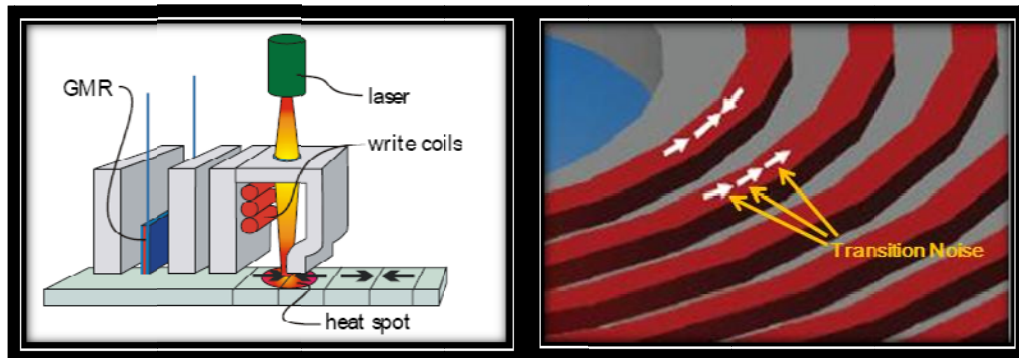
Figure 2.1: Schematic structure of Heat Assisted Magnetic Recording (HAMR) and Discrete Track Recording (DTR) [9][10]

Next alternative technology is nano-imprint lithography (NIL), which Dr. Chou in Princeton University suggested in 1995[11]. The principle concept of NIL is very simple and has a potential for high yield performances. Although, NIL has developed and suggested high areal densities [12], pattern dimensions performance, since Dr. Chou's original proposal, have met critical technical obstacle. Normally, NIL molding employs electron beam lithography (EBL) for fabricating the "main stamp / mother mold", however it takes too much time with EBL for duplicating the "child stamp". Also the needs from various industries for mother mold materials such as, Si, SiO$_2$,

SiC, Silicon Nitride, Sapphire, etc are not met, and many research groups only can perform sufficient durability and hardness from Si, and SiO_2 in current. Secondly, controlling the precise pressure, in mother mold approach, between the mold and the other substrates for duplication, is key procedure, which determines the quality of the imprinted features. In this procedure, the resist viscosity between mother mold and substrates for duplication is also another decisive factor in the quality of the outcome result. Thirdly, NIL also has a thermal effect which can affect the magnetic properties if substrate temperature goes high over the threshold limitation, and it also conduces to resist mismatching between two molds [13][14][15][16].
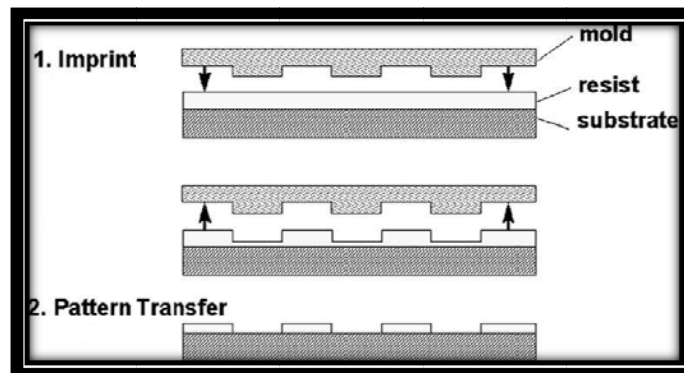
Figure 2.2: Schematic procedure of nano-imprinting lithography(NIL) [11].

The crucial advantage of bit patterned media (BPM) is segregating each bit's data with the structure as magnetic- non-magnetic- magnetic structures. BPM, in terms of reducing bit transition noise, is superior to DTR method and can achieve larger grain volume. As a result of one bit's magnetic moment direction changing conducts the other magnetic moment direction, one bit forms magnetic exchanging coupling successfully. BPM can give higher SNRs result than any other methods. Possible materials are Co/Cr alloys, L10 materials such as Fe/Pt relative materials as changing

9

the atomic structure from Face-Centered Cubic (FCC) to Face-Centered Tetragonal (FCT) and Co/Cr, Co/Pt, Co/Pd multilayer[17][18][19][20].
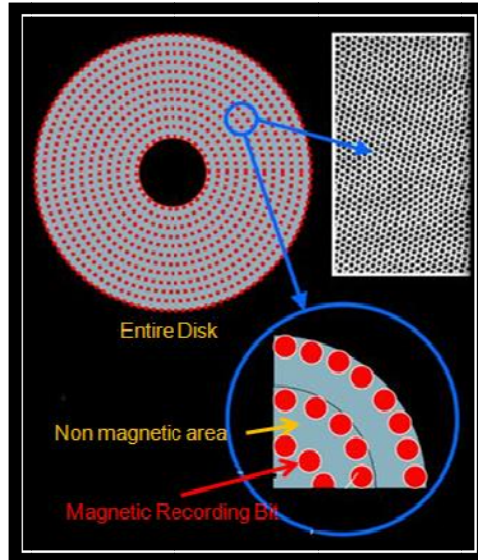
Figure 2.3: Schematic structure of Bit Patterned Media (BPM)[21]

The described representative technologies so far are top-down methods, grouped in two typical categories. The last method is oriented bottom-up approach, Self Assembled Monolayer (SAM), and it is quite prominent technology for high areal density field.

3. Demanding for high density data devices

Hard disk drive industry based on magnetic information storage, continuously develop and grow, market share has been expanding since the primary computer, RAMAC, releasing in 1956 from IBM. In 1999, the market share of hard disk industry was $89 million and keeps expanding with increasing needs and finally we predict $640 million in 2011. Most of consuming area of hard disk industry was personal computer related industry, but the portion of usage is also extending to other industries such as Digital Video Recording (DVRs), Personal Digital Assistant (PDAs), Digital Camera, Video Games, Cellular Phone, High Dimension Television (HDTV) and so on. The markets demand, not only an increase in production number, but also cost efficiency, proper maintenance with cutting-edge technologies, and miniaturization of hard disk devices for suitable consumer's personal electronic devices.

The ancestor of the hard drive as shown in illustration (fig.3.1) in personal computer was released by IBM with the name of RAMAC in 1956. Its areal density was 2 Kbits/in^2, 70 Kbits/s data rate, and 24 inches disk with 50 stacks. The capacity of recording storage is only one MP3 song at a cost of around $50000 dollars. After four decades, new micro-device from Seagate, costs only $55 ~ $65 dollars, was released 250 K Mbytes with 3 Gbits/s data rate and capability to store over 60,000 MP3 song on one disk [22].
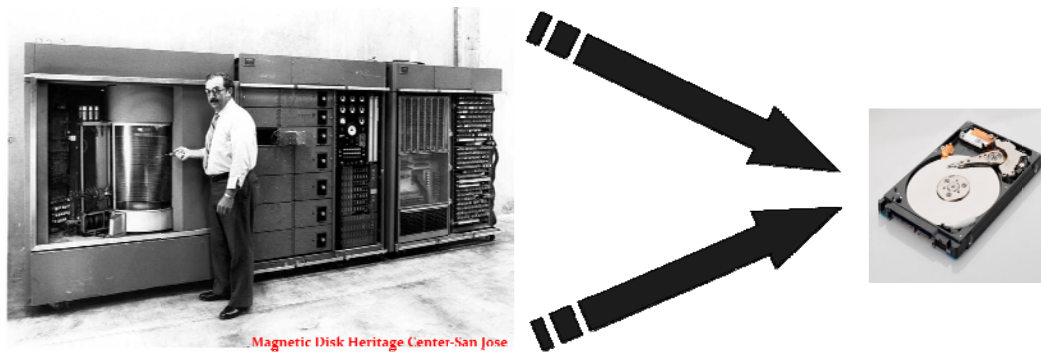
Figure 3.1: Hard disk drive development from the ancestor storage system to new technology. Left image is the first modern type of computer, RAMAC, was invented from IBM in 1956 and right is from Seagate hard drive "Momentus" series [23].

Chapter 2. Physical Background of Current Limitations in HDD and Electron Beam Lithography

2.1. Superparamagnetic Limitation

Among the obstacles for hard disk drive industry, one of main key challenges is overcoming the constraints imposed by the superparamagnetic limitation, which occurs when the micro-established magnetic grains, embedded information or signal, on the disk become so infinitesimal in size that there are affected by the temperature of neighboring bits and suddenly reverse their magnetic orientations. When ambient condition is influenced by heating, the energy barrier depicted in illustration Fig. 5, separating the two stable directions of the magnetic moment,$\Delta E = KuV$,will collapse and the magnetization direction will filp. As a result of this, the affected bits cannot storeprevious data. In this illustration, I describe the magnetic orientation north and south, however after the proper energy barrier has collapsed due to adiabatic effect, there is no guarantee that the magnetic orientation will sustain its previous direction [24][25][26][27].
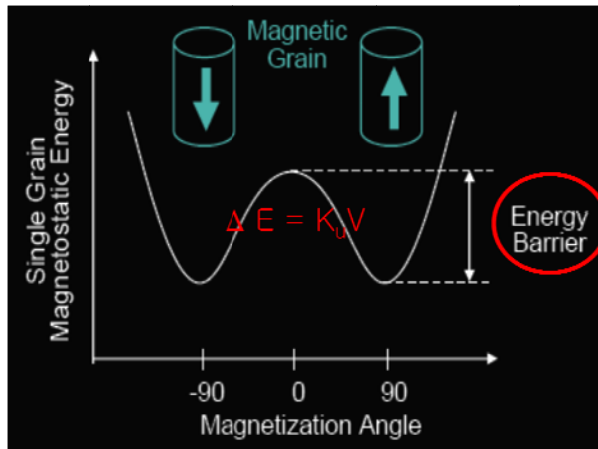
Figure 2.1.1: The sufficient energy barrier for sustaining each data bits

τ_N = The average length of time for the magnetization to randomly flip
as the result of thermal fluctuation

$$\tau_N = \tau_0 e^{-\left[K_u V / k_B T\right]} \tag{1}$$

τ_0 = Length of time, the attempted freqneucy normally $10^{-9} \sim 10^{-10}$ seconds.

$K_u V = \Delta E$ = Energy Barrier

K_u = Magnetic anisotropy density constant ($\sim$ erg/cc)

V = Grain Volume

T = Absolute Temperature in K

k_B = Blozman constrant

In order to sustain the signal in each microscopic grain, the power factor $K_u V / k_B T$ in equation (1) should be in the range from 40 to 80. For example, if $K_u V / k_B T$ equals 60, then the average length of time for holding the magnetic orientation in a bit is around 3.5 x 10^9 years. However, if $K_u V / k_B T$ is25, then the bit can store the data for only 72 seconds before losing its magnetic orientation.

14

2.2. Scaling Law

Currently to insure the adequate signal to noise (SNR) ratio, each bit must encompass around 50 to 100 grains [4].

$$\text{SNR} \propto 10\log(\text{N}) \qquad \text{N} = \text{grains per bit}$$

Assuming cubic grains:

$$a \approx \frac{1}{\sqrt{\text{areal density}}} \qquad a^3 \approx \text{volume of the grains}$$

When scaling down to reduce the entire size of hard disk, the bits must preserve the sufficient grain number. In other words, a reduction in recorded bit size requires a reduction of the grain size in order to retain a sufficient number of grains per bit and maintain an acceptable SNRs. However, thermal instability occurs from neighborhood bits and causes bits consisting of several magnetic grains or magnetic clusters to be shaped irregularly and randomly packed. Such imperfection as a jitter noise in grain boundary causes the playback noise and poses a technological challenge when synchronizing the signals.

2.3   Longitudinal and Perpendicular Recording

So far, I described the limitations such as superparamagnetic limitation and scaling law when scaling down for high density hard disk storage. Many researchers are making an effort to overcome these limitations. In longitudinal recording, the magnetic orientation of the data bits is aligned horizontally, as its name indicates; applied parallel to the surface of the disk. On the contrast, in perpendicular recording, the magnetic orientation of the data bits is allocated vertically, perpendicular to the surface of disk. In this orientation, materials of smaller crystalline grains can be used, because in such structure of magnetic orientation it is harder to reverse the magnetic direction; this results in smaller physical bits, which are still stable at room temperature. In longitudinal recording the write process is done with the fringing write field of around $2\pi M_S$. However, the gap in perpendicular recording possesses effective write field occurring around at $4\pi M_S$. This double writing field in perpendicular magnetic recording head is able to meet the requirements for high magnetic anisotropy materials and also achieve higher signal to noise ratio (SNR) than the longitudinal magnetic method.

As shown in illustration 2.3.1, the data in medium was stored in longitudinal direction and the magnetic material's magnetization in each particle can hold the data under certain level of the energy barrier but sometimes its magnetizations are flipped due to the change of the anisotropy energy barrier $K_u V$, where K_u is the anisotropy constant for a given magnetic material and V is the volume. If the fringing filed in the writing process from head to medium is higher than the coercivity of the grain, then the

magnetic anisotropy energy in medium cannot hold its magnetization and finally magnetization of each grain will be fliped over and the stored data will be lost. Another challenge in longitudinal magnetic recording concept, arises during the magnetic transition one bit to another neighboring bit, due to the not precisely defined boundary, which is affected by grain size, in case of smaller grain size the jitter noise increases. Therefore, as consequence of that when achieving higher density by shrinking the bit cells without shrinking bit grain size, the magnetic transitions cause more noise, which ultimately poses a challenge to the read-back system for recovering the data.

First of all, in order to further discuss the advantages of Perpendicular magnetic recording concept, I must introduce demagnetization field theory, given by the following equation [28].

$$H_d = -NM \tag{1}$$

where M is magnetization vector, and N is the demagnetization tensor depending on the magnetic shape and the direction of the magnet. The closer the distance from the magnetization tips to the magnetic charge on medium, the stronger the demagnetization field is. However, in the previously mentioned recording concept, longitudinal recording, the distance between magnetic tips and magnetic charge gets closer as approaching the high density. The latter leads to a high demagnetization field and induce a loss of signal in the grain. In contrast to this effect in longitudinal recording, in perpendicular magnetic recording technology, demagnetization field is no longer an obstacle for storing the embedded data in the grains. Another advantage of perpendicular magnetic recording technology is it can have higher geometrical density than longitudinal recording concept. As illustrated in the schematic in figure

2.3.2. Moreover, in perpendicular technology the Soft Under Layer (SUL) as a magnetic medium has high permeability and it can act as a magnetic mirror [29][30]. It can be seen from the illustration in figure 2.3.4 that the SUL medium can virtually double the gap of the probes in perpendicular recording and it can achieve the high writing fields [31].
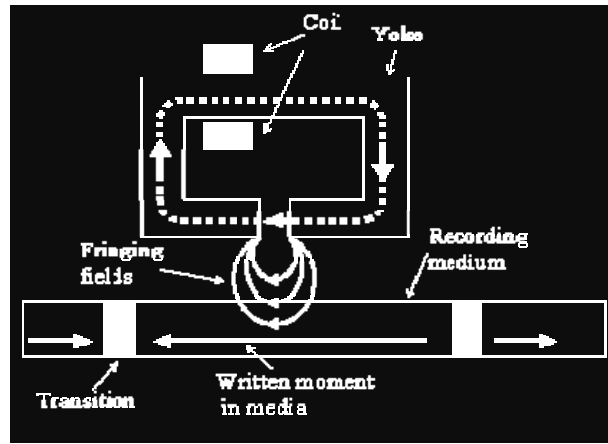
Figure 2.3.1: Schematic diagrams showing a side cross section of longitudinal magnetic recording – the medium grains in down the tract direction – with permission[31]
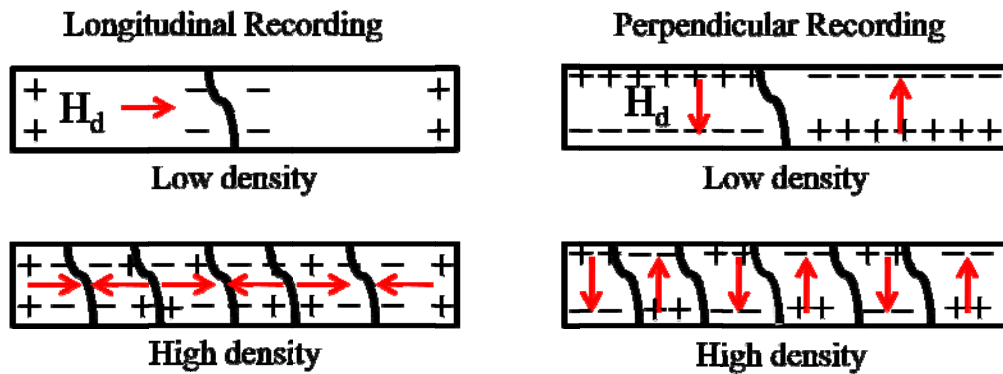
Figure 2.3.2: Medium states in longitudinal and perpendicular recording concept. Top first lines are showing the low density state and bottom lines are showing the high density states [29].
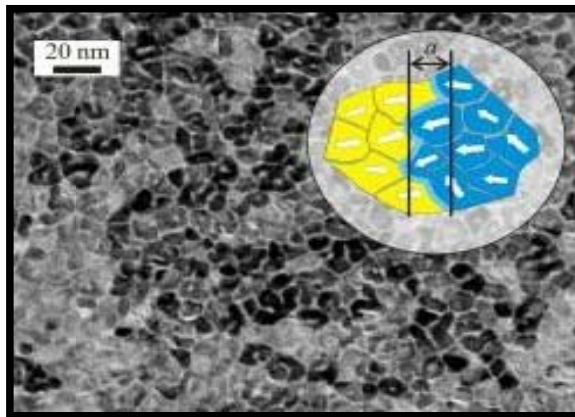
Figure 2.3.3: TEM image of surface grains in magnetic materials with jitter noise. As scaling down, the bit will be affected by the thermal instability and be lost its data due to the jitter noise.
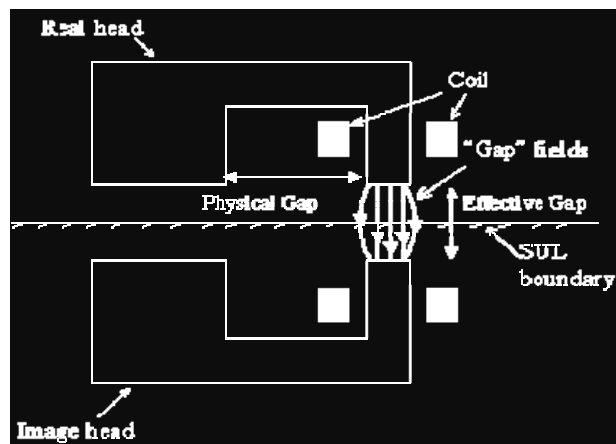
Figure 2.3.4: Schematic diagrams and 3 dimensional drawing of the magnetic imaging principle in perpendicular recording with soft under layer (SUL) – with permission [31]
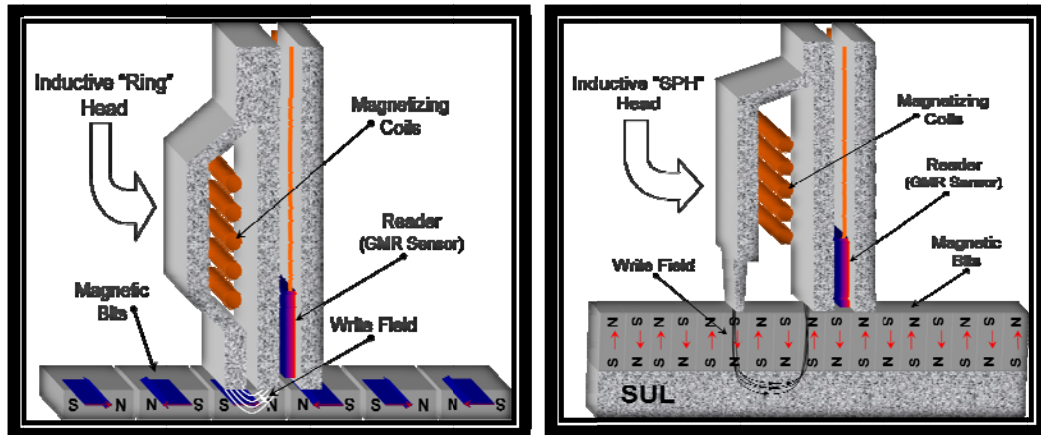
Figure 2.3.5: Schematic structure of writing procedure in longitudinal recording and Perpendicular writing. First recording concept is recording with fringing magnetic flux and next concept is perpendicular recording idea after transparent through SUL which enhancing magnetic flux for recording[30] [31].

2.4 Scanning Electron Beam

The earliest concept of theoretical scanning electron microscopy was introduced by the German M. Knoll in 1935. After a few years in 1938, Von Ardenne constructed the standard type of the modern SEM. In 1942 Zworykin et al. successfully modified the SEM design concept in RCA Laboratories in the United States. Finally, C.W. Oatley, a professor at Cambridge University, re-designed it in 1947 and since then many other important contributions have enhanced the scanning electron microscope [32].

The principle of a scanning electron microscope is very simple, as its name implies it is based on the principle of raster scanning a focused beam of electrons on the sample being imaged. When an electron beam bombards to surface of a material, generally two different types of significantly considerable interactions in electrons occur. Commonly, without critical energy loss, elastic scattering events occur in nuclei of atoms on the surface of the material, which cause changes only to the direction of the electrons. If considering the Schrodinger's equation, the wave forms are not changing in this case. On the other hand, there are inelastic scattering events occurring, accomplished by several different mechanisms, which all result in energy loss from the incident electrons. The first of these mechanisms responsible for electrons' energy loss is through the generation of secondary electrons in low-energy levels, the energy of secondary electrons is designated as less than 50 eV; 90% of secondary electrons have energies less than 10 eV, most have energies between 2 to 5 eV. Secondary electrons are used in SEM imaging for generating the topography of the sample and its contrast, as well as three dimensional images of the specimens. The

second mechanism for energy loss occurs through the generation of Auger electrons, similarly to secondary electron, Auger electrons occur when electrons bombard samples. However, Auger electrons emission process is quite different from secondary electrons emission and is illustrated in Figure 2.4.1. When an incident electron knocks out an electron from the atom, thus leaving a hole and ionizing the atom, as shown Figure 2.4.1(a). If this incident happens in an inner electron shell of the atom, outer shell electron move to the inner shell to fill the empty hole, as illustrated in Figure 2.4.1 (b). The energy released by this process could either be emitted as an X-ray, or it can cause other less tight bonding electrons to be ejected from outer shells, as depicted in Figure 2.4.1 (c). The latter energy emission process is known as Auger electron emission.
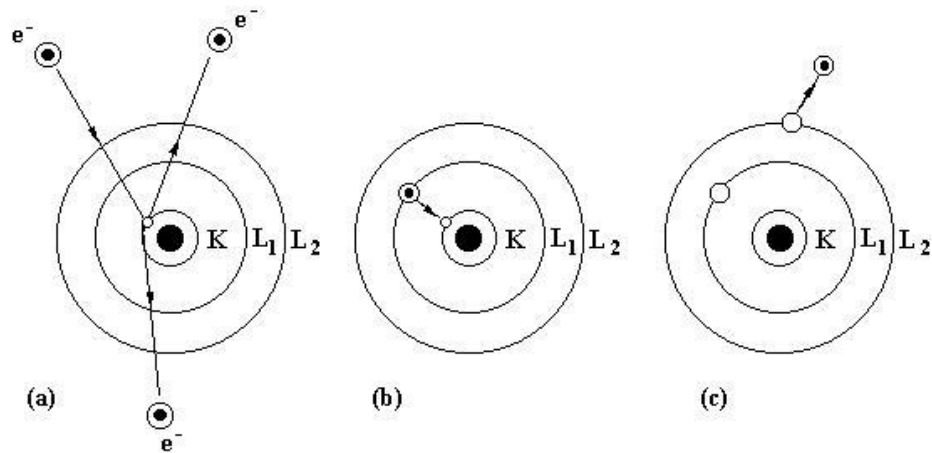
Figure 2.4.1: Various type of emitted electron. a) Incident electron collides with electron in inner shell and leaves a hole. b) Electron from higher energy level fills in the hole. c) Energy is released in the form of X-ray or by emission of an Auger electron.

In summary, the inner electron shell of an atom can be ionized by the electron bombardment on material, and then the vacancy is filled by an outer shell electron, because its bonding energy may not be stronger than inner shell bond. As a result

energy in emitted in the form of X-ray, or it can cause an electron from outer shell to be ejected.

If this electron has enough energy to leave, it can leave as Auger electron from the atom. Both the energy from X-ray and Auger radiations   can be used in the analysis of the material's surface composition. Especially useful is Auger electron, which has low kinetic energy; it   has-much smaller mean free path and has much better resolution than X-ray, but poor SNRs. The Auger and X-ray energies are frequently used for providing surface chemical information [32].   The third mechanism of loss of electron's energy, due to inelastic scattering interactions of electrons in the nuclei, is Bremsstrahlung x-rays, which literary means "Deceleration radiation". It is a form of radiation which is produced when a charged particle accelerates or decelerates. This is the principle used in synchrotron radiation and impact x-ray sources, where an electron beam hits a metal foil to generate x-rays.   Inside a solid, as the incident electron slows down, it emits Bremsstrahlung radiation. A number of other interactions in electron are the generation of lattice vibrations called phonons, electron oscillations in metals called plasmons, electron-hole pairs in semiconductors and insulators, long-wavelength electromagnetic radiation in the visible, ultraviolet, and infrared regions sometime called cathodoluminescence.
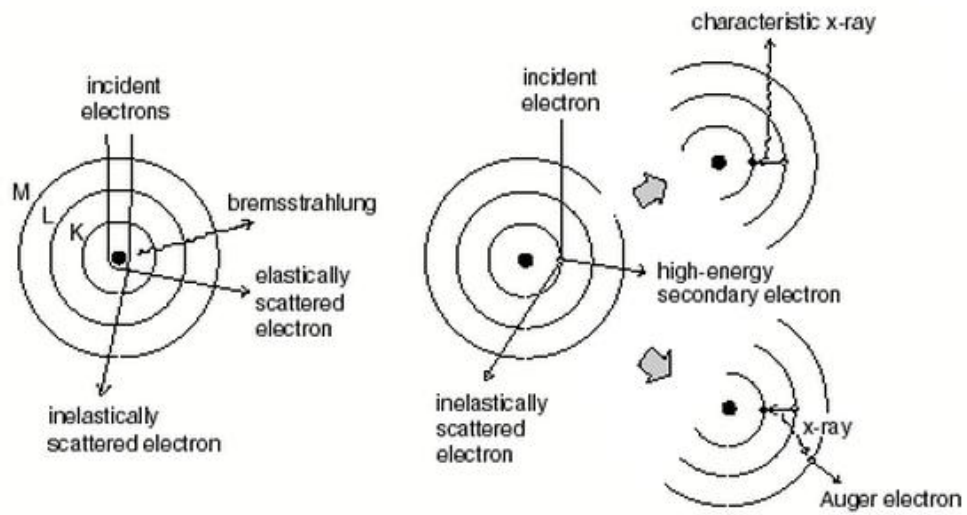
Figure 2.4.2: Characteristic of auger electron and x-ray emission after inelastic stattering

.

2.5 Electron Beam Lithography

Electron beam lithography system plays an important role not only for semiconductor development but also for development of next generation devices such as electron wave device, neuro-device, electron groups for integration of large area, high density, high accuracy of LCD and optical encoders, integrated circuitry of optical information processing devices, and micro machines for high density integration of micro sensors, micro actuators and electronic circuits.

As mention previously, electron scattering behavior on forward scattering and backward scattering are key points for deciding precise pattern shapes. Forward electron scattering in high acceleration voltage, such as 100 kV, can achieve narrow and high density distribution and be able to perform finer line. In same way, backward scattering in high acceleration voltage perform broad and low density distribution and due to this property, pattern results are adversely affected by the proximity effect. For this reason, large acceleration voltage can reduce forward scattering and backscattering at substrate surface. In other words, 100 kV beam intensity, electron beam lithography equipment can provide the finest and deepest lines and reduce proximity effect, having the possibility of super ultra fine pattern around 4 nm.

In electron beam lithography, forward scattering calculation is quite critical variable for deciding pattern dimension. The formula is

$$\Delta\chi = 0.9 \left(\frac{t_r}{V_{acc}}\right)^{1.5} \tag{5.1}$$

Where $\Delta\chi$ is beam size due to the forward scattering in nm.

t_r is resist thickness in nm.

V_{acc} is an acceleration voltage.

For example, resist thickness is 400 nm and acceleration voltage is 50 kV, then beam size from forward scattering is around 20 nm, with beam broadening from top of resist to bottom to the surface. Forward scattering and resist profile can also depend on the development time. Resist profile can also be controlled by changing the resistivity type from positive to negative.

The estimation of backscattering effect is quite a difficult matter, because it is decided on the higher atomic materials of substrate type. In this dissertation work, normally I have used Silicon or Silicon dioxide substrates and the ratio of backscattered electron values (η) are around 0.18 for Silicon, while back scattering range is as large as 5 to 20 micrometers. When primary incident electrons slow down, energy is dissipated in form of secondary electrons with energies ranging from 2 to 50 eV. Those electrons are responsible for the actual resist exposure and the depth range in the electron beam resist is around 8 nm.
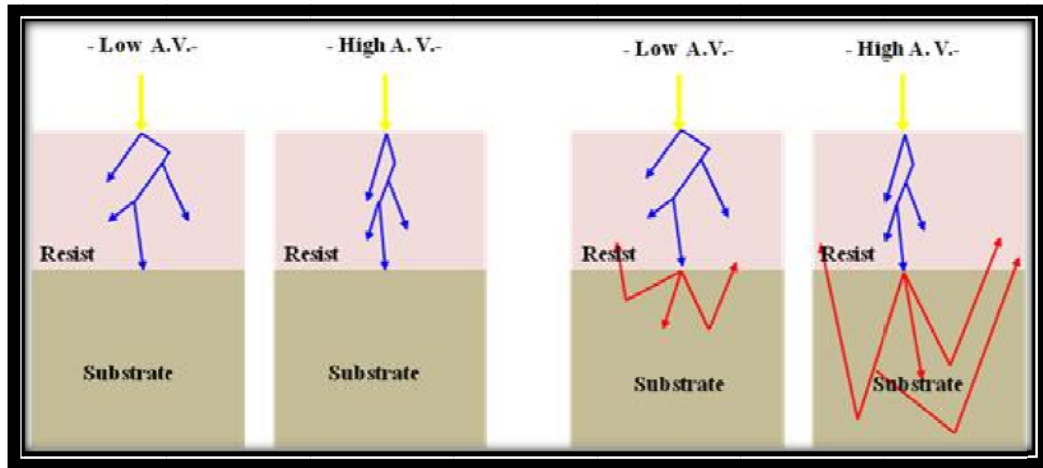
Figure 2.5.1: Electron scattering behavior. Two illustrations from left show forward scattering with low acceleration voltage 30 kV and high acceleration voltage 100 kV, while the two figures on the right reveal backward scattering with acceleration voltage of 30kV and 100 kV respectively.
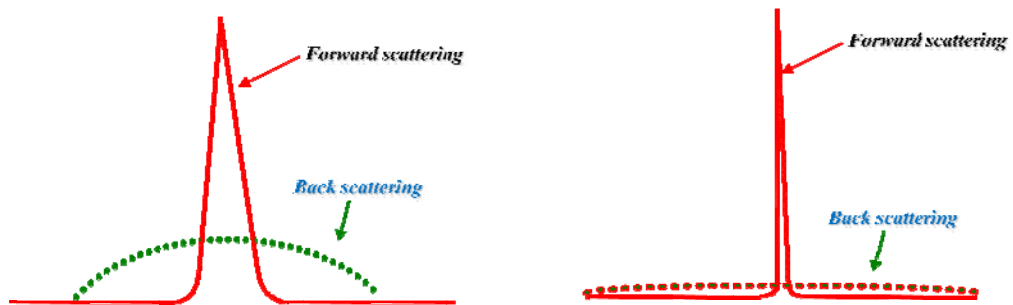
Figure 2.5.2: Electron emission scattering distribution. Left illustration shows low electron acceleration voltage such as 30 kV. The illustration on the right shows high beam acceleration   intensity, such as 100 kV acceleration intensity.

① Electron gun

⑬ Electron gun
alignment coil

⑩ Restriction aperture

② Blanking electrode

③ 1st lens
(1st demagnification lens)

⑭ 1st beam
alignment coil

⑧ 1st aperture selector

④ 2nd lens
(2nd demagnification lens)

⑤ 3rd lens
(3rd demagnification lens)

⑮ Astigmatism
correction coil

⑰ 2nd deflector

⑯ 1st deflector

⑨ 2nd aperture selector

⑥ 4th lens (projection lens)

⑦ 5th lens (projection lens)

⑱ Backscattered-electron
detector

Figure 2.5.3: Cross-section of JEOL Scanning Electron Beam column [34]

28

The Bragg law diffraction [33], although it is used to describe x-ray diffraction, can successfully be applied to wave particles. The Davisson-Germer experiment [34] can demonstrate the wave performance of the electron and confirm the earlier physical hypothesis concept of de-Broglie wavelengths "every particle can be described by its de-Broglie wavelengths".

$$\lambda = \frac{h}{\mathcal{P}} = \frac{h}{\sqrt{2meV}} = \sqrt{\frac{150.5}{V}} \times 10^{-10} \text{ m} \tag{5.2}$$

For example, the wavelength of electron in electron acceleration voltage through 100 volt. Then, velocity is $v = 5.9 \times 10^6 \, m/s$. so the wavelength is around,

$$\lambda = \frac{6.626 \times 10^{-34} J \cdot s}{(9.11 \times 10^{-31} \text{kg})(5.9 \times 10^6 \text{m/s})} = 1.2 \text{ x } 10^{-10} \text{m} = 0.12 \text{ nm} \tag{5.3}$$

and this wavelength is shorter than the visible wavelength of about 390 nm. Also, electron beam wavelength is around 0.0549 nm if we apply 50 kV beam acceleration voltage. Therefore, optical lithography has the limitation of diffraction of light but electron beam lithography does not have any diffraction limitations. Selecting electron beam as a lithography method gives more advantages, for example, electron beam spot size is around 5nm, while in optical lithography it is around ~ 500nm, and as depending on designer's purpose it can achieve lower defect densities than optical lithography. I have summarized the differences between the two lithography methods in Table 2.5.1.

Advantage of EBL	Disadvantage of EBL
Spot size is around ~ 5nm vs 500 nm in Optical lithography	Strong scattering electrons on solid structures
Requires only software mask	Requires vacuum ambient conditions
Flexible alignment with wafer structures	EBL system is more complex than optical lithography
Lower defect density compared to Optical lithography	Long time necessary for exposing even a single wafer
	System and maintenance cost are very high

Table 1.5.1: Comparison of the features of Electron Beam Lithography vs. general optical lithography
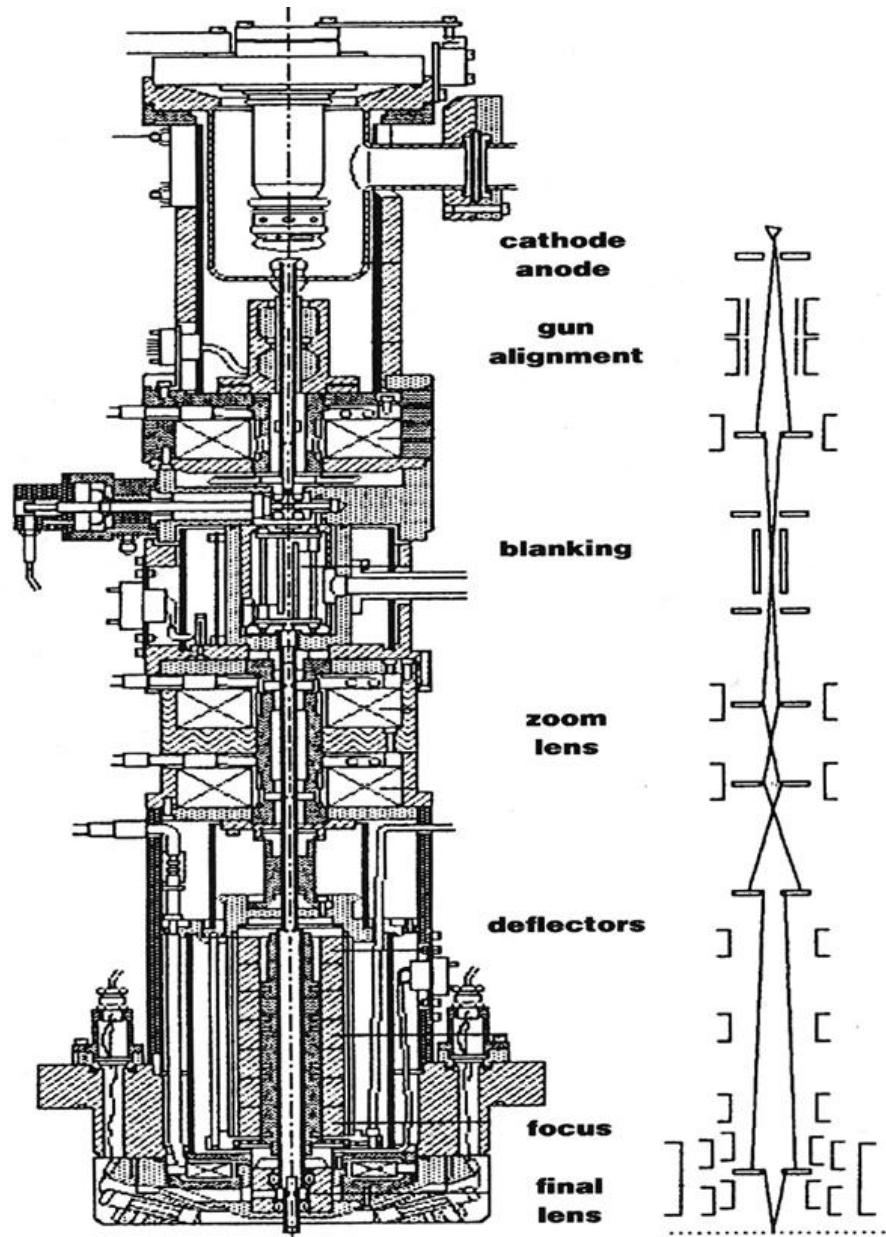
Figure 2.5.4: Cross-sectional schematic of the structure of electron beam lithography with the various corresponding electrical and optic components. (From Leica Lithography System LTD) [34]

Chapter 3. Characterization for High Areal Density

3.1. Pre-requirement for high areal density

In modern hard disk drive industry, researchers are trying to increase high areal density by various methods, which I described briefly in a previous section. Table 3, shows the well known requirements for achieving high areal density. For achieving 550 Gb/in^2, the bit area must be lower than 1290 nm^2 and the dot pitch distance along the track is supposed to be less than 35.9 nm, while 1 Tbit/in^2 requires 675 nm^2 bit area and dot distance of less than 27 nm. Although, there is no research groups who have achieved above 1 Tbit/in^2 density so far, in this section I will describe the realization having the potential to achieve above 1 Tbit/in^2.

Density	Bit area	Dot-Pitch along the track
550(Gb/in^2)	1290 (nm^2)	35.9 nm
750(Gb/in^2)	860 (nm^2)	29.3 nm
1000(Gb/in^2)	**675 (13 x 52 nm ^{2})**	**~27.4 nm**
2500(Gb/in^2)	**258 (nm^2)**	**~16.1 nm**

Table 3.1: The requirements of sufficient Bit area and Dot pitch along the track for various areal densities.

Starting from the polymer characterization, I present five linchpin constraints of high density patterns. First, fixing the development duration, I seek the tendency of dosage correlation between the dimensional variation followed by the distance changes within the patterns and vice versa, and the dosage variation as the exposed area

changing.

Moreover, two representative experimental fabrication methods, such as pre-patterned media and patterned media with positive and negative tone polymers will be described, with presenting some problems in each procedure and suggested solutions for resolving those problems. Scanning Electron Microscopy (SEM), Atomic Force Microscopy (AFM), Magnetic Force Microscopy (MFM) and Magneto-Optic Kerr Effect Microscopy (MOKE) results are used to show the feasibility of ultra high areal density magnetic pattern.

3.2. Resist Characterization

There could be a considerable difference in the data provided by the polymer manufacturer regarding thickness step height for polymer and the real tangible results obtained in an experiment. This is due to the fact that chemical properties and composition can slightly change from the time of manufacturing to the time of actual experiment. Moreover, my experimental processing steps can quite critically influence the step height even if the step height variation is not critical for other processes. Experiments in this dissertation, for achieving high areal density begin with characterization of various resists. There are two commonly used e-beam resists, as positive and negative tone, respectively. Positive tone resists are Polymethyl-meta-acrylate (PMMA) types which were released in the market by Rohm and Hass company in 1933[35] with molecular formula, $(C_5O_2H_8)_n$, it is generally used as a high resolution positive resist electron beam lithography as well as x-ray and DUV lithographic processes and its sensitivity is a critical aspect in determining pattern performance. Typical developer used for it is 1:3 methyl isobutyl ketenes: isopropyl alcohol and resist sensitivity is reported in the range of 5x 10^{-5} to 5x 10^{-4} coulombs/cm^2 [36]. Meanwhile, due to the solvent type of either chlorobenzene or anisole, 495K and 950K molecular weight (MW) PMMA resists can cover a wide range of polymer thickness [37].

The most notably used as a negative resist, hydrogen silsesquioxane (HSQ), was invented by Dowcorning and it was well used as the passivation films in semiconductor industry, serving as a low-k dielectric material [38] because of the

thermal effects, HSQ turns the nature of its properties into Silicon Dioxide (SiO_2) [39]. Aside all of those reasons, HSQ's high sensitivity to electron-beam lithographic technology makes it an ideal candidate for inorganic and negative-tone resist, for its many desirable properties. Especially, its capability of achieving very high resolution and high mechanical strength of its patterns after electron beam exposure and development procedures [40].

When shrinking the pattern dimensions smaller than ~50 nm, we face on the most critical challenge; Lift off process is used for removing the materials deposited on unexposed (or exposed) polymer when Acetone (polymer solvent) submerges through the sidewall of the polymer, dissolving it completely after certain time duration, after this process only the desirable patterns are finally staying onto the substrate. However, when pattern dimension become smaller than 50 nm, polymer residues may remain on substrate after development, and in this case the target patterns which are supposed to stay on specimen are also washed away due to the harsh processing step such as using acetone gun or brushing the substrate.

For this reason, I have attempted to find other alternative processing techniques, and also make use of negative tone resist, typically HSQ, which can eliminate such problematic obstacle.

 The results of resists thickness followed by the appropriate spin-coating condition [41][42] are only applicable to large patterns such as above 500nm dimensional pattern. Therefore, those suggested recipes [43][44] in the provided data by the manufacturer are not sufficient enough to be used in the fabrication of high areal density patterns. In respect to that, it is necessary to re-characterize step height in order to obtain proper process recipes needed for achieving the desirable results. Table

4 sows the result after characterization. These results include characterization of various types of positive and negative tone polymer resists. I characterized the most representative positive tone polymer so called PMMA, which can be categorized in different groups of PMMA resists, depending on the solvent used. For example, Chlorbenzene and Anisole are general solvents used for PMMA; mixing PMMA with either one of those solvent is denoted by a footnote with capital letter of 'A' or 'C'. Moreover, deciding the concentration of PMMA is also quite critical for setting the step height thickness. From experimental results, it is seen that thickness is getting smaller as the polymer concentration in the solvent reduced. That means that the thickness achieved with 2% concentration PMMA is thinner than 4%, or 6% one. Table 6 shows a simple equation for determining the proportions of PMM and solvent needed for preparing PMMA C 2% and PMMA A 2%, using polymer with molecular weight (MW) 996k.Based on this result, for PMMA C 2% preparation, 2.26 g polymer and 88.528 ml Chlorobenzene solvent, must be continuously mixed at 80 ℃ hot plate, overnight, the preparation of PMMA A 2% is similar..

Experimental procedures of measuring polymer thickness start with the substrate cleaning from organic, oxide, and metallic contaminants. For removing insoluble organic contaminations, substrate must be submerged for 10 minutes in 5:1:1 = $H_2O:H_2O_2:NH_4OH$ solution. Secondly, for removing a thin silicon dioxide layer, on which metallic contaminants may have accumulated as a result of first process, the substrate is diped into a diluted 20:1= $H_2O:HF$ solution.

Chlorobenzene (C)	Anisole (A)
Density from **MSDS: 1.107 g/cm³**	Density from **MSDS: 0.995 g/ cm³**
$1.107g : 98 = 1 : x$ $x = \dfrac{98}{1.107}$ $\approx 88.528ml$ $\dfrac{88.528ml}{98g} \Leftrightarrow \dfrac{996K}{2g}$ $88.528ml : 2g = 100ml : x$ $x = \dfrac{200}{88.528}$ $\approx 2.2592g$ $\cong 2.26$	$0.995\ g : 98 = 1 : x$ $x = \dfrac{98}{0.995\ g}$ $\approx 98.492\ ml$ $\dfrac{98.492\ ml}{98\ g} \Leftrightarrow \dfrac{996\ K}{2\ g}$ $98.492\ ml : 2g = 100\ ml : x$ $x = \dfrac{200}{98.492}$ $\approx 2.031\ g$

Table 3.2.1: 2% PMMA fabrication with different solvent, chlorobenzene, and anisole with 996k polymer molecular weight (MW).

Third step involves cleaning ionic dirt by removal of ionic and heavy metal atomic contaminants by a solution of 6:1:1 = H_2O:H_2O_2:HCl, for 4 minutes. After each cleaning step, substrate is rinsed by DI water. Finally, the substrate undergoes a "Piranha cleaning" for removing other organic materials such as photoresist, oil, etc. This cleaning process requires mixing 98% of H_2SO_4 (sulfuric acid) and 30% H_2O_2 (Hydrogen peroxide) in volume ratio of 2 ~ 4 : 1, at a temperature of 100 ℃ under ambient condition and submerging the substrate in it for 4 minutes. Thereafter, all cleaning steps are repeated to ensure optimal purity of the substrate.

In the next process step, I spin-coated the polymer onto the 2 x 2 cm² clipped silicon or silicon dioxide substrates, using the following parameters, spin speed of 5000 rpm, ramp speed of 1000 rpm, and duration of 60 seconds.

With all prepared samples, I opened three wide windows with electron beam lithography machine, with area around 10x10 μm², and the processing condition of

beam current being ~ 120 pA and dosage of around 120 ~ 140 μC/cm². Topographic

results of opened windows on substrate are measured with Atomic Force

Microscopy (AFM). A summary of the measured step height by AFM for all other

polymers is displayed in Table 3.2.2.

Type of Resists	Molecular weight(MW)	Step Height (Measured by AFM)	Step Height (From Company)
A 2 (+)	495K	63 ~ 70 nm	~80 nm
A 4 (+)	495K	120.7 ~ 130 nm	~180 nm
C 2 (+)	495K	102.1 ~ 120 nm	~130 nm
C 4 (+)	495K	200 ~ 250 nm	~320 nm
ZEP - 520A (+)	57K	32.4 ~ 38 nm	←
HSQ(XR-1541)6%	---------------	64.3 ~ 68 nm	---------------
HSQ 2% (-)	---------------	24.1 ~ 31 nm	←
Diluted HSQ (-)	---------------	25.3~ 33 nm	←

Table 3.2.2: The step height comparisons between company providing data and tangible experimental results of various polymers followed by the condition of 5000 rpm spin speed, 1000 rpm ramping speed and 60 seconds duration (Characterized step height by AFM).

It is critical to preserve the polymer under proper condition in order to insure

consistent lithography results, otherwise the polymer properties can be affected by the

environment conditions, which can affect the lithography process. The differences

between the actual measured polymer thickness and company provided data are not

negligible as expected by our first assumption. From the results of positive tone resists

from PMMA A2 to ZEP-520 A, it can be seen that the step height difference between

actual measured thickness and the data provided by manufacturer can range from 10

nm to 50 nm. This is not insignificant, and can give rise malfunction of entire

electronic devices. Because there are no published data for thickness step height of the negative tone resist, I used the result from the measurement shown in Table 3.2.2.

From table 3.2.2, I selected three different polymers as the proper candidate for realizing high areal density magnetic patterns, which are designated with red arrow. Based on over three years of numerous experimental results, I know for fact, that polymer thickness and the the desired pattern's dimension must have an aspect ratio of around 1 : 3 for both positive and negative tone resist, due to the effect of electron's "tailing". This means that for fabricating sub 10 nm dimensional patterns, Polymer thickness should be around less than 30 nm. If polymer thickness is thicker than the expected 30nm, experimental results will never guarantee sub 10 nm dimensional patterns. Therefore, I choose ZEP-520A from positive tone resist, 2% HSQ, diluted from 6% HSQ, as negative tone resists for generating sub 10 nm shape dimension.

I will discuss further the details of the resulting pattern's dimensions in next chapter. But to mention briefly, I was able to achieve 8 nm patterns in positive tone resist, and 27 nm pitches in negative tone resist with sub 10 nm pattern size.

3.3 Variables Characterization

Motivation

Fabrication of nano=size patterns for high technology devices, can be accomplished only if all process parameters are optimized.. Because my research field is in the nano-area, tiny variation in those variables will critically effect the final results, Optimizing those required parameters for all variables is not an easy task to achieve. Optimal maintenance and working conditions of all processing equipment is crucial for reaching the final result. However, in lithography field, it is often assumed that these requirements are satisfied. Therefore, in this section I will discuss five critical variables; Dosage, Dimension, Distance, Developing time, and exposed area. First, I will discuss the dosage trend with varying patterns' dimensions and distance between individual patterns. Next I will discuss determining the proper dosage with changing exposed area.

3.3.1. Dosage/Dimension/Distance

In figure 3.3.1, I schematically show the design of the nano structure patterns for finding the proper dosage trend. I used the embedded design software in JEOL JBX-5500FS and the Nabity software, NPGS CAD program, L-edit program, AutoCAD program can also be used after converting the file format to .GDS.

I designed the distance between patterns to vary from 250 nm to 25 nm in horizontal direction, and also vary the pattern dimensions from 250 nm to 25nm vertically at a same time. The entire resulting pattern covers an area of around 30x30 μm^2 and is surrounded by 5 μm areal reference marks.

Figure 3.3.2 shows the one-to-one corresponding SEM image after developing processing. The detailed lithography processing conditions will be discussed in next section, because they are different for each polymer tone. Those dosage results come from the conclusion of polymer step height measurement and the final dosage value will be re-characterized by varying the polymer step height.

From the illustration 3.3.3, I show the results of dosage characterization. The digit values in the illustration are the final dosages and their value is calculated by the equation below

$$\text{Final Dosage}(\mu c/cm^2) = \text{Basis Dosage} \times (1 + \text{Secondary Dosage}/100) \quad (1)$$

Let me, elaborate on dosage calculation little bit more, in equation (1), there are two different dosages we need to determine. First, one is called "basis dosage" and it acts as primary dosage and is used in the entire CAD file during exposing with electron beam lithographic equipment, the secondary dosage can be assigned to individual parts of the pattern designs. For example, when there is a need for multilayer design, such as MOSFET design with Cadence Layout, each layer needs to be chosen with different width and depth of line, with different dosage. Secondary dosage can be used to accommodate this need, although the basis dosage cannot be changed after it has been initially set.

Mechanically, I must select the electron beam moving step when exposing the polymer on the specimen. JEOL JBX-5500FS system has three different step modes, which can be selected, step 2, step 4 and step 8. Let's assume the exposing area on substrate can be divided as numerous grids and electron bean can stop and expose

each point of the grid. The interval between each point on the grid being exposed by the beam is determined by the step. Therefore, electron beam exposes a point once it crosses two grid points in the step 2 mode. While in step 8 modem the beam expose every eighth point on the grid. So, exposing a pattern of small dimensions would require using the step 2 mode, however researcher should be careful for choosing right the dosage because high beam energy selection will cause electron beam to stay longer in one single grid point and in small step mode will cause much worse results, and will produce over-exposed pattern. Normally, JEOL JBX-5500FS beam spot size is 4~6 nm. Therefore, accumulated experimental skill from operator is also one important element in determining the right dosage and step mode in the exposure of nano dimensional patterns. In this dissertation work I have used step 2 mode.

By the way, the dosage tendency is shown in illustration 3.3.3. According to the results, if the pattern dimensions remain the same and distance between patterns decreases the dosage should be also reduced. I found the dosage decreased from 700 $\mu C/cm^2$ to 390$\mu C/cm^2$. Meanwhile, maintaining same distance and changing the dimension size from large to small patterns, requires an increase in dosage from 700 $\mu C/cm^2$ to 2100 $\mu C/cm^2$ from 250 nm to 25 nm dimensions respectively. The surface areal density in edge and central part were also affected by the different development process. MF CD-26 was used for developing negative tone resist, while and MIBK: IPA=9:1 diluted solution was used for positive tone resist.

Figure 3.3.1: Schematic of design structure used to determine proper dosage trend. Distance varies from 250 nm to 25 nm, while pattern dimensions change from 250 nm to 25nm at a same time. The entire pattern exposed covers an area of 30x30 μm^2 and is surrounded by areal reference mark.
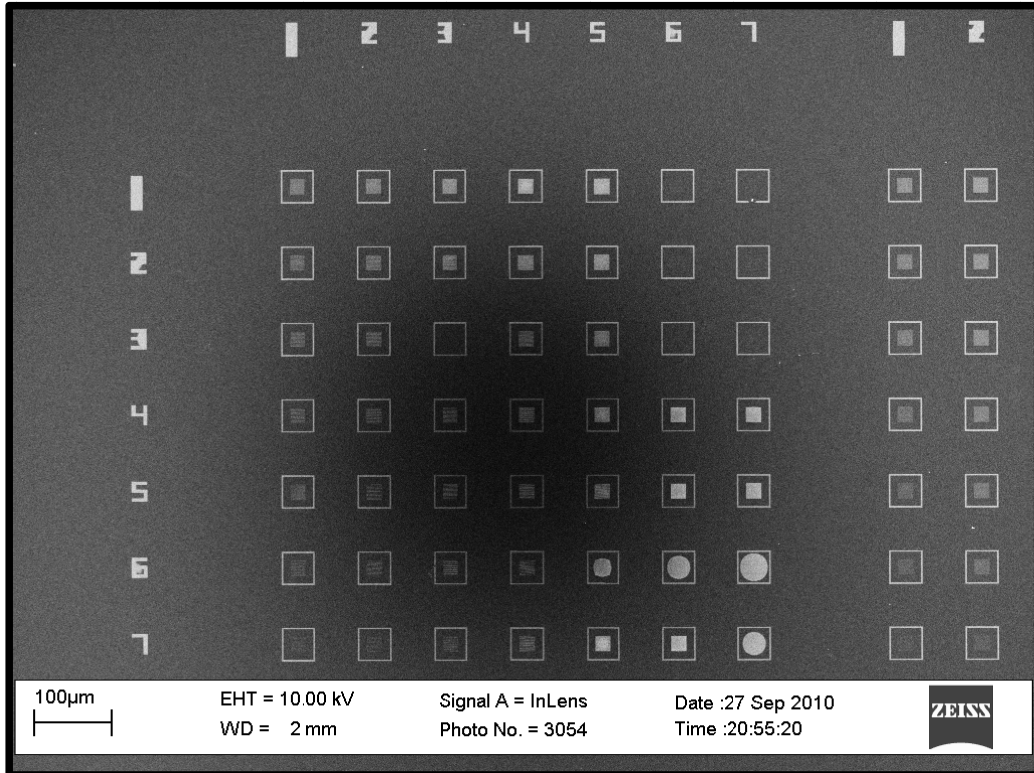
Figure 3.3.2: Corresponding Scanning Electron Microscopy image to figure 3.3.1. Applying same basis dosage in this entire file and choosing different dosages for each

detailed pattern. This SEM result is showing one part of 900 µc/cm^2 basis dosage. And 1000 µc/cm^2 basis dosage, in the other part respectively.
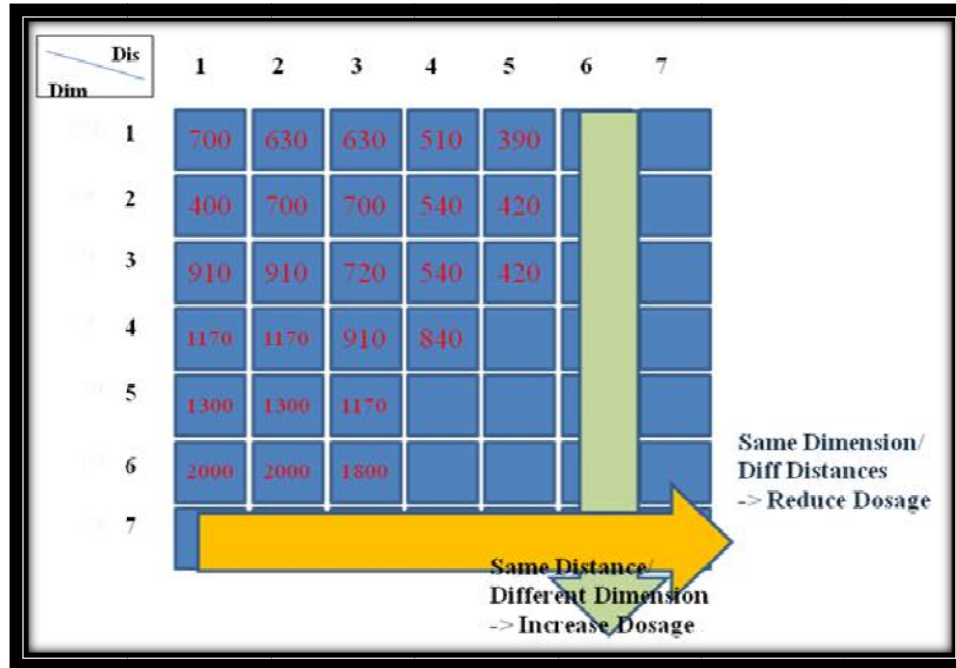
Figure 3.3.3: The dosage tendency results after final procedures. Red numbers are showing the dosage and its scale is ~ µC/cm^2. Maintaining same dimension and varying different distance between each patterns, requires reducing the dosage. On the contrary, keeping same distance and changing the dimension from large to small patterns requires increasing the dosage.

3.3.2. Dosage/Exposing Area.

In this section I will discuss the correlation between the two variables of dosage and the exposed area. First, I was expecting that the properly selected dosage from the previous experimental results will maintain and produce same results even when increasing the exposing area from 10 x10 um^2 to 30 x 30 um^2 or even larger. However, the SEM images show quite disappointing conclusion from applying the same dosage to larger exposure areas, therefore it is required to find new dosage as exposure area is changed.

Illustration 3.3.4 is SEM image after development procedure. Initially, the CAD design was intended to achieve 75 nm dimensional sizes and 90 nm pattern distances with 30 x 30 um^2 exposure area. The SEM image shows that in general, the produced pattern result perfectly matches the design in right bottom corner of the exposure 30 x 30 um^2 area, with the first selected dosage. However, the pattern shape changes in the center part of the exposure area, showing abnormal results with dimensions getting bigger than initial design. It can be seen from illustration 3.3.5, that pattern's sidewalls show coursing condition and still contain remaining polymer. Therefore, using same dosage as increasing the exposure area is not producing consistent results, in contrary to what was expected initially.

Hereby, I propose two methods for solving this problem. First one is by increasing the developing time duration; the second is by applying different dosage as electron beam approaches the more dense areas, such as the central parts. However, if I use the first suggested approach it can give rise to some other problems. Because the patterns at the edge of the exposed area, which have the right exposure will be deteriorated by

45

the chemical developer as increasing the developing time, even though this can lead

to obtaining perfect results in the high dense area in the middle. Perhaps, it can be an

alternative solution when using small area exposure but not as good in big areal

exposure. Therefore, second suggested method can be a better solution to the problem

even though it is experimentally more complicated. For example, when I draw 30x30

um^2 patterns areas to be exposed, I must divide it in 2 or 3 different layers with

different dosages, applying lower dosage the pattern in the central area.

= 74.84 nm

= 88.45 nm

1μm   EHT = 10.00 kV   Signal A = InLens   Date :27 Sep 2010   ZEISS
WD =   2 mm   Photo No. = 3245   Time :22:58:19
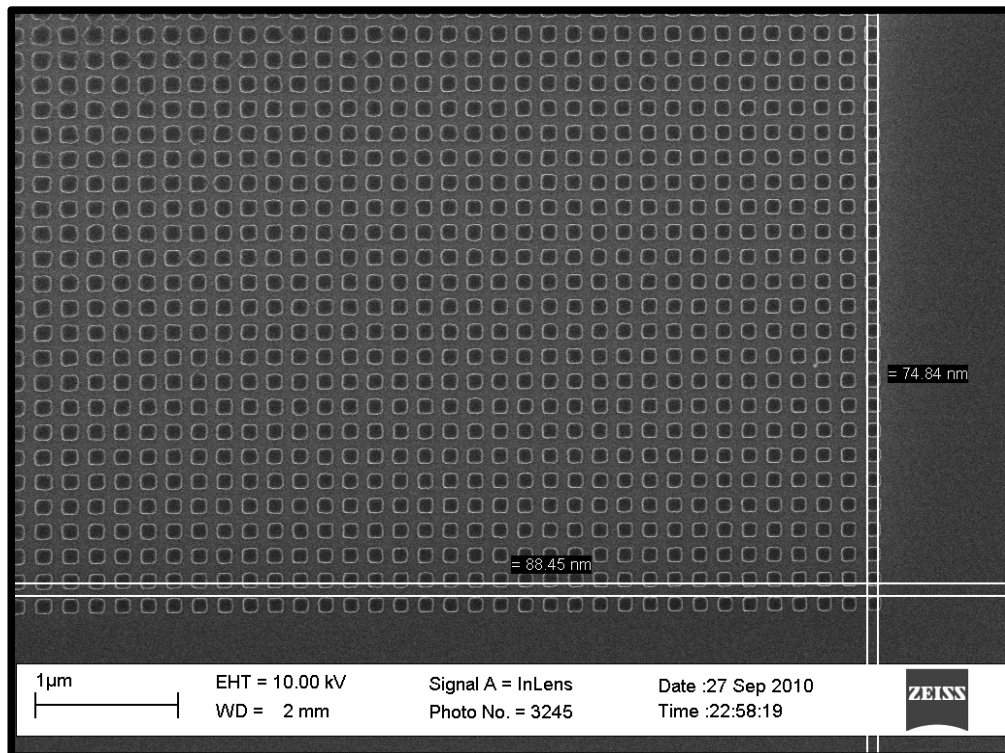
Figure 3.3.4: SEM image of results after development procedure. Side walls of patterns which are located in right bottom corner came out perfectly as the initial design intention.
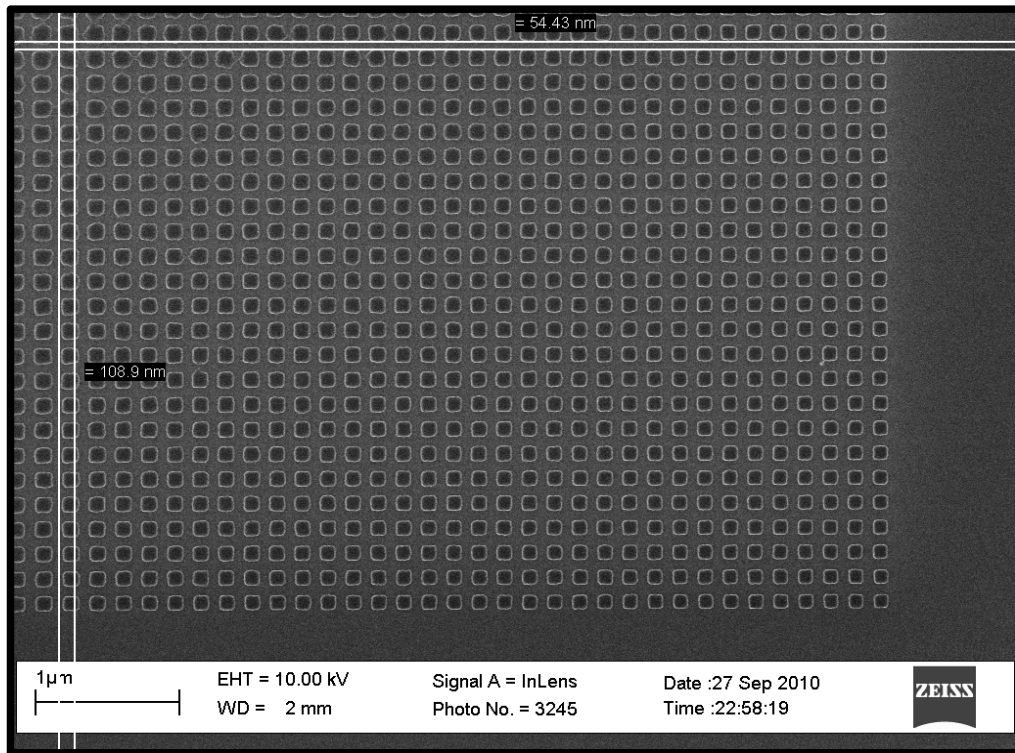
Figure 3.3.5: SEMimage of the results after development procedure. Side walls of patterns which are located in left-top corner are not produced as the initial design intention. It is same image as figure 3.3.4.

3.4. Experimental Result Images

In this section, I will show some result images from positive tone resist and negative tone resist. These results processing conditions will be used for fabricating Bit patterned Media (BPM) with 3-Dimensional multi magnetic layer recording (3D ML) and Discrete Track Recording (DTR). The main processing steps will be discussed in next section.

Cursor Width = 8.03 nm
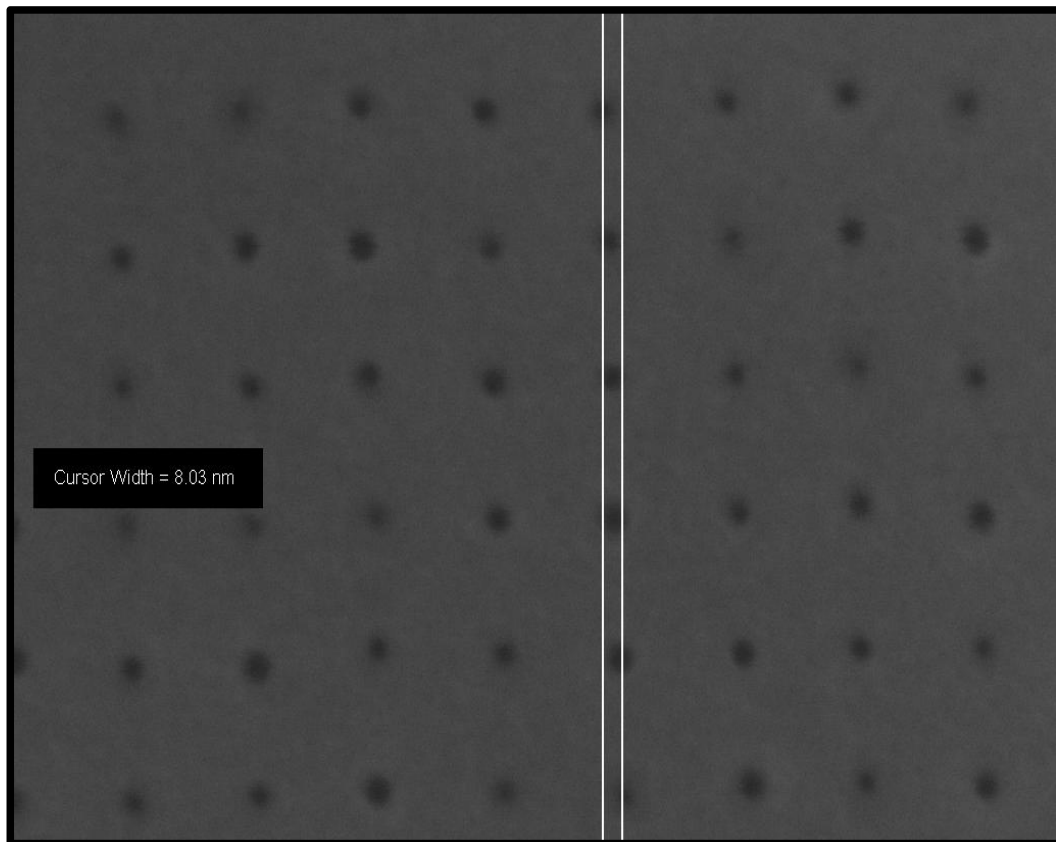
Figure 3.4.1: With positive tone resist, I accomplished 8 nm dots size on 30x30 μm^2 area by applying dosage of around 20800 $\mu c/cm^2$, beam current is ~98 pA. Development processing conditions are MIBK: IPA=9:1 in sub 10 ℃ ambient condition for 1 minute and rinsing in MIBK: IPA=1:1 for 15 seconds in room condition.

Illustration 3.4.1 reveals the result of positive tone resist, ZEP-520A, with 20800 μc/ cm2 dosages, ~ 98 pA beam current condition and the main chamber pressure is lower as 10^{-5} mTorr. Developing condition is dipping for 1 minute in MIBK: IPA mixture 9:1 ratio in sub 10 ℃ ambient conditions for controlling slow developing. Additionally, specimen is dipped in MIBK: IPA=1:1 ratio rinsing chemical liquid and DI water and gently dried with nitrogen. From SEM results, it is seen I achieved around sub 10 nm dot size patterns on the entire 30x30 um^2 exposure area.
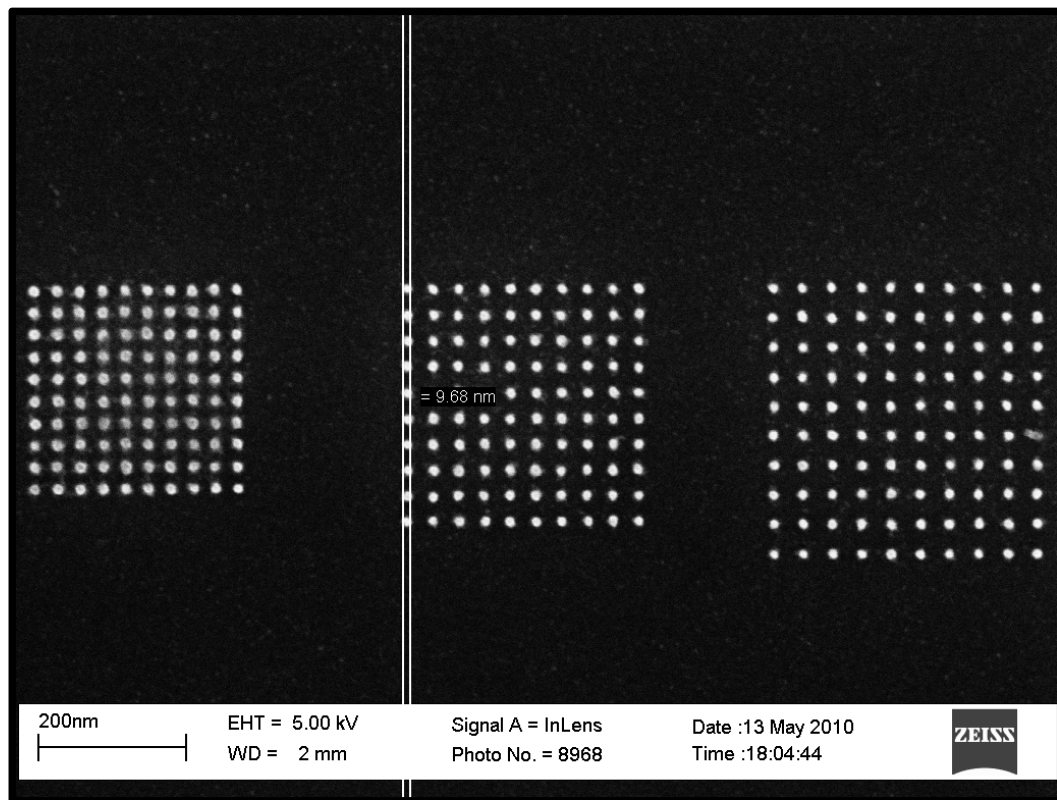
Figure 3.4.2: SEM result. 10x 10 array pattern dimension is sub 10 nm and vary the distance between the dots.

49

As seen from fig. 3.4.2, I have used negative tone resist, because if using a positive tone resist, "lift off" process must be used which cannot achieve good results for sub 50 nm dimension patterns. Negative tone resist can successfully be used to avoid the problems with "lift off", although it requires removing a large area of polymer in the development process; it is better suited method for sub 10 nm dimensional pattern lithography.

In figures 3.4.2 through 3.4.5, I have listed SEM images from numerous results from applying suitable exposure dosage for achieving the desirable pattern dimensions and distance between patterns. Figures 3.4.2 and 3.4.4 show the achievement of 10x10 arrays of dot patterns with sub 10 nm diameter. There are many considerable factors in assessing the merit of the lithographic patterns results, one important factor in the HDD industry is the dot-pitch size. The latter is critical not only for accomplishing the high areal density but also for measuring the synchronization of signals in reading and writing processes, with high magnetic probe and data embedded substrate. Two SEM images below show achieving around 33 nm and 28 nm dot pitch distance, which has a capability of over 1 Tbit /in^2.

Consistent results can be obtained with narrower pattern sizes, as shown in figure 3.4.4. SEM image shows the result of a 5x5 array pattern with sub 27 nm dot-pitch size and sub 10 nm pattern dimensions, which also has the capability of embedding data is also above 1 Tbit/in^2.

The fabrication parameters used in achieving these lithographic patterns are: 2% of negative tone resist (HSQ), with the exposure dosages varying from 7150 $\mu c/cm^2$ to 6700 $\mu c/cm^2$, in 50 $\mu c/cm^2$ dosage decrements. The development condition differs from positive tone resist developing condition; dipping the exposed sample in MF-CD 26 kept at sub 10℃ temperature in ambient conditions, for around 30 seconds including the time for moving the specimen in and out of the solution, then followed by rinsing the sample in DI water for around 1 minute.

Even though my research experimental result can successfully be used for achieving a capability of data storage above 1 Tbit/in^2, these experimental results, shown in Fig. 3.4.5, have the feasible potential of achieving even higher areal density. This can be accomplished by increasing the developing time more than 30 seconds, such as 40~43 seconds, then the remaining polymer will be perfectly removed by developer and experimental result of smaller dot-pitch distance like around 17 nm can be achieved, and this dot-pitch distance can approach the capability of 2.5 Tbit/in^2.

The application of this experimental result will be extended for use in the concept of 3-dimensional magnetic multilayer, for increasing the capability of embedding the data. Even though, the concept of 3-D ML may seem impractical to be adopted in industry field, because it requires changing the entire read and writing probe design, since detecting the signals with only one probe will be quite difficult to accomplish in short time. Despite of that, I will go over this concept in detail in next chapter, because it has a great potential in extending the capability of hard disk drive.
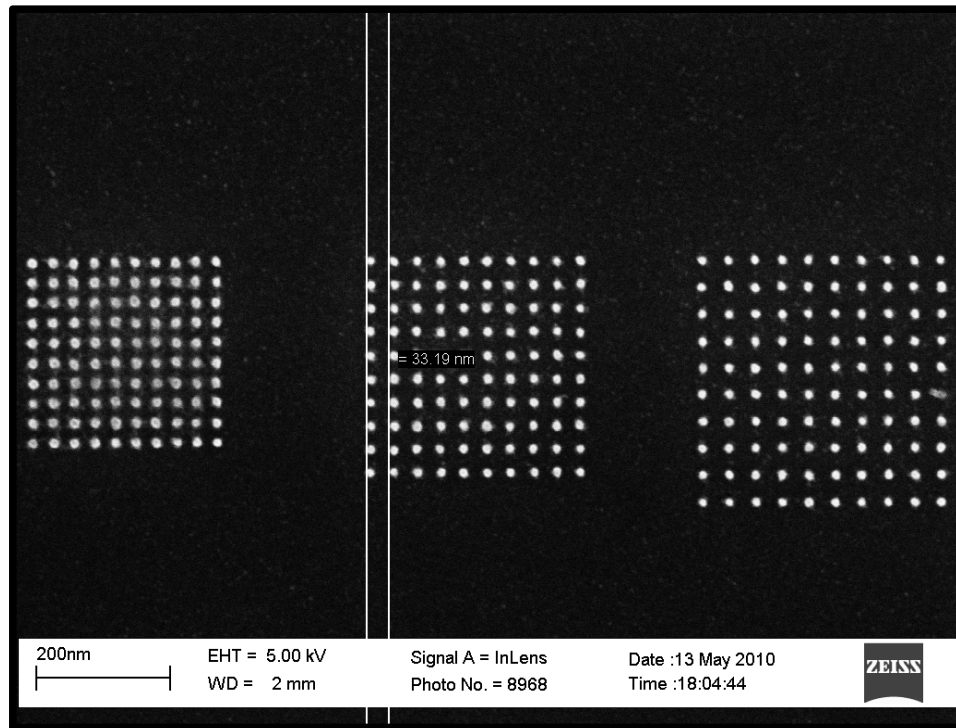
Figure 3.4.3: Negative tone resist lithographic result with sub 10 nm dot sizes and 33 nm dot-pitch size. According to this result, this method can be used for achieving over 700 Gbit/in^2.
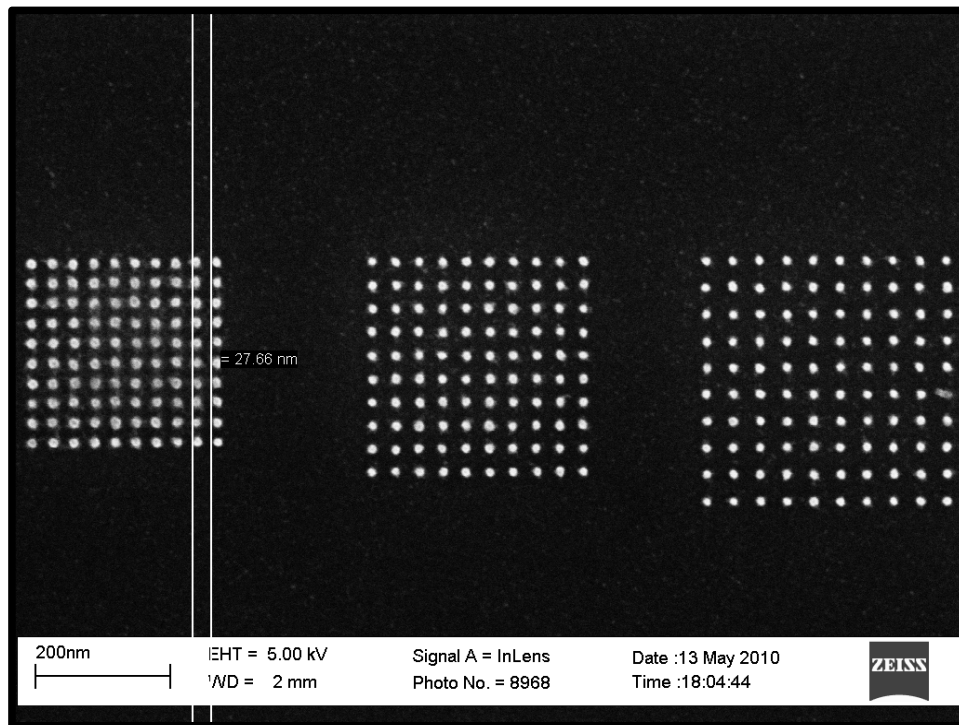
Figure 3.4.4: Negative tons resist lithographic result with sub 10 nm dot sizes and 28 nm dot-pitch size. According to this result, it can be used for achieving around 1 Tbit/in^2.
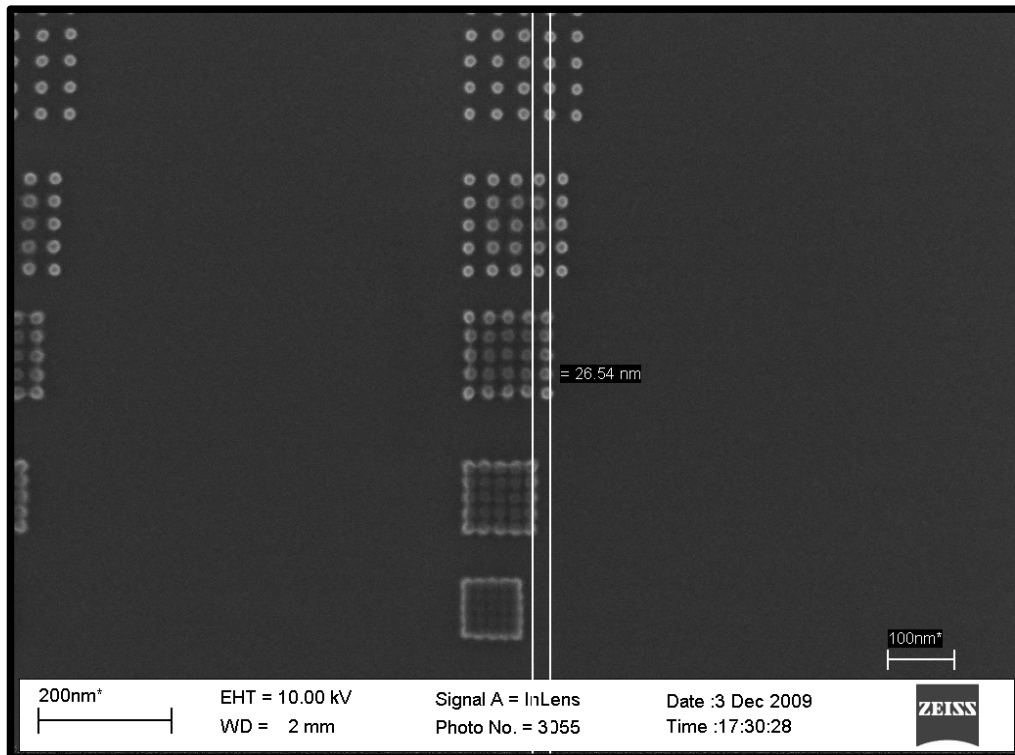
Figure 3.4.5: Negative tone resist, used for fabricating 5x5 array dot patterns, with sub 10 nm dot dimensions and around 26 nm dot-pitch, its capability is also above 1 Tbit/in^2. This pattern can show the feasibility of performing around 2.5 Tbit/in^2 by increasing developing duration.
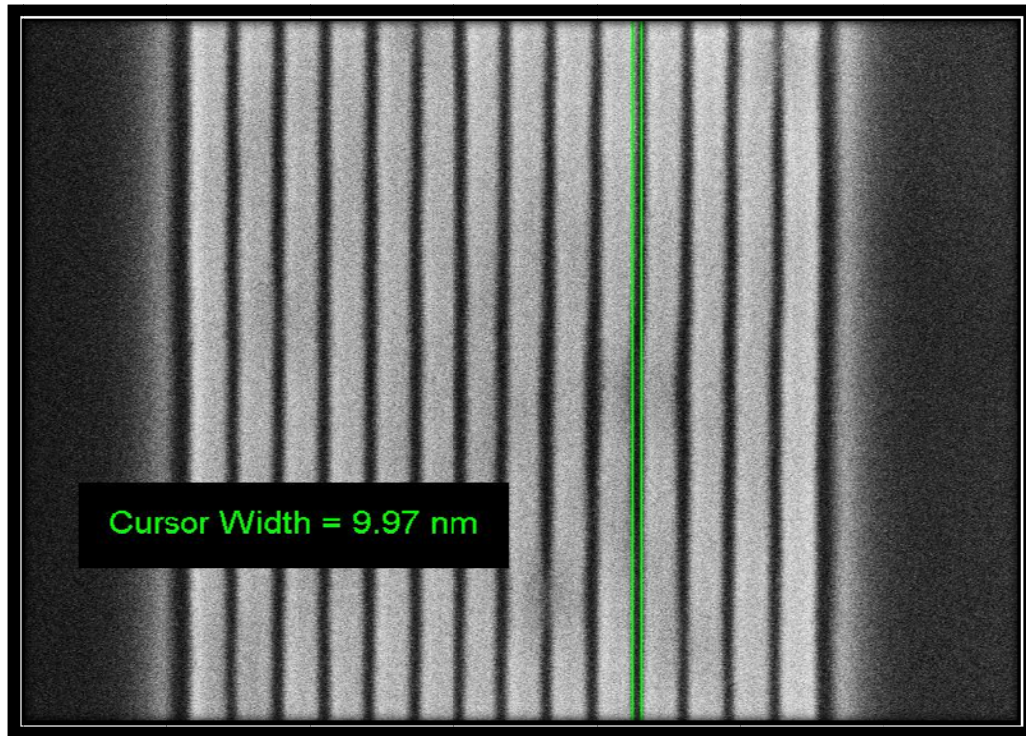
Figure 3.4.6: The feasibility of Discrete Track Recording (DTR). SEM image is showing the line width is sub 10nm and consistency of this result on the entire 4 inch wafer with JEOL JBX 5500FS system. ZEP-520A, JEOL-5500FS, EHT 1.8Kv, Developing condition is MIBK:IPA=9:1 in lower than 10 C, 1 minute and rinse in MIBK:IPA=1:1 in RT 15 seconds.
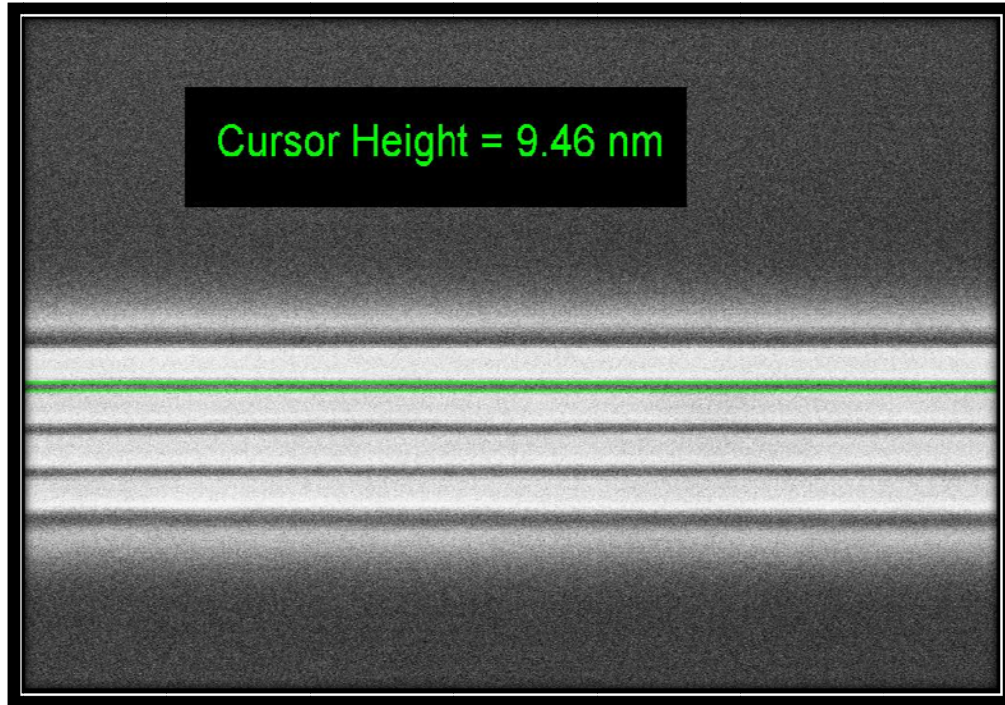
Figure 3.4.7: The feasibility of Discrete Tract Recording (DTR), showing the line width is sub 10 nm. ZEP-520A, JEOL-5500FS, EHT 1.8Kv, Developing condition is MIBK:IPA=9:1 in lower than 10 C, 1 minute and rinse in MIBK:IPA=1:1 in RT 15 seconds.

From the results revealed in Fig. 3.4.6 and 3.4.7 I also demonstrate that lithographic technology has the capability and can be applied to the concept of Discrete Track Recording (DTR) concept. The two experimental results shown above ,are are from positive tone resist, ZEP-520A, and exposing and development conditions are the same for both, 880 μc/cm² dosage, developing for 35 seconds in MIBK:IPA=9:1 diluted developer at 10℃, followed by a rinse for 1 minute in MIBK:IPA=1:1, the resulting line width is bellow 10 nm. The process conditions, used in these experimental results can be applied for pattering an entire 4 inch wafer by lithography, however I did not attempt this as it is tremendously time consuming process.

Chapter 4. 3-Dimensional Multi-Level Magnetic Recording

4.1 Motivations

3-Dimensional multi-level magnetic recording (3D ML) concept can be combined with Bit patterned media (BPM), for further increasing the capability of data storage. It is a quite different approach compared to traditional recording technologies, because it introduces a third vertical dimension approach for storing information in addition to the surface recording with BPM, with 3-Dimensional recording information can be stored in the volume of the recording media. From the illustration in Fig. 4.1.1, it can be seen that stacking more than on single layer could allow to record, store, and retrieve information at the same time, from the same unit surface area of the magnetic deposited specimen. Moreover, this new concept provides opportunities not only for developing superior near future data storage device (3D-ML drive), but also opens up the possibility for exploiting the advantages of an entirely new dimension.

Stacking different multi layers can generally be categorized by two different modes, which are multilevel 3D stacking mode and absolute 3D stacking mode. First in multilevel 3D stacking, the embedded signal recording and reading back processes, from the stacking multi-levels are clearly defined by the recording head spot size, which located exactly above the stack. In this case, the data in all N layers located vertically contribute to one particular signal. Therefore, the number of signal levels (L) is showing the different magnetic layers (N) and can be controlled by the stack number of fabricated 3D media, for which the magnetizing layers are showing a distinguishable signal with adequate SNR for different L levels. The effective density

in this case will be increased by a factor of Log_2 (L) with respect to the density of the single layer, which only has binary signals. On the other hand, the absolute 3D mode in the N layer media only shows the different signal separately. Therefore, with 3-D multi-layer recording, for given areal density data storage would increase by a factor of N, compared to the same areal density of the equivalent single layer media.
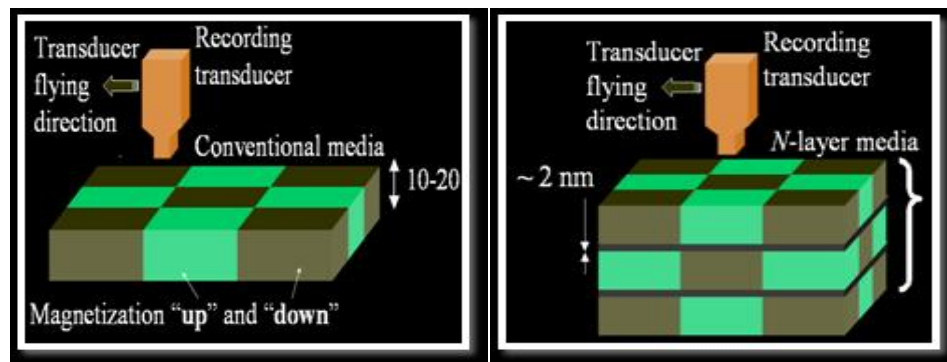
Figure 4.1.1: The schematic conceptual illustration with conventional recording system from left and new suggestion concept of three dimensional magnetic recording systems (3D-ML) and the thickness of stacking may change depending on the purposes.

In this dissertation, I chose Co/Pd-Co/Pt multi-layer from among the different candidate magnetic materials because it has been extensively studied, and its structural properties are well known and established. Meanwhile, I focused my research effort on investigating many process variables such as main chamber pressure, roughness of surface topography, capping layer thickness, seed layer thickness, and number of different bi-layer selections for achieving the optimal performance for high density magnetic structures. I will discuss the results from those mentioned experiments in the following section.

4.2. 3-Dimensional Multi-Layer Materials and Fabrication

Among the next generation alternative technologies for high areal density recording is HAMR method, which employs a locally heated spots of several nm sizes, by the near field regime with laser, in order to bring down the coercivity value of highly anisotropic materials, such as FePt-L10 material [45]. Since the stability of individual recorded bits is directly proportional to the effective anisotropy of the magnetic materials and the effective volume of each grain, it is possible to scale down the grains sizes and thus increase the areal density in a HAMR system.

However, 3D-ML recording provides a further possibility of increasing the areal density by fabricating the media with isolated magnetic layers exhibiting a range of Curie temperatures, resulting in Curie temperature gradient across the thickness of the 3D ML media. In this dissertation, I will discuss the practical method to increase the number of individual layers with varying coercivity in a Co/Pd and Co/Pt multi-layers, with interlayers between layers, sufficient to satisfy two prerequisites. First, interlayers must demonstrate perfect exchange decoupling. And secondly, serve as a good heat conductor. For satisfying those constraints, MgO is a good candidate material as interlayer. An optimization in the heat transfer can also be improved by bit patterned media concept.

The advantages of Co/Pd and Co/Pt 3-dimensional multilayer are they are magnetically coupled in one single layer (in-plane), and between the layers; those materials can be magnetically decoupled from multilayer.

For effective deposition of decoupled magnetic layers on the substrate, the fabrication conditions and media composition have been investigated for the 3D ML media. Each layer must have different magnetic coercivity value for the decoupling effect. This

coercivity factor depends on the substrate composition and surface properties, seed and capping layers thickness, process pressure, and Co/Pd bi-layer thickness. For analyzing the coercivity dependence on all those conditions, dual layer of Co/Pd multi-layer stack were fabricated and characterized. The hysteresis of Co/Pd dual layer were measured by Magneto Optical Kerr Microscopy (MOKE) and Vibration Sample Magnetometer (VSM) respectively, and the media composition analysis was performed by Energy Dispersive Spectrometer (EDS). The pressure in main deposition chamber could be another parameter affecting the magnetic coercivity in each layer. Pd interlayer of about 3 nm was sufficient to perform a perfect exchanging decoupling between the magnetic layers. Illustration 4.2.1 shows the topographical specimen differences due to the different deposition pressure of seed layer and capping layer. In the case of the image on the left 5 mTorr pressure was used, which resulted in larger size of magnetic domain compared to the result with 15 mTorr pressure, shown in the image on the right. Due to the large size of magnetic domain occupied entire sample substrate, its coercivity might be lower than the right side image. In order to high coercivity, left image has higher frequency changing of magnetization than previous image.
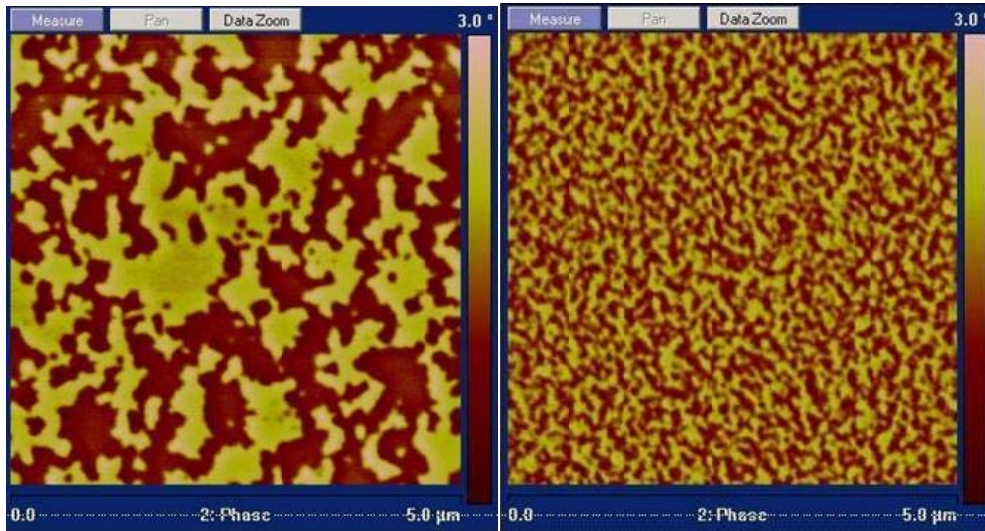
Figure 4.2.1: The topographical differences of seed layer and capping layer based on different deposition pressure. Left image is from 5 mTorr and right is under obtained from15 mTorr pressure conditions.

Another factor to consider is, the coercivity can increase as the main vacuum chamber pressure goes up, and the relationship between the two is summarized in the graph shown in Fig.4.2.1.
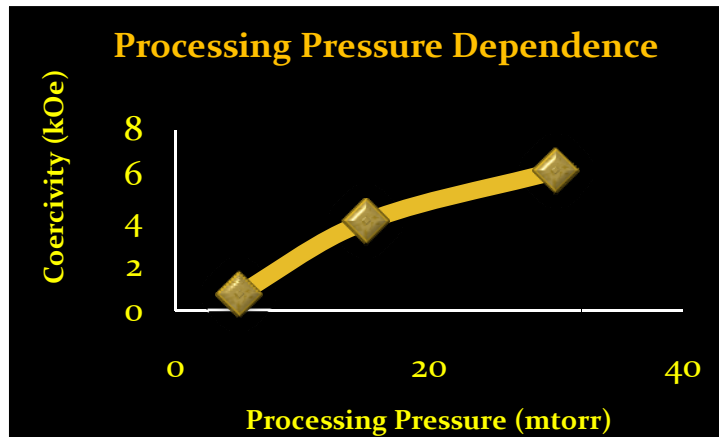
Graph 4.2.1: The proportional trend of coercivity increasing in high processing pressure condition.

In this experiment, the relationship between coercivity value and the thickness of seed and capping layers is also another important factor to be considered. The seed layer compositions are set as Pd(X nm)/{Co(0.36nm)Pd(0.55nm)}x7/Pd(5.3nm), the

following values are used for the variable X; 2.5, 5, 7.5, 10, 15, 20 and 32 nm thickness. The result is shown in the graph of Fig. 4.2.2, the 5nm seed layer thickness gives the highest coercivity value.
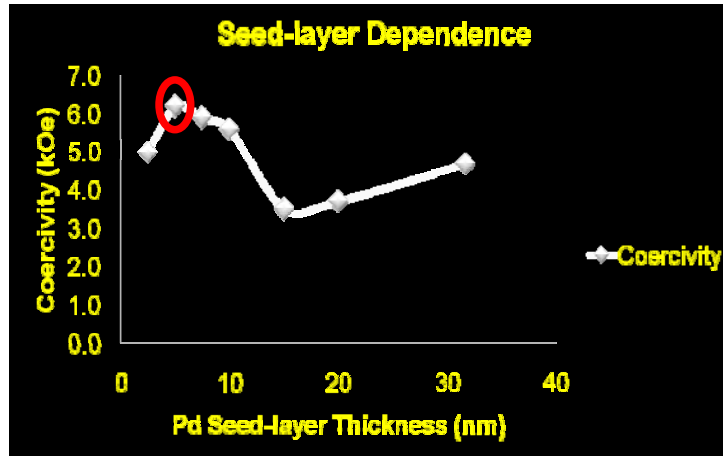
Graph 4.2.2: Coercivity dependence on Pd seed layer thickness (nm) in Co/Pd multilayer media.
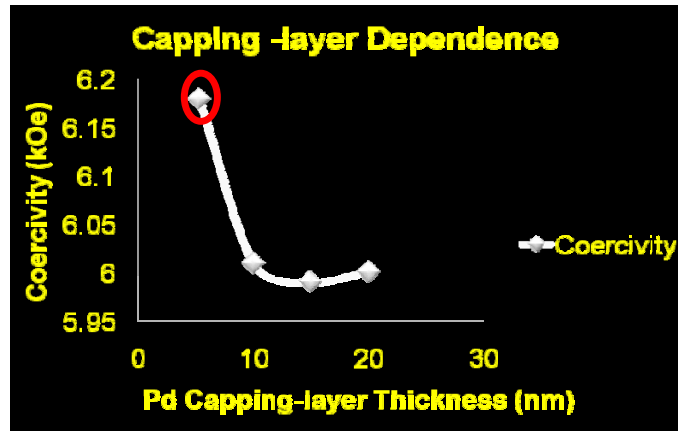
Graph 4.2.3: Coercivity dependence on Pd capping layer thickness (nm) in Co/Pd multilayer media.

After acquiring the coercivity dependence on the Pd seed layer thickness, the relationship between capping layer thickness and coercivity was also established and the results are shown by the graph in Fig. 4.2.3.

The experimental compositions used are Pd(5 nm)/{Co(0.36nm)Pd(0.55nm)}x7/Pd(X nm), and the thickness of Pd is changed to 5.3, 10,15 and 20 nm, and from the result it can be seen that 5.3 nm Pd thickness can achieve highest coercivity.

Also graph 4.2.4 shows the optimal condition of Co thickness for obtaining high coercivity value, in this case 0.25 nm thickness was selected.
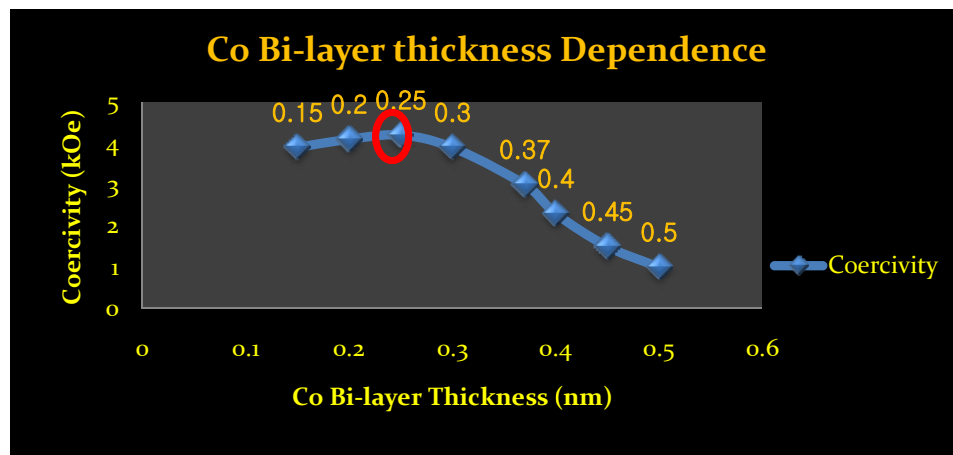
Graph 4.2.4: Coercivity dependence on Co bi-layer thickness, in Co/Pd multilayers media.
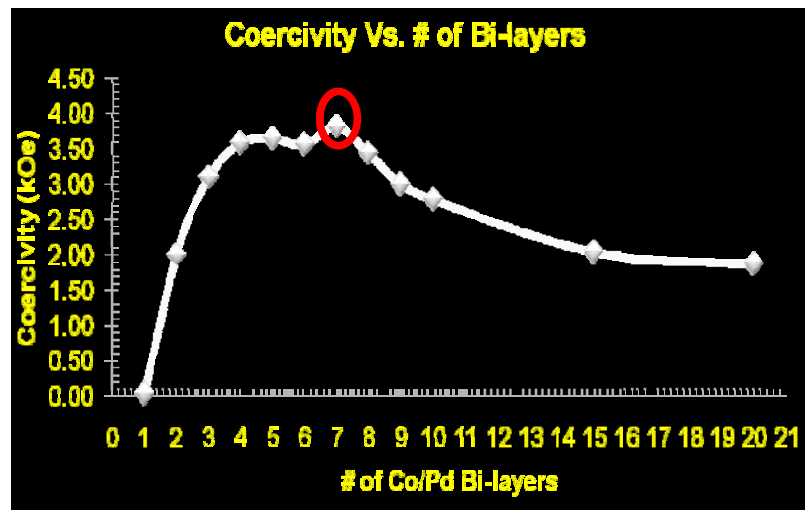
Graph 4.2.5: Coercivity dependence on the number of bi-layers in Co/Pd multilayer media.

62
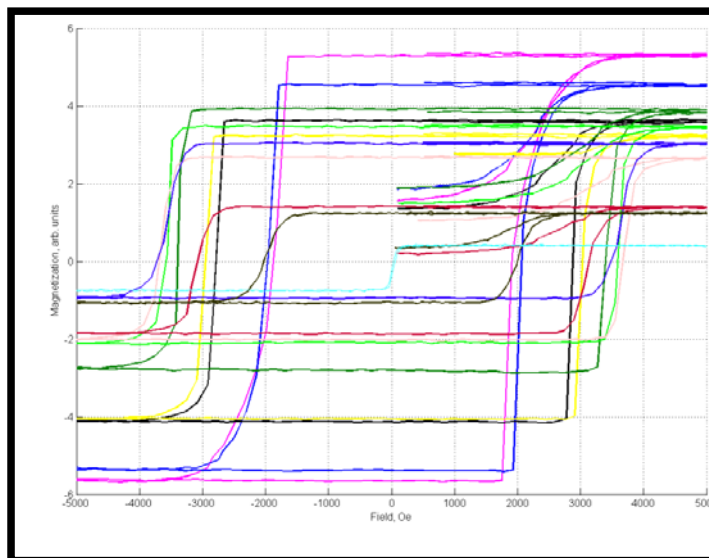
Graph 4.2.6: Hysterisis curve result of the number of Co/Pd bi-layers from MOKE.

Graph 4.2.5 and 4.2.6 show the optimal conditions for obtaining high coercivity results. The experimental procedures used are as follows, on the silicon substrate, I deposited Pd(5nm)/{Co(0.25nm)/Pd(0.55nm)}x(X)/Pd(5.3nm) and changed the number of bi-layer from 1, 2, 3, 4, 5, 6, 7, 8, 9, 10, 15, 20 different stack experiments, and I found that 7 bi-layer stacks are giving proper results.
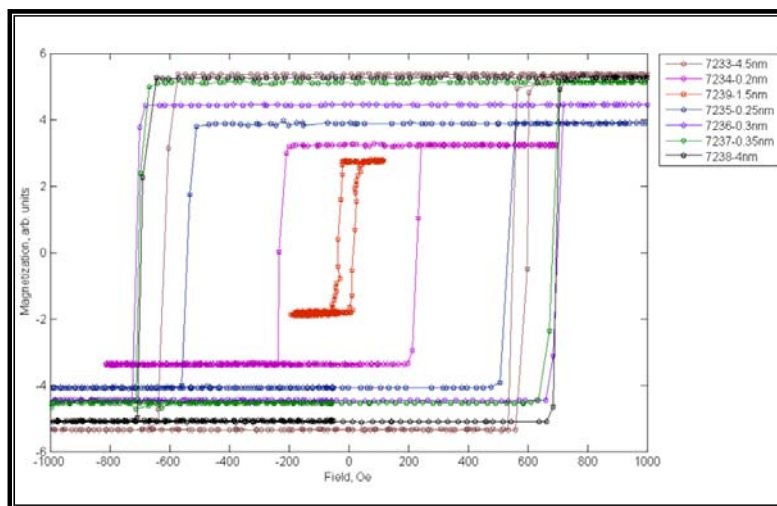
Graph 4.2.7: Co/Pt multi-layer hysteresis results. showing 0.3 nm has the highest coercivity.
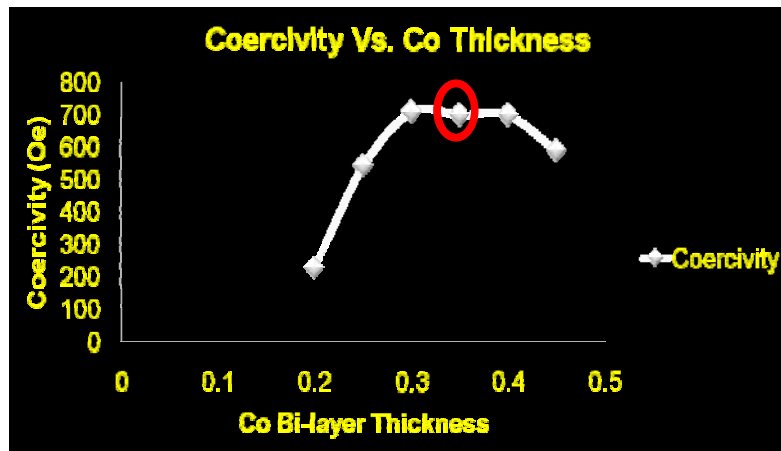
Graph 4.2.8: Coercivity results from Co thickness variation.

I also need to characterize Co/Pt condition with the rest material composition remaining the same. So, I experiment Co thickness from 0.15, 0;2, 0.25, 0.3, 0.35, 0.4, 0.5 nm in Ti(4nm)/Pt(5nm)/[Co(X nm)/Pt(0.55nm)]X7/Pt(5nm). And from graphs in fig 4.2.7 and 4.2.8, it is revealed that the 0.3 nm thickness of Co possesses highest coercivity.

According to the conclusion from all experimental results, I deposited Co/Pd, Co/Pt multilayer following these conditions. The main deposition chamber pressure was selected 15 mTorr, even high coercivity can achieve as increasing the main chamber pressure, but I also consider the mechanical limitation in order not to break the main shutter in chamber. The thickness of seed and capping layers selected were 2.5 nm and 5.3 nm, respectively. Because of the highest coercivity can be obtained with 0.25 nm thickness, Co bi-layer is deposited at this thickness. Finally, the number of Co/Pd bi-layers need to be selected for the highest coercivity value, based on the results of that experiment, I found 7 stacks have the highest coercivity.

In summary, the deposition composition of Co/Pd, Co/Pt are Pd(5nm)/{Co(0.25nm)/Pd(0.55nm)}x(7)/Pd(5.3nm),Ti(4nm)/Pt(5nm)/[Co(0.3 nm)/ Pt(0.55nm)]X7/Pt(5nm) respectively, deposited at 15 mTorr pressure .

Chapter 5. Bit Patterned Media Procedure

5.1 Motivation

I found the proper materials needed and the optimal processing conditions for realizing Bit patterned media. Moreover, I concluded that negative polymer results are better than positive tone resist and also adequate for fabricating the high areal density magnetic material. Even though, 3-dimensional magnetic multilayer concept shows enough feasibility of extending the magnetic recording capacity, I found that the Bit patterned media concept has higher potential in improving capacity, by segregating and reducing the noise and increasing SNRs in each bit of data.

Therefore, I discuss the combination of BPM and 3-D ML concept in this chapter. Briefly, figure 5.1.1 shows the bit patterned media result from Atomic Force Microscopic (AFM) analysis, and this topographic analysis shows perfect segregation of each dot. Moreover, Magnetic Force Microscopic (MFM) scanning shows bright dots and dark dots after depositing magnetic multilayer stacks followed by the result of chapter 4.
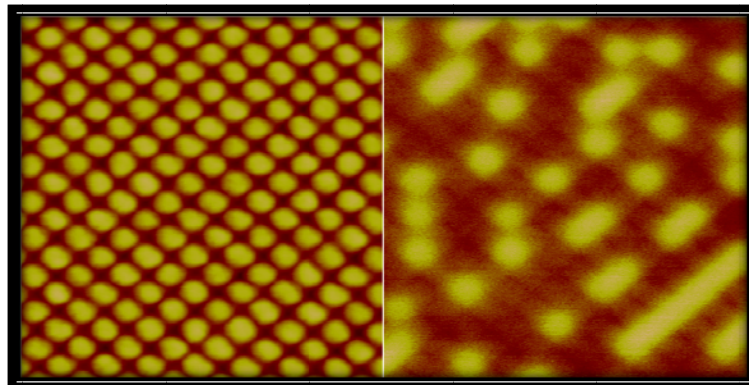
Figure 5.1.1: Image of bit patterned media result from Atomic force microscopic analysis. The AFM result shows briefly the concept of BPM in left and MFM result in right. Different signals are detected by MFM scanning as bright dots and dark dots are out-of-plane signal and down signal respectively. For understanding little bit easier of the signals, Bright dots are representing 1 and dark dots are showing 0.

5.2 Combination of Dual Layer with Co/Pd and Co/Pt

As mentioned in the previous chapter, I obtained the optimal conditions of each Co/Pd and Co/Pt components and this chapter I will show the use of those two elements for extending the magnetic recording capability. In implementing this experiment, a two component combination of Co/Pd and Co/Pt has been deposited by sputtering in order to achieve a highly exchanged decoupling between each layer. The two separate compositions of Pt(5nm)/{Co(0.45nm)/Pt(0,55nm)}x7/Pt(5.2nm) and Pd(5nm)/{Co(0.25nm)/Pd(0.55nm)}x7/Pd(5.3nm) were deposited on silicon substrate with sputtering equipment provided by AJA international Co. The fundamental base pressure and the deposition pressure used were 2x10-7 Torrs and 5 mTorr as respectively. The hysteresis coercivity results obtained from these samples are illustrated in Fig. 5.2.1. It can be seen that both magnetic layers can be perfectly magnetic exchange decoupled because Co/Pt has lower coercivity than Co/Pd, and coercivity is a critical factor.
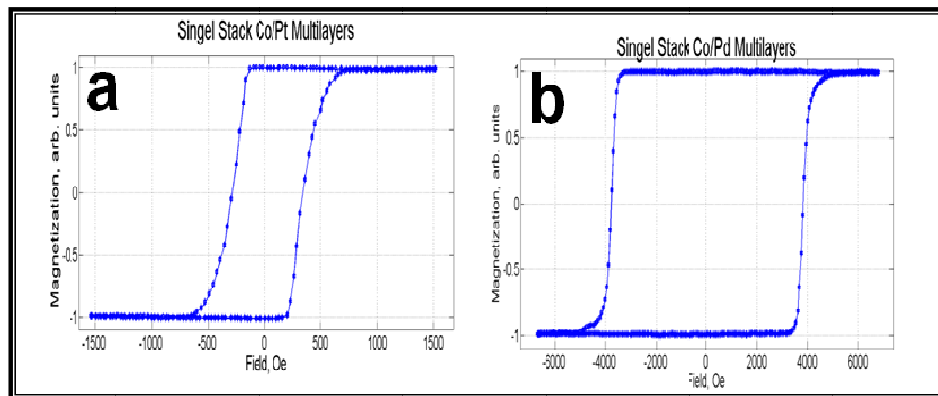
Figure 5.2.1: Hysteresis curve of Co/Pd multilayer and Co/Pt magnetic multilayer layer. Co/Pt hysteresis curve shows lower coercivity than Co/Pd. Both magnetic layers can be perfectly exchange decoupled.

From the combined component recipe of

Pt(5nm)/{Co(0.45nm)/Pt(0.55nm)}x7/Pt(2.5nm)/

Pd(2.5nm)/{Co(0.25nm)/Pd(0.55nm)}x7/Pd(5.3nm), I can identify the perfect

magnetic exchange decoupling between layers, illustrated in figure 5.2.2. The minor

loop, shown in black is Pt_based component, and the main loop (in red) is Pd

related hysteresis curve.
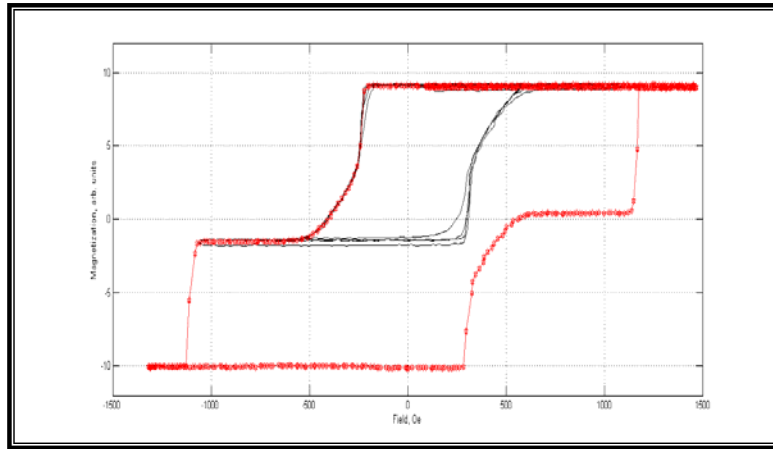
Figure 5.2.2: Hysteresis curve result of Co/Pd-Co/Pt combined multilayer

5.3 Pre-patterned Media Procedures.

Based on the result from chapter 5.2, in this section I will describe process of combining the two. Before delving into the main content of the topic, I will briefly discuss the pre-patterned media fabrication procedures.

Pre-patterned media fabrication starts on Silicon Dioxide substrate. This procedure also can start on silicon substrate, however it would not be affected by Reactive Ion Etching (RIE) processing used for milling the substrate. For that reason, this process can only be accomplished on Silicon dioxide substrate. However, in next chapter, I will suggest innovative procedure to overcome this barrier, called patterned media processing. The first step, after finishing substrate cleaning, is spin-coating ZEP 520A positive tone resist with 5000 rpm/1000 rpm ramping speed for 60 seconds. The resulting positive tone resist thickness is around 27 ~ 34 nm after baking at 180℃ for around 20 minutes.
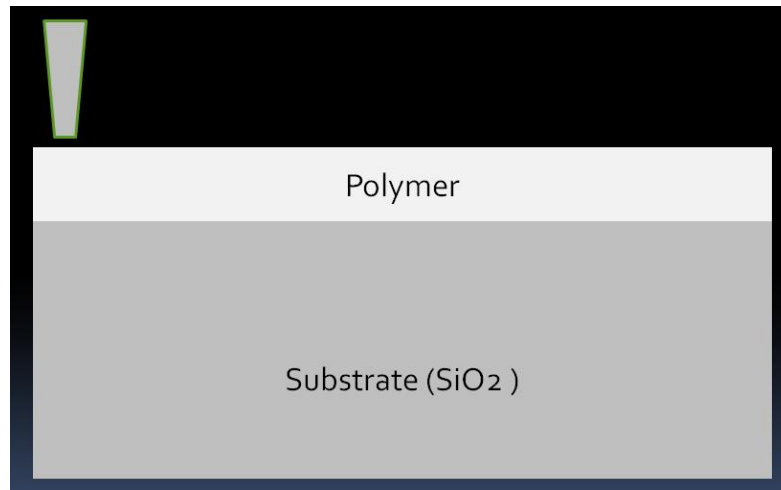
Figure 5.3.1: Spin-coating positive tone resist with 5000rpm speed and 1000 rpm ramping time for 1 minute on SiO$_2$ substrate. Baking at 180℃ for around 20 minutes and its resulting thickness is around 27 to 34 nm, determined by AFM step height analysis.

Next step is lithography exposure with JEOL JBX 5500FS, the dosage used is around 130 µC/cm^2 and beam current is around 98 pA, with beam acceleration intensity of 30 kV. The exposed substrate isthen soaked in MIBK:IPA=1:9 diluted developer, held under 10℃ temperature, for 60 seconds, and then rinsed in MIBK:IPA=1:1 for 15 seconds.
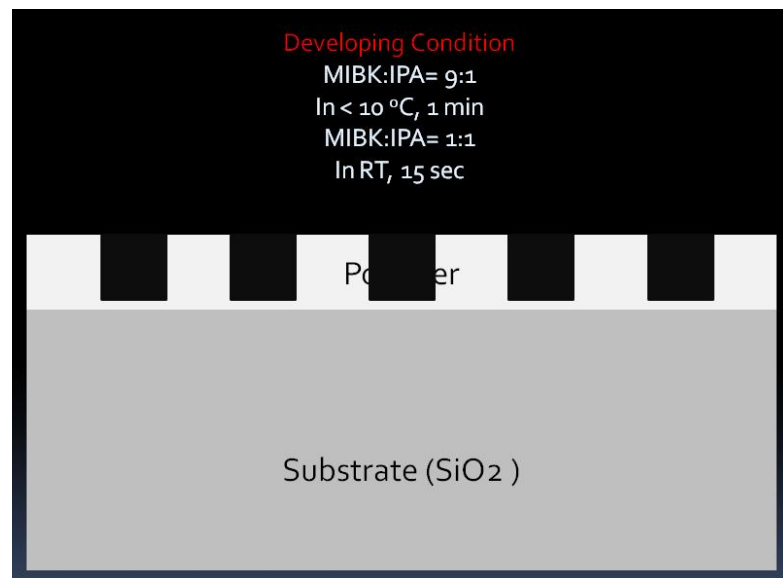
Figure 5.3.2: Developing condition for exposed substrate. Soaking MIBK:IPA=1:9 for 60 seconds and rinsing in MIBK:IPA=1:1 for 15 seconds.

After development processing, substrate is moved to Reactive Ion Etching (RIE) chamber for cleaning processing, because I assume that there is some residue of the positive tone resist left on the SiO$_2$ substrate, after developing process. After a number of experiments the achieved results were below my expectations, and the reason was that the spin coated resist thickness and the step height of exposed pattern after developing showed different thickness. Furthermore, those differences of the gap in step height were ascending when the pattern size exposed was getting smaller. I found that the resist residue is the cause of this problem. So, I decided to use Oxygen

cleaning with RIE. Its conditions were 30 Watt power, with 50 standard cubic centimeters (SCCM), for 8 seconds. The results were confirmed by AFM analysis.
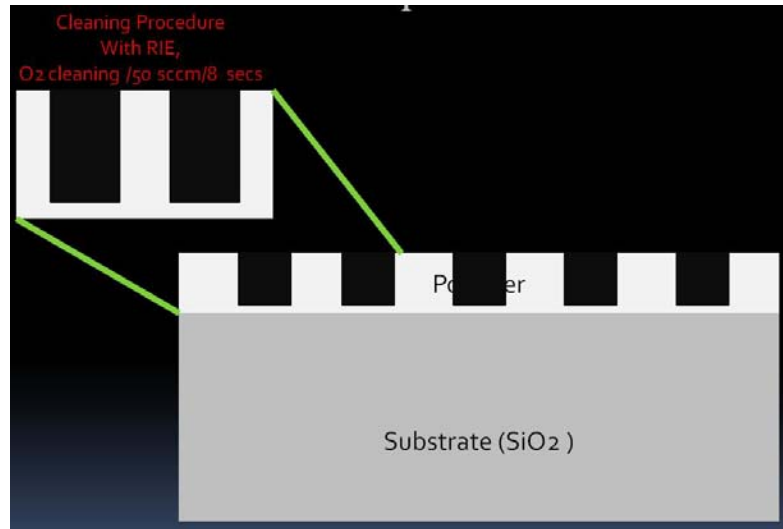
Figure 5.3.3: Reactive Ion Etching process used for cleaning resist residue, because the remaining residue of resist will deteriorate the resulting pattern. Oxygen cleaning is done under 30 Watt, 50 sccm oxygen flow rate, for 8 seconds, at 10^{-9} Torr main chamber pressure.

The substrate was moved to Electron Beam Evaporator (EBE) for deposit protective material layer. In this case, I choose Chromium (Cr) among the other materials because it can be etched very effectively by a wet etchant (5 Å/second). The wet etchant used is capable to remove only Cr without damaging other materials.
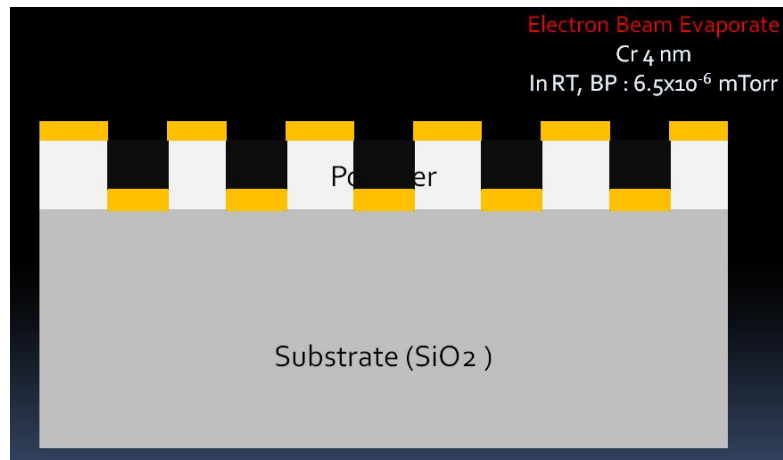
Figure 5.3.4: Schematic diagram of deposition of Cr 4 nm, with Electron Beam Evaporator (EBE). Base pressure is under 10-6 mTorr. Temperature in main chamber is starting from room temperature and is increased to 28℃

The deposition rate and main chamber pressure are very critical parameters which determine the quality of deposited materials. In general, the lower the main chamber pressure and the slower the deposition rate, the higher material quality is achieved. In this case, The EBE main chamber pressure was 6.5×10^{-6} mTorr, starting at room temperature, depositing Cr at 0.1 Å/second rate, which takes 40 seconds to deposit 4 nm. In practice, infinitesimal particles of material, bombarded by the electron beam, are floating into the main chamber even after closing the target shutter, leading to an increase in the effective thickness of the deposited material; therefore, I close the shutter a little earlier before deposition thickness reaches on 40 Å.

The EBE equipment can deposit materials in an anisotropic matter. If the material were deposited by sputtering machine, in the case of which the source of igniting the target is plasma, then the selected material would be deposited on the entire substrate in an isotropic matter, including the sidewalls. In that case, there would be no room for Acetone to penetrate and dissolve the resist and lift-off the materials over the resist.

Figure 5.3.5 shows the result after removing all resist. Cr remains the fully exposed substrate only.
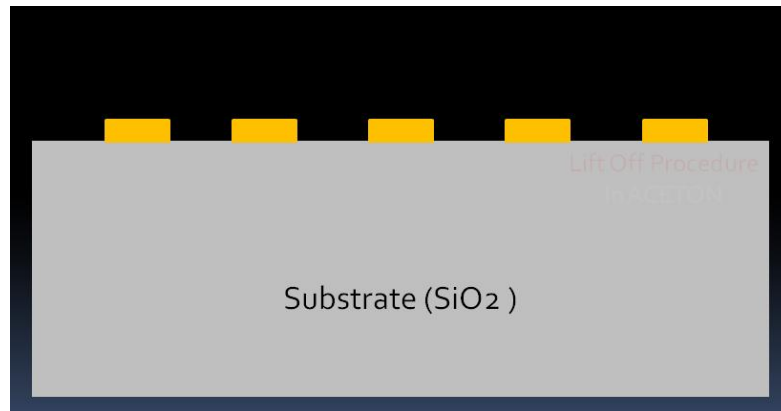
Figure 5.3.5: After removing resist, Cr remains on the fully exposed areas only. Lift off process is done with Acetone and duration is decided by the type of resists and its thickness.

Next step is milling the substrate with RIE. I used this equipment for cleaning processing with Oxygen previously, however in this step, I use higher power and longer duration for paring the silicon dioxide substrate. In this experiment, I confirmed that the Cr material endures until the end of this procedure and successfully serves its role as a mask. RIE milling conditions used were100 Watt power, CHF_3 flow rate of 50 sccm, for 60 seconds, which produced around 90 ~ 100 nm depth of milling. This depth is sufficient step height for the next step.

Figure 5.3.6: Main milling processing with RIE. Silicon dioxide substrate is milled under 100 Watt power for 60 seconds, with CHF$_3$ of 50 sccm. The depth of milling is around 100 nm confirmed by AFM analysis.
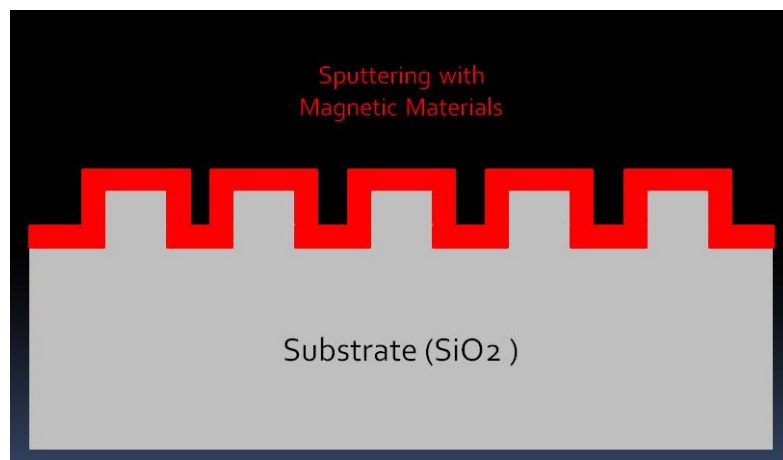
Figure 5.3.7: Final step in prepatterned media processing. Deposition, by sputtering, of magnetic materials depending on the purposes. In this experiment, I deposited dual magnetic layer based on the Co/Pd-Co/Pt magneteic layer following the previous results.

Sputtering deposition is of magnetic material is the final step. According to the the results shown in the previous sections, I sputtered Co/Pd-Co/Pt dual magnetic multilayer having the results in each multilayers defined as magnetically exchange decoupled. In this case, the intervals of each shutter transition in deposition of magnetic materials is a critical parameter, sputtering shutter control can affect the magnetic film's properties.

5.4. Discuss the Pre-patterned Media Experimental Results.

On the basis of previous results, I did lithography with varying the pattern dimension from 30 nm to 500 nm. In illustration 5.4.1, pattern dimensions are shown as 30, 50, 60, 70, 80, 90 100, 150, 200, 250, 300, and 500 nm, starting from upper left corner. SEM image was taken after development processing of silicon dioxide substrate with positive tone resist, ZEP 520A, having an average step height of around 30 nm.

Figure 5.4.2 shows the results after the milling process in RIE. In this case, much more careful characterization of RIE processing is needed, because this image shows that almost all patterns were produced with exceptional results except for small dimension patterns of size such as 30 nm. However, controlling the amount of CHF_3 gas which reacts with plasma during RIE processing, and also adjusting the adequate milling time for nanometer size fabrication are very difficult. Therefore, an alternative processing technique is required for overcoming this challenge.

The image of the result of sputtering magnetic materials, discussed in the previous chapter, which is based on Co/Pd-Co/Pt dual multilayer, is shown in Fig. 5.4.3. Due to the sputtered magnetic material amount, each pattern dimensions are getting bigger than the initial dimensions. This is also another problem in this pre-patterned media processing.
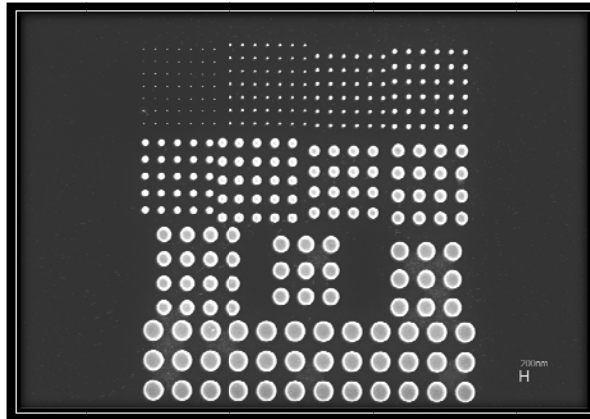
Figure 5.4.1: SEM image after development processing. Pattern dimensions vary and start from top left corner as 30, 50, 60, 70, 80, 90 100, 150, 200, 250, 300, and 500 nm respectively.
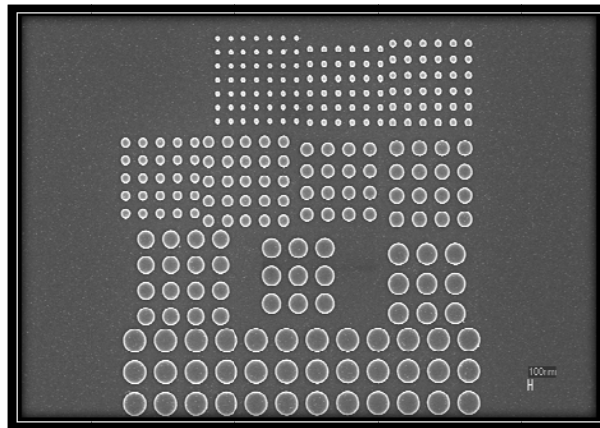
Figure 5.4.2: SEM image from RIE milling processing. Small dimensional pattern, 30 nm, vanishes under these processing conditions of 100 Watt, 60 seconds, and CHF_3 plasma. Each pattern has around 100 nm milling depth and was analyzed by AFM.
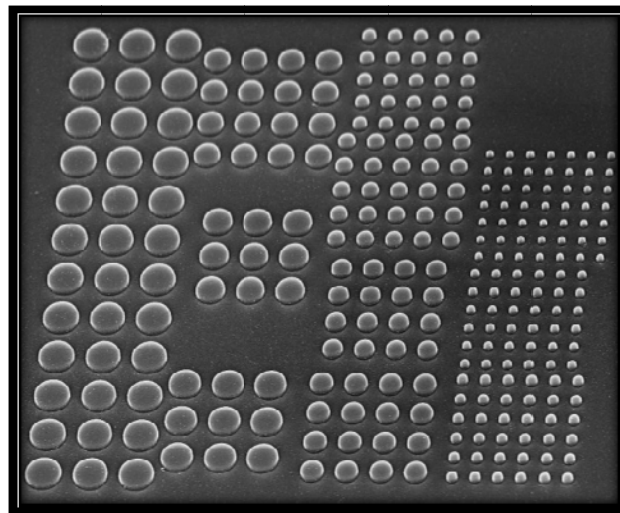
Figure 5.4.3: 45° tilted SEM image after sputtering dual multilayer magnetic materials based on Co/Pd-Co/Pt. Each pattern dimensions become bigger than original pattern dimensions.

Figure 5.4.5 and 5.4.6 are the core results of this entire experiment. Figure 5.4.5 shows Atomic Force Microscopic (AFM) and Magnetic Force Microscopic (MFM) analysis. In this case, I analyzed the 60 nm dimension patterns, where red line presents AFM, green line   indicates MFM result. According to the MFM result, the magnetic dual multilayer substrate represent three distingusiable signals, the coresponding magnetic signals are shown by the dotted red arrows in the graph on the left of Fig. 5.4.5. In thoery, four different magnetic signals can be presented in dual multilayer, this is illustrated in figure 8.4.4.
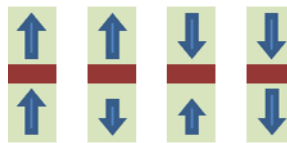
Figure 5.4.4 : Corresponding to the hysterisis curve, four different magnetic signals may be presented in dual magnetic multilayer. I present these signals as up-up, up-down, down-up and down-down as respectively.
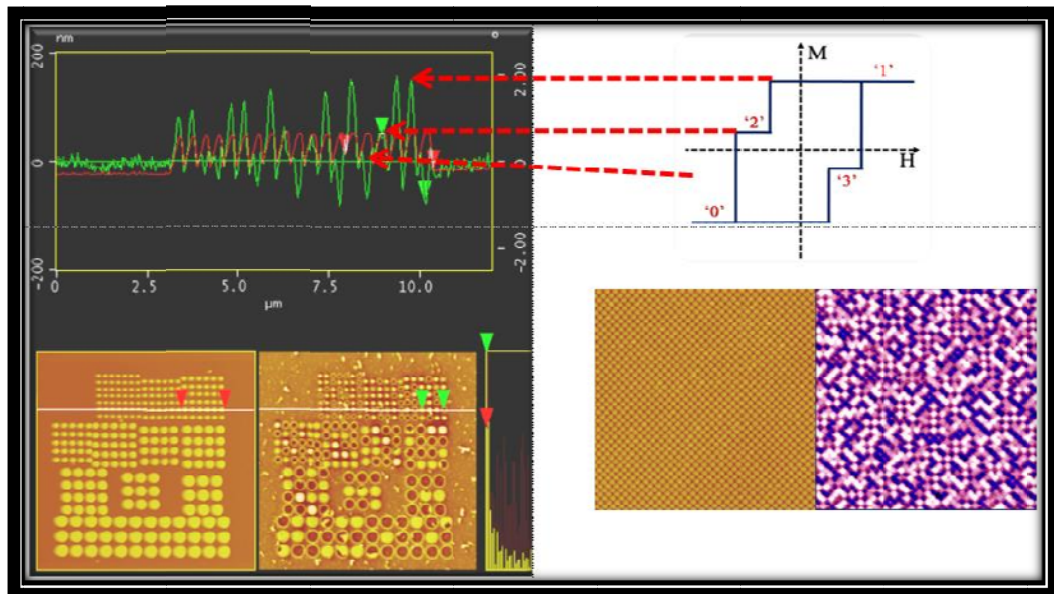
Figure 5.4.5: AFM and MFM analysis. Red solid line in upper left image is topographic results from AFM and green solid line is from MFM analysis. In MFM analysis, magnetic dual multilayer shows distinguishable signals corresponding to theory in right upper figure. Extending the pattern area to 10x10 μm^2 with same conditions, the magnetic signals are showing different levels in right bottom image.

However, experimental result show only three different magnetic signals from the MFM analysis in figure 5.4.5, this is due to two signals, up-down and down-up, merging together, and located within the threshold for distinguishing the magnetic signal. For this reason, magnetic signals only exhibited three different signals. I implement same processing and increase the exposed area as 10x10 μm^2 in order to ensure this theory and convert MFM image into gray image. The image bellow is used to represent the magnetic signals much clearer.
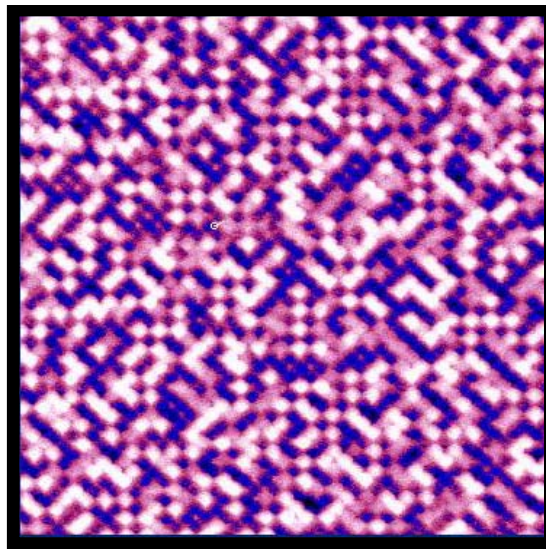
Figure 5.4.6: Enlarged image of 10x10 μm^2 exposed area from figure 5.4.5. Image converting by the contrast and it shows more clearly levels of magnetic dual multilayer.

Furthermore, let me extend this concept to the triple multilayer based on the Co/Pt-Co/Pd-Co/Pt magnetic materials. It shows different coercivity from the analysis of MOKE or VSM, this magnetic medium can have eight different magnetic signals as it can be seen from the VSM analysis in Graph 5.4.1, which gives the possibility of extending this idea. From the main until minor loop, coercivity can show enough different signals to distinguish the magnetic levels.
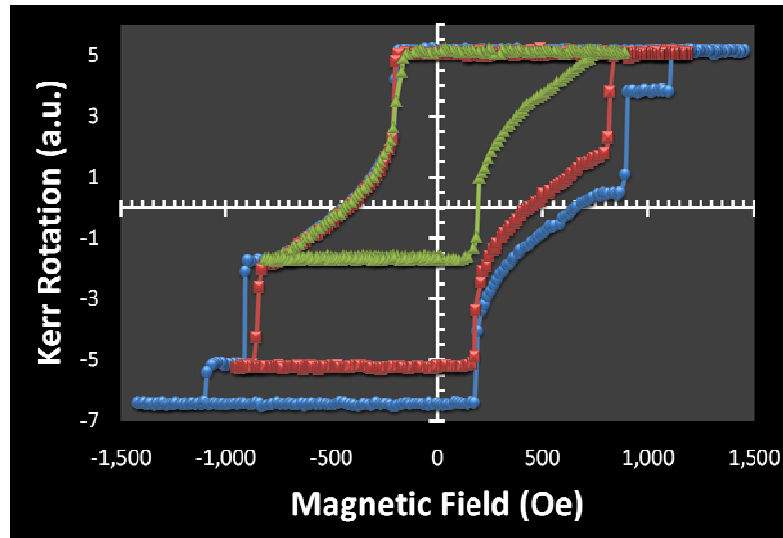
Graph 5.4.1: Three hysteresis curves based on Co/Pt-Co/Pd-Co/Pd multilayers. This medium may be able to show 8 different magnetic signals.

Figure 5.4.7 is SEM image of final result of prepatterned media processing. Sputtering height of triple multilayer magnetic material based on Co/Pt-Co/Pd-Co/Pt is around 40 nm. So, the original pattern dimension is 10 nm and the distance between dots is around 250nm.

Figure 5.4.8 shows AFM and MFM images, indicated with red and green arrows, respectively. Based on the MFM analysis, background noise on magnetic material sputtered medium is exceeding the tolerance degree, preventing magnetically coupled bits from patterning even after performing the demagnetization processing. For this reason, Prepatterned media processing is not a suitable method for increasing the magnetic storage capability.
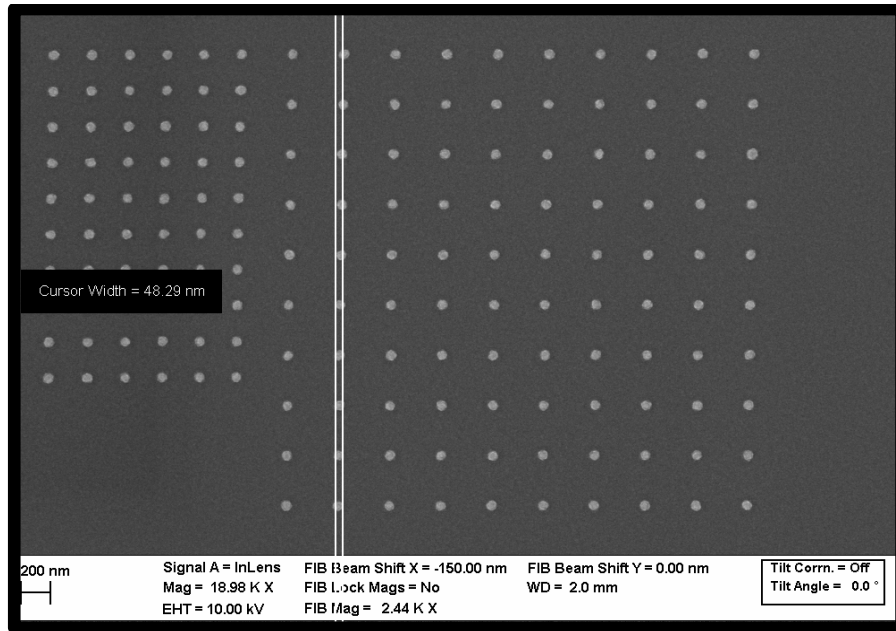
Figure 5.4.7: SEM image of final result with prepatterned media processing. Sputtering height of three multilayer magnetic materials based on Co/Pt-Co/Pd-Co/Pt is around 40 nm. The original pattern dimension is 10 nm and the distance between dots is around 250nm.
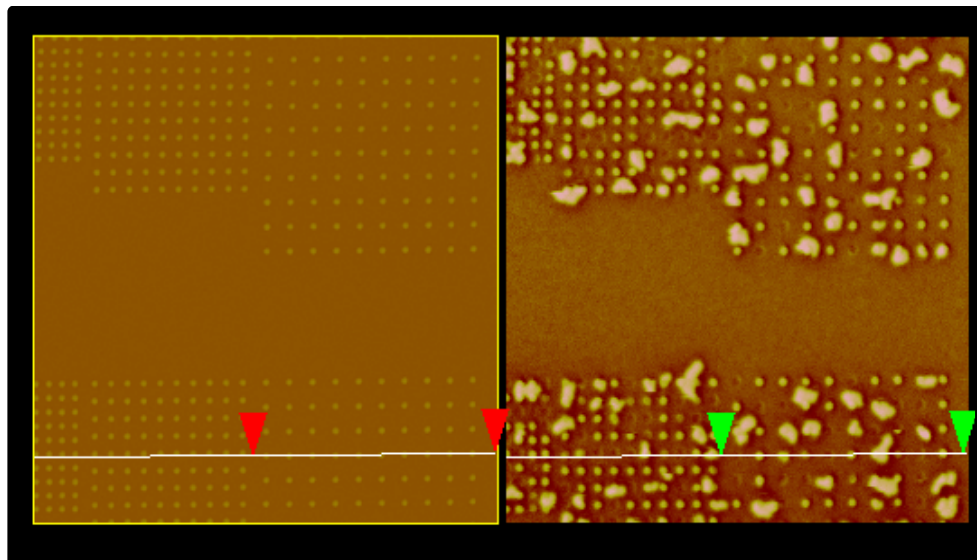
Figure 5.4.8 AFM and MFM image with red and green arrows, respectively. According to the result of MFM analysis, background noise on magnetic materials sputtered medium is exceeding the tolerance, allowing the magnetically coupled bits even after demagnetization processing and this is one of critical barrier for pre-patterned media processing.

80
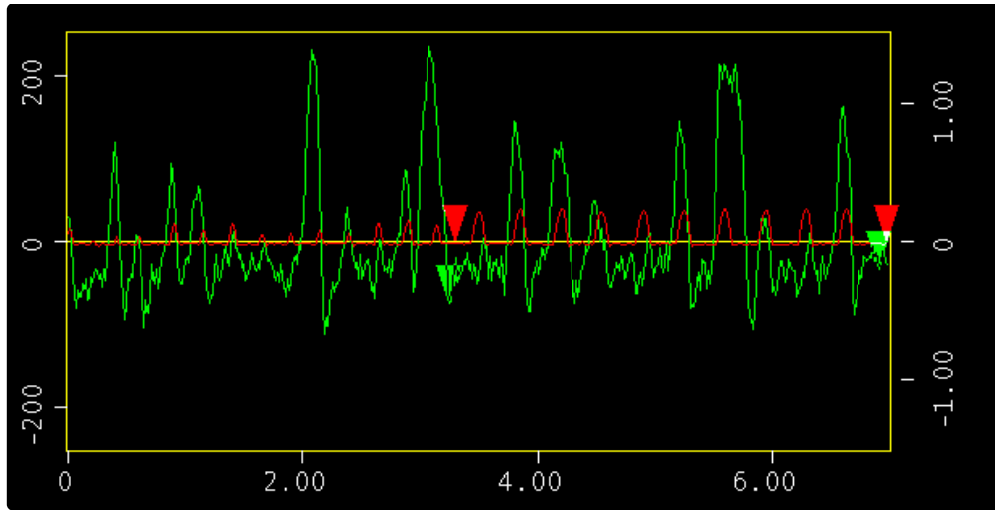
Figure 5.4.9: AFM and MFM analysis corresponding to the area measured in figure 5.4.8. Green line shows MFM and red line shows topographic result, respectively.
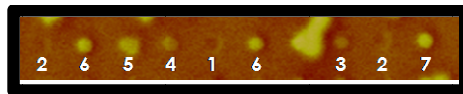
Figure 5.4.10: MFM result from the measured line from figure 5.4.8. this area's magnetic signals have seven different levels by checking the brightness differences and can be confirmed by the magnetic signal measurement from figure 8.4.9.

Figure 5.4.9 is AFM and MFM analysis image corresponding to the measured area which was designated in figure 8.4.8. Green line shows MFM and red line shows topographic result, respectively. MFM result from figure 5.4.10 shows magnetic signals display seven different levels, with checking by brightness differences, one signal cannot be distinguish as having unique magnetic level and also cannot be confirmed by the magnetic signal measurement from figure 5.4.9, because the highest and lowest vortex points in green lines are not precisely defined in the 6th signal. To make matters worse, for detecting the eight different magnetic levels, one pattern was affected by the background noise and lost its own dimension.

Based on all those results, I can conclude three-dimensional magnetic multilayer with bit patterned media can display the feasibility of extending magnetic recording capability. Moreover, I experimented with dual multilayer and triple multilayer for extending the theoretical knowledge and presented the result of distinguishable magnetic signals with AFM, MFM, MOKE and VSM analysis. However, prepatterned media method for achieving bit patterned media also has many technical challenges. First, lift off processing should be done in order to achieve small dimension patterns, such as bellow 50 nm. However, as I mentioned before, it is really hard to achieve in practice due to the RIE process and so on. Another reason for the necessity of alternative method is that the final pattern's dimensions exhibit larger than the original size due to the magnetic materials deposition over the final patterns. And finally, background noise is exceeding the tolerance of magnetic bits which was combined with many grains when patterns are getting smaller. I present new procedure with negative tone resist to address this need of a new paradigm.

5.5. Patterned Media Procedures

In this chapter, as mentioned above, I will present a new concept of processing with negative tone resist, hydrogen silsesquioxane (HSQ). By using a different resist I had to redesign the whole process procedure, I started by depositing the magnetic materials on the substrate, followed by spin coating the negative resist on top of them. I deposited triple magnetic multilayer based on Co/Pt-Co/Pd-Co/Pt using the same recipe as mentioned in previous chapter on the silicon or silicon dioxide substrate after completing the substrate cleaning process.

This suggested processing method has more advantages compared with prepatterned media concept, in terms of having less processing steps and lower risk of mistakes. Besides, this processing method has no potential technical barrier for realizing the nano-meter size pattern, because it is not using the lift off process and because it is not covered by magnetic materials, pattern dimensions are huaranteed to remain constant.

Figure 5.5.1 shows the first step in the process, sputtering magnetic materials on top of cleaned silicon or silicon dioxide substrate. In this experiment, I sputtered Co/Pt-Co/Pd-Co/Pt, triple multilayer magnetic materials and spin coated negative tone resist on top of the magnetic materials. In this case, the polymer adhesion property with the magnetic material must be considered. For example, if selecting Pd as a capping layer, negative tone resist will not adhere firmly on the substrate during the development processing. Therefore, Tantalum (Ta) instead of Pd often is used as a capping layer according to the literature. Illustration 5.5.2 is showing the adhesion matter when Pd is used as a capping layer.
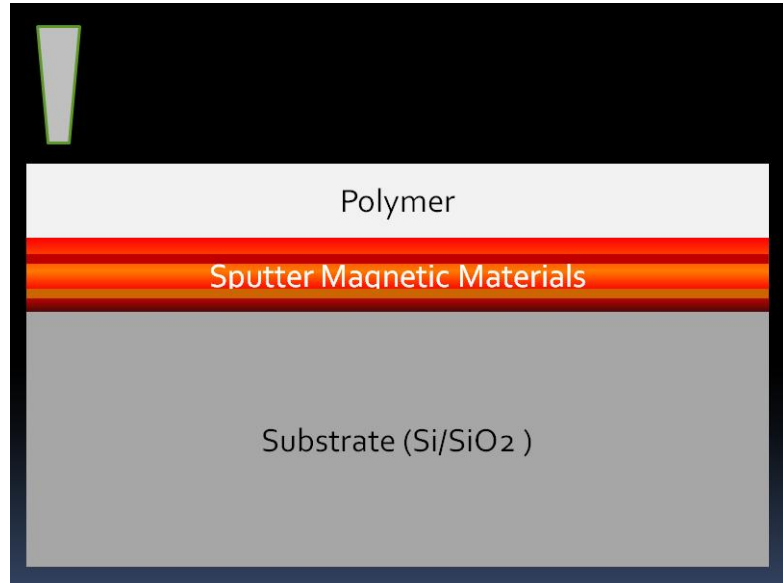
Figure 5.5.1: Sputtering magnetic materials on top of cleaned silicon or silicon dioxide substrate. In this experiment, I sputtered Co/Pt-Co/Pd-Co/Pt, triple multilayer magnetic materials and spin coated negative tone resist on top of the magnetic materials.
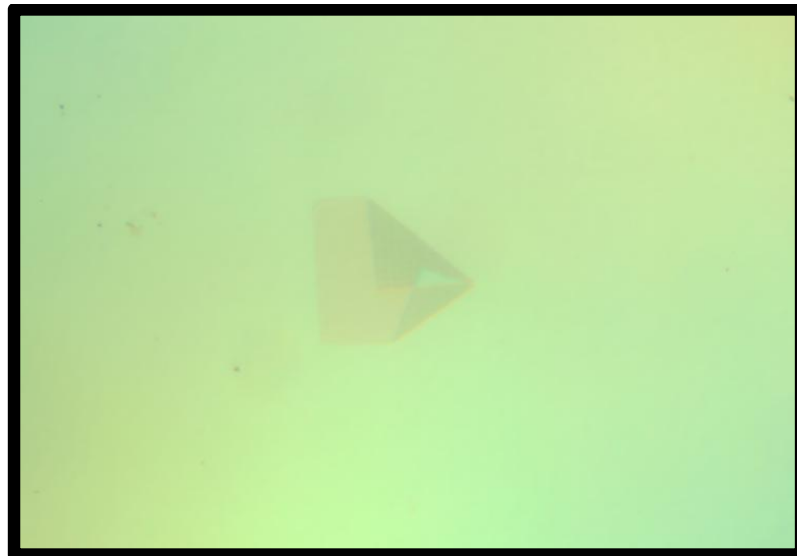
Figure 5.5.2: Using Pd as a capping layer causes an adhesion problem for the polymer on the surface. Exposed negative tone resist peels off after development processing. Image was taken by optical microscopy.

Next step is development processing by immersing the substrate in MF CD-26 for 27 ~ 30 seconds followed by a rinse in IPA and then DI water for 15 seconds and 60 seconds respectively.
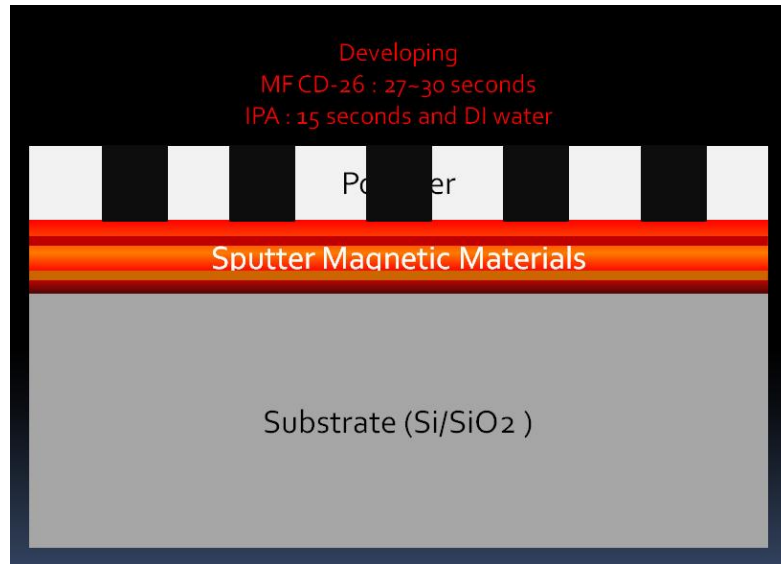
Figure 5.5.4: Immersing the substrate in MF CD-26 in 27 ~ 30 for seconds and rinsing in IPA and DI water with 15 seconds and 60 seconds respectively.

Third step is the main processing stage which can determine the ultimate success or failure of this patterned media method. Figure 5.5.4 shows Ar^+ milling processing with Induced Coupled Plasma (ICP). Unlike RIE, ICP with the ionized plasma can use a voltage bias and bombard the substrate. While processing, the voltage bias is maintain around 300 Volts. For the triple multilayer magnetic thin films, Co/Pt-Co/Pd-Co/Pt, with Ta capping layer, ICP runs 6 minutes, without affecting the negative tone polymer as mask, while completely milling the Ta capping layer. Though Ar^+ milling process is quite traditional way, its performance results are better than other methods such as using SF_6, or other chlorine (Cl) based-gases. The negative tone resist cannot withstand the SF_6 plasma and can be easily removed from the substrate. Other

possible gases are less desirable because of the health hazards associated with them. For that reason, traditional Ar $^+$ milling processing was selected even though the roughness of substrate surface was poor.
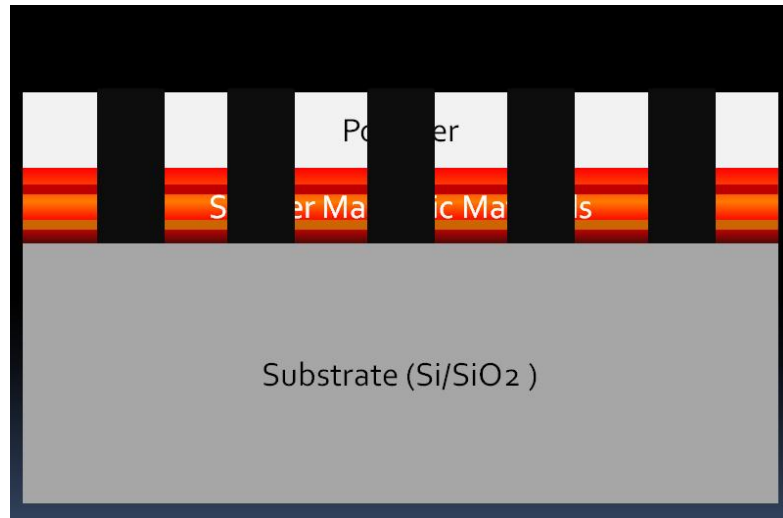
Figure 5.5.4: Ar$^+$ milling processing with Induced Coupled Plasma (ICP). Based on Co/Pt-Co/Pd-Co/Pt with Ta capping layer, ICP runs for 6 minutes, without destroying the negative tone polymer as mask while completely milling the Ta capping layer.
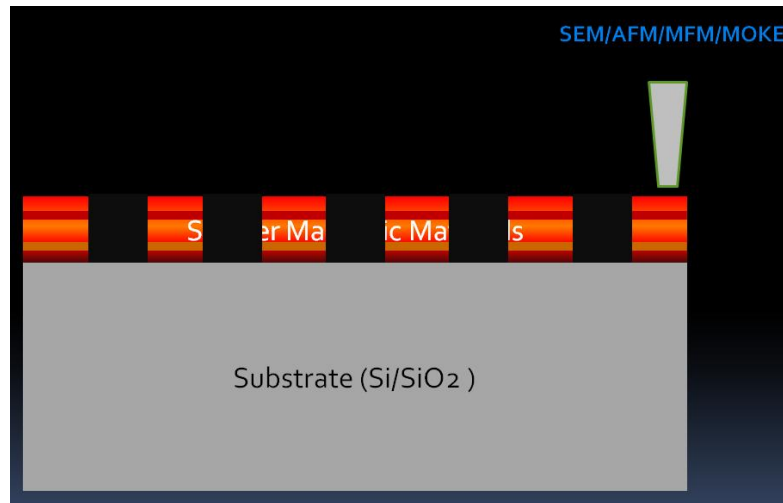
Figure 5.5.5: Analyzing the substrate after milling processing by SEM, AFM, MFM, and MOKE.

5.6. Discuss the Patterned Media Experimental Results

In this chapter, I will discuss the capability of extending the triple multilayer concept in patterned media processing. I applied 8-level Co/Pt-Co/Pd-Co/Pd based multilayers and the hysteresis result from that is shown in graph 5.6.1.
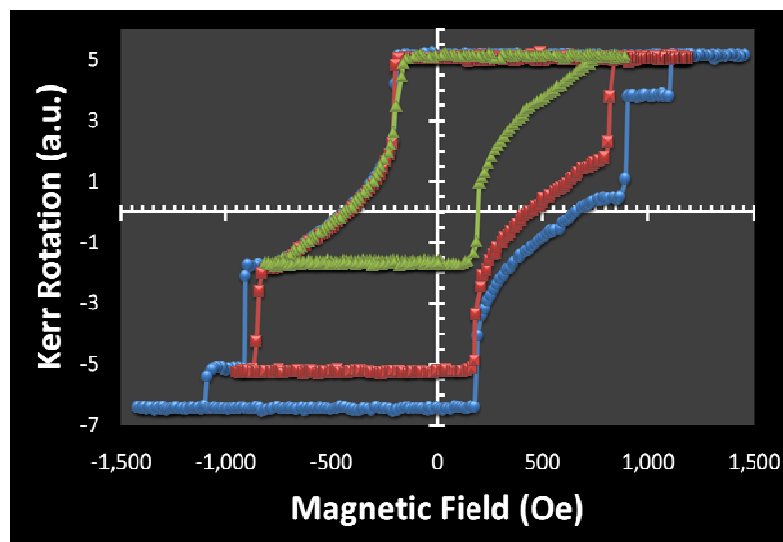
Graph 5.6.1: Hysteresis curves of three multilayers based on Co/Pt-Co/Pd-Co/Pd multilayer. This magnetic thin film is capable of showing 8 different magnetic signals.

Although, in figure 5.6.1, pattern dimension have the same size of 125 nm, distance between dots is increasing by 10 nm steps from left to right. Figure 5.6.2 is corresponding to figure 5.6.1 and showing AFM and MFM results after demagnetization processing. From MFM result, it can be concluded that the patterned media procedure realizes no background noise. For that reason, patterned media method is quite close to extending the storage capability in magnetic storage system.
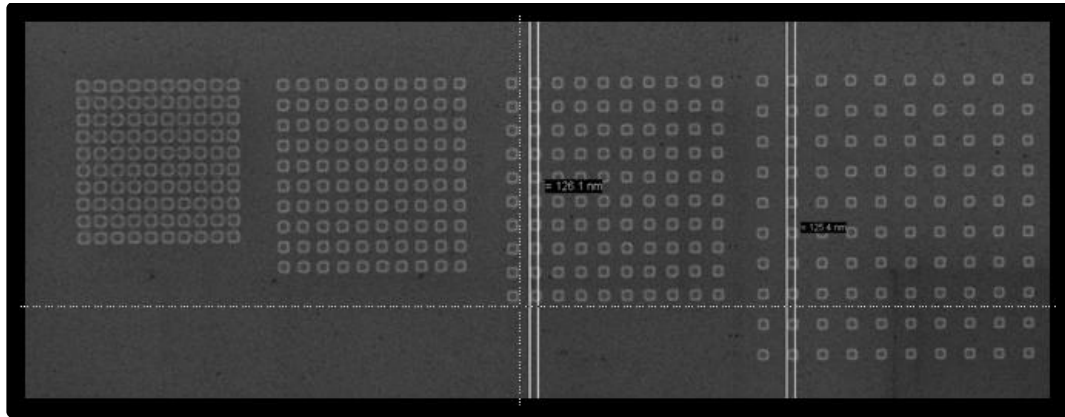
Figure 5.6.1: SEM image and pattern dimension is around 125 nm. Though dimension perform same size its distance between dots are increasing from left pattern to right.
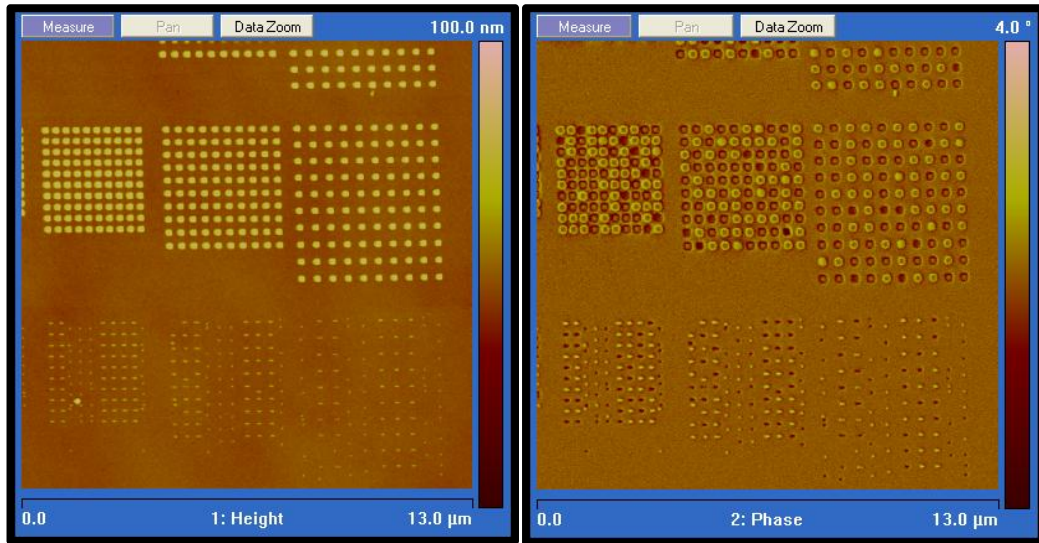
Figure 5.6.2: Corresponding AFM (left) and MFM (right) results after demagnetizing same area from figure 8.6.1. Patterned media procedure may not be concerned background noise and it is the most advantage for selecting this method.

Illustration 5.6.1 and 5.6.2 are SEM image and pattern dimension is around 125nm and the distance between dots are increasing from left pattern to right pattern even dot size was fixed and measuring same area magnetic properties with AFM and MFM methods which demagnetized the pattern's magnetization in order to eliminate the background noise. The pattern's size of MFM result looks like bigger than the original size because MFM probe start to scan a magnetization field in each pattern, it also

detect the field from the pattern's sidewall. Therefore, applying adequate probe with high sensitivity and high coercivity is very important. Especially, high sensitivity probe can resolve the image resolution when it detect high dimensional patterns and high coercivity probe will be satisfied to give firm image in magnetically decoupled multilayer. By the way, the details of probe fabrication and analysis will discuss from next chapter.

Figure 5.6.3 and 5.6.4 are showing SEM, AFM and MFM analysis which have smaller dimension than 125 nm patterns array. The results are same as I mentioned before. No background noise after demagnetizing its field and probe works perfectly fine so far. However, probe sensitivity problem is occurring when probe scans smallest as like figure 5.6.5 and 5.6.6 patterns size. Not only matter of pattern size but also matters of the distance between dots also an important criterion to determine the probe's sensitivity.
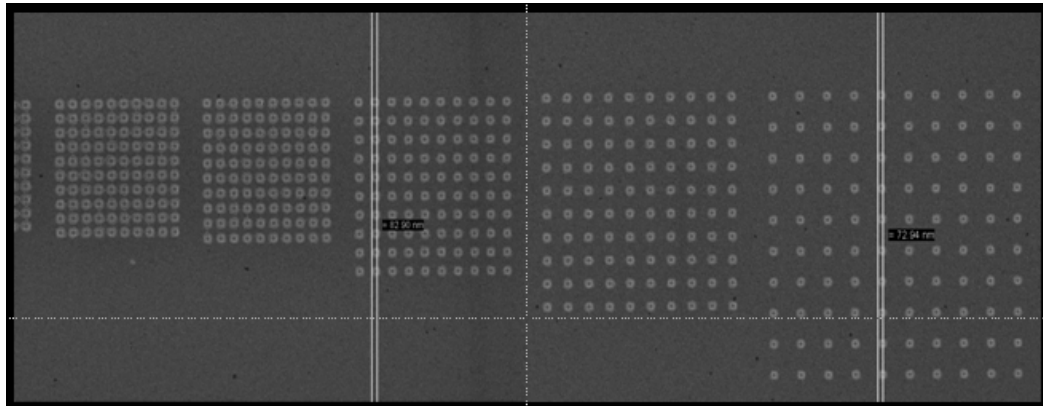
Figure 5.6.3: SEM image with around 70 nm pattern dimension. Distance of two dots are increasing from left to right.
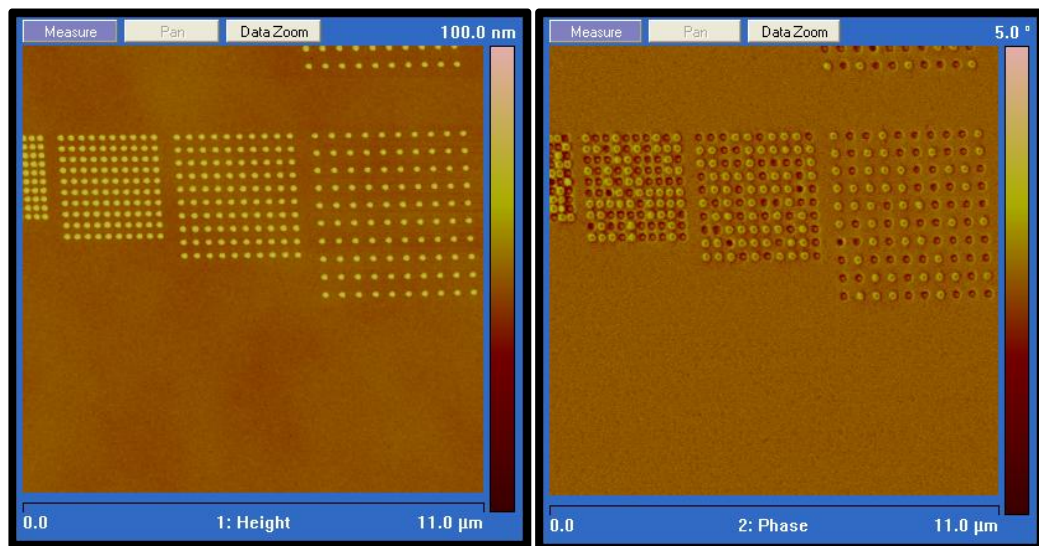
Figure 5.6.4: AFM and MFM analysis corresponding to figure 8.6.3. In MFM result, there are no background noise occurs after demagnetization processing.
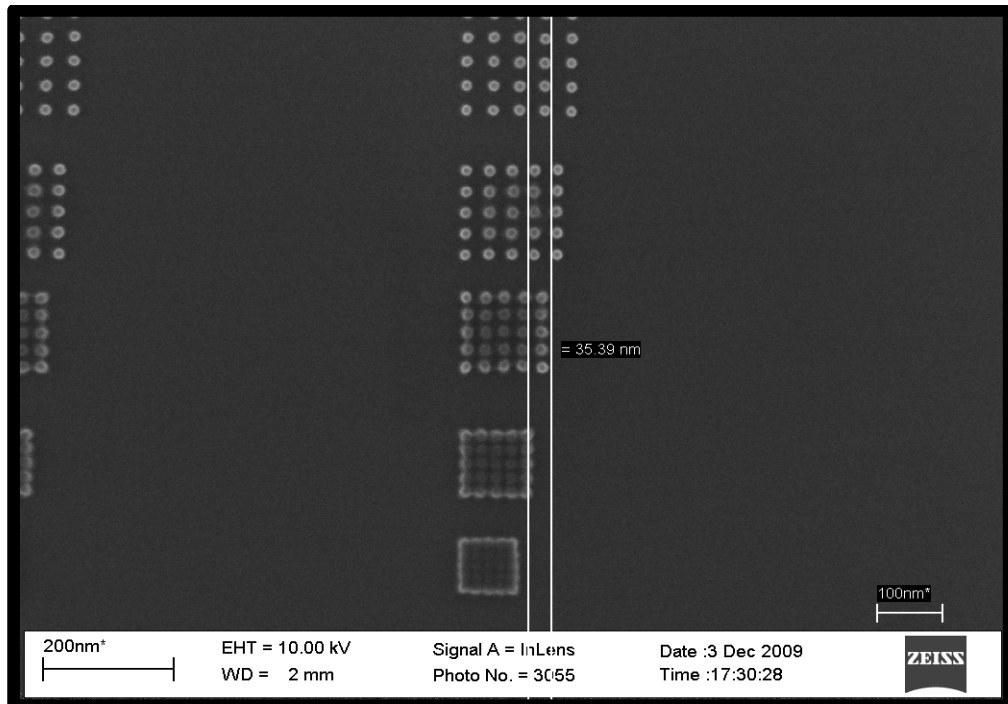
Figure 5.6.5: 5x5 array pattern for conducting the feasibility of high density magnetic patterns. Each dot dimension is less than 10 nm and dot-pitch is 35nm. It is able to record information around 750 Gbit/in².
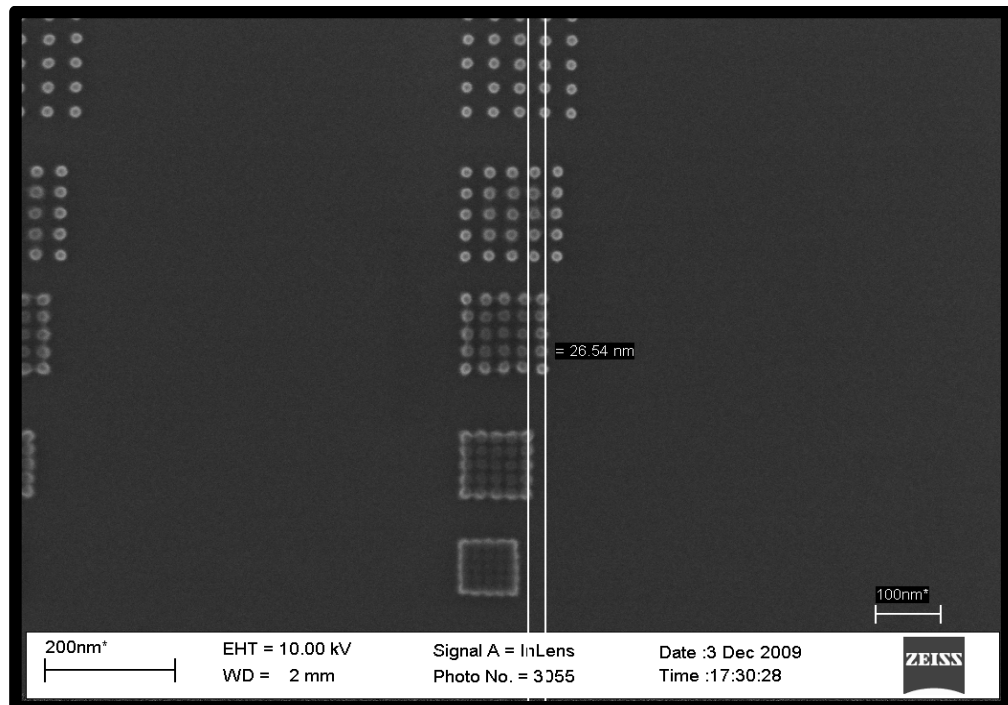
Figure 5.6.6: 5x5 array pattern for conducting the feasibility of high density magnetic patterns. Each dot dimension is less than 10 nm and dot-pitch is 27 nm. It is able to record information around 1 Tbit/in².

Figure 5.6.5 is 5x5 array pattern for conducting the feasibility of high density magnetic patterns. Each dot dimension is less than 10 nm and dot-pitch is 35nm. In that result, it is able to record information around 750 Gbit/in^2. Figure 5.6.6 is also same array pattern as previous image and this pattern size conduct the feasibility of high density magnetic patterns. Each dot dimension is less than 10 nm and dot-pitch is 27 nm. It is able to record information around 1 Tbit/in^2. According to those two results, negative tone resist is able to lithography high magnetic density and the possibility of storage is around 1 Tbit/in^2.

Chapter 6. Probe Fabrication for High Areal Density.

6.1 Motivation

For the necessity of addressing the fabrication and exploitation of ultrahigh coercivity magnetic force microscopy (MFM) probes is characterizing high-magnetic moment nanostructures and devices. Since its invention about three decades ago, magnetic force microscopy (MFM) has become a primary imaging technique to analyze sub-micrometer domains. Typically conventional MFM probes have been particularly influential in the analysis of magnetically recorded bits, their use in the analysis of fully energized modern magnetic transducers has been limited because of their relatively low coercivity. The magnetic field generated by modern magnetic transducers can reach more than 10 kOe at a distance less than a few nanometers above the write-pole tip. Therfore, the magnetization of the probe can change as it scans across an energized write-pole tip, making interpretation of the MFM images difficult.

It is not a first time to show relatively high-coercivity probes have been demonstrated. However, they have either not been tested on magnetic recording transducers or used only to evaluate transducers with dc currents up to 3 mA; meanwhile, modern magnetic recording transducers operate at write currents above 25 mA. Currently commercially available high-coercivity MFM probes are marketed with coercivity values higher than 5 kOe and are composed of FePt or CoPt with a thickness of 45 nm, such as the Asylum Research Magnetic Force Microscopy-High Coercivity probes. Similarly, MFM probes with coercivity greater than 5 kOe have been fabricated on

tip-less carbon nanocones, using FePt films [Chen 2009]. Liou and Yao [1998] present their experimental work on the development of high-coercivity MFM probes, using CoPt composition, but do not characterize the probe's coercivity or provide data for dc write currents higher than ±3 mA.

Liou [1997] have used superparamagnetic MFM tips to characterize magnetic transducers, but only for dc write current of 3 mA. Others have used FePt-based compositions to enhance the coercivity and/or lateral resolution of MFM probes via unconventional techniques, such as focused ion beam milling of FePt-coated plateau probes [Amos 2009], FePt/FeCo/FePt exchange-spring trilayer tips [Rheem 2005], and multi-domain MFM probes [Amos 2008]; Albeit, neither has demonstrated sufficient coercivity to analyze fully energized magnetic transducers. Hence, these probes may be limited in their usefulness for characterizing modern magnetic recording transducers.

6.2 Probe Fabrication

To attain coercivity larger than 10 kOe, the deposition conditions for FePt (55/45) L10 thin films are first optimized on silicon substrates. The composition and thickness of the adhesion (Ta), seed (CrRu and MgO), and magnetic layers along with the sputtering pressure (3–10 mTorr) and substrate temperature (500 °C–700 °C) of the magnetic layer are tuned for optimal results. Next, selected compositions are sputter deposited on several silicon probes in conjunction with silicon witness samples.

In this section, two types of newly developed MFM probes are presented: low moment (LM) with $\sim 2.3 \times 10^{-13}$ emu and extremely LM (ELM) with $\sim 4.5 \times 10^{-14}$ emu (80% less magnetic moment), both exhibiting coercivity larger than 11 kOe. The LM and ELM probes are composed of CrRu(15 nm)/MgO(6 nm)/FePt(25 nm) and CrRu(25 nm)/MgO(6 nm)/FePt(5 nm), respectively. The magnetic composition for the LM and ELM probes is deposited at 700 °C under 5 mTorr and at 500 °C under 10 mTorr, respectively. The incorporation of both CrRu and MgO to the compositions facilitates the L10 ordering of the FePt film. The L10 ordering was confirmed via X-ray diffraction analysis on the witness silicon samples. In order to estimate the magnetic moment of each type of MFM probe, the volume of the magnetic compositions is calculated based on the assumption of a semispherical active magnetic region and is then multiplied by an approximated composition magnetization (MS) of ~ 750 emu·cm^{-3}. The calculations are based on an initial radius of curvature (ROC) of 10 nm for the silicon probes. The volume integration starts from the seed layer ROC ($R1$) and ends on the magnetic layer ROC ($R2$),

95

resulting in the following formulation: $m_{tot} \sim 2\pi/3(R_{32} - R_{31})\ M_S$, where m_{tot} is the total calculated magnetic moment. The first selected composition has a coercivity of about 10.5 kOe for the out-of-plane direction, as measured by vibrating sample magnetometer on a witness silicon substrate. To determine their coercivity, the probes are saturated in one direction and used to take a reference image of a demagnetized perpendicular bit patterned media (BPM). The probes are then removed from system, subjected to an applied magnetic field of 1 kOe in the reverse direction, and another MFM image of the BPM is taken for comparison with the reference. The process is repeated for increasing applied magnetic fields until the color coding of the MFM image inverts, an indication that the magnetization of the probes has switched. This technique is conducted to characterize both the newly developed and commercially available MFM probes from Nanosensors (NS), the point probe plus–LM–MFM–reflex coating (PPP-LM-MFMR) probes. Atomic force microcopy (AFM) and MFM imaging is performed using a dimensions 3100 scanning probe microcopy system by Veeco Instruments. The tapping/lift-mode technique is applied for all MFM imaging. The phase shift in the mechanical response of the probe, due to probe–sample interaction, is monitored. The lift-start/lift-scan heights are set to 50/30 and 50/10 nm for the BPM and magnetic writer analysis, respectively. The resonance frequency of the cantilevers is around 70 kHz with a force constant of $\sim$2.8 N/m.
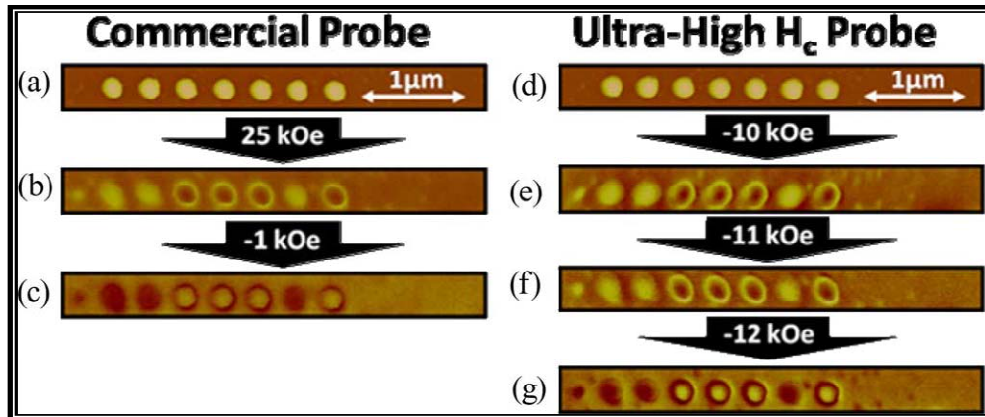
Figure 6.2.1: On the left, coercivity field analysis of a conventional MFM probe by NS: (a) AFM image of a series of seven magnetic bits, taken with the NS MFM probe, (b) MFM images of the magnetic bits after applying a magnetic field of 25 kOe, (c) and −1 kOe along the probe's axis of symmetry. On the right, coercivity field analysis of the newly developed LM-UHC MFM probe: (d) AFM image of the same series of magnetic bits as shown on the left, taken with the LM-UHC MFM probe, (e) MFM images of the magnetic bits after applying a magnetic field of −10 kOe, (f) −11 kOe, (g) and −12 kOe along the probe's axis of symmetry.

6.2.1 Probes' Coercivity Analysis

First, the coercivity of the NS MFM probes is investigated. One of the probes is magnetized along its axis of symmetry with a magnetic field of ∼25 kOe, followed by AFM/MFM imaging of the BPM [see Fig. 6.2.1(a) and (b)]. The MFM image shown in Fig. 6.2.1(c) is performed after a magnetic field of 1 kOe has been applied in the reverse direction. As is clearly evident from the MFM images, the magnetization of the commercial MFM probe is already reversed by a magnetic field of 1 kOe. Similar results are obtained for four other NS MFM probes. Next, the coercivity of the newly developed MFM probes is determined by the same technique. Since the coercivity in the out-of-plane direction of the FePt thin-film composition on silicon witness samples has been measured to be higher than 10.5 kOe, the incremental magnetic field analysis starts from a magnetic field of 10 kOe. To avoid redundancy, the MFM image taken after the probe was saturated with a magnetic field of 25 kOe is

omitted. Fig. 6.2.1(e)–(g) reveals that the coercivity of the newly developed MFM probes lies between 11 and 12 kOe, at least an order of magnitude higher than the coercivity of the commercially available MFM probes. Similar results are obtained for four other probes. Hence, from here on these probes will be referred to as LM-UHC MFM probes. To summarize, the commercially available NS MFM probes are suited for analyzing magnetic structures that emanate less than 1 kOe of stray magnetic fields. On the other hand, the newly developed LM-UHC MFM probes can be used to investigate specimens that emanate stray magnetic fields higher than 11 kOe and are therefore suitable for characterizing fully energized modern perpendicular magnetic recording writers.
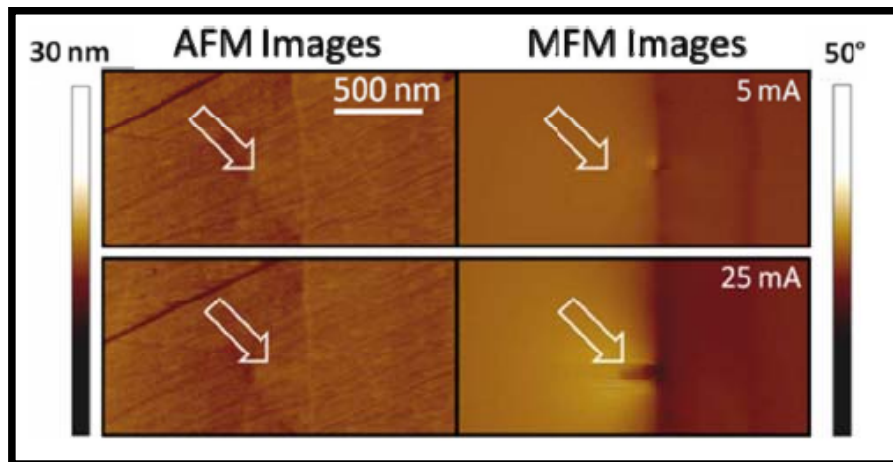
Figure 6.2.2: MFM analysis of a modern perpendicular magnetic transducer, using a commercially available MFM probe by Nanosensors. The white arrows print to the location of the write –pole tip
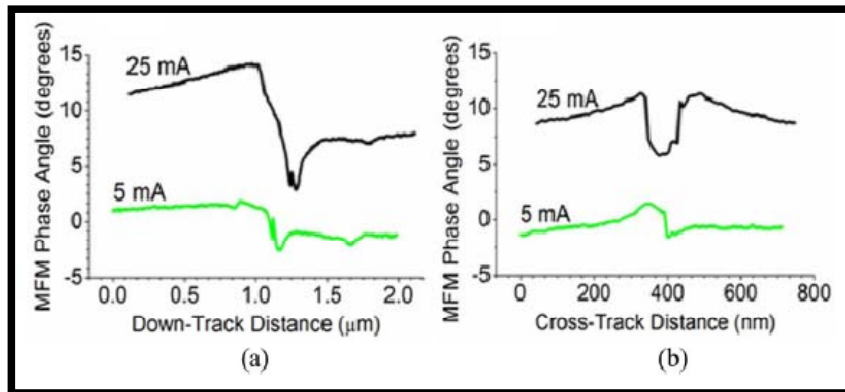
Figure 6.2.3 : MFM line scans along the write pole tip (a) down track and (b) cross track directions. Both graphs reveal the switching of the probe's magnetization as the probe scans above the write pole tip.

6.2.2 Modern Magnetic Recording Transducer Analysis

The commercial and LM-UHC MFM probes have been used to analyze a modern perpendicular magnetic writer by performing head saturation and remanence tests on a shielded write pole tip [Kanai 2003, Xiao 2005]. The transducer exhibits both a front magnetic shield and a trapezoidal write-pole tip. The front shield contributes to a larger magnetic field gradient and a better magnetic field angle for sharper bit transitions and improved grain switching, respectively [Mallary 2002]. The trapezoidal shape of the write-pole tip eliminates the erasure of adjacent tracks when recording at relatively large skew angles, resulting in higher magnetic tracks density [Ito 2002, Kanai 2007]. The MFM probes by NS are initially used to perform a writepole saturation test. The saturation test is most commonly performed using a spinstand system with which various signal parameters are analyzed as a function of applied write currents. For example, the write currents may be varied from 1 to 45 mA, while the average giant or tunneling magnetoresistance readback signal of a recorded track is measured for each write current step. A plot of the write current versus the

99

average readback SNR is generated. In most cases, the write current at which the SNR plateaus is considered the saturation current of the magnetic transducer under investigation. As can be seen from Fig. 6.2.2, a write current of only 5 mA is already sufficient to generate magnetic stray fields greater than the coercivity of the NS probe, and therefore the magnetization of the probe switches right when the probe is scanning above the write-pole tip. For the 25 mA write current, an even more pronounced magnetization switching of the probe is evident when the probe reaches the region of the write-pole tip. MFM line scans along the write-pole tip down-track and cross-track directions further emphasize the magnetization switching of the probe [see Fig. 6.2.3 (a) and (b)]. The probe is thus unsuitable for characterizing dc energized magnetic transducers. The newly developed LM-UHC MFM probes are then used to perform the same saturation test with dc write currents ranging from 0–45 mA. As can be seen from Fig. 6.2.4, the probe maintains its polarization of magnetization throughout the entire test. When the dc write current polarity is changed from 45 to −45 mA [see Fig. 6.2.4 (h) and (i)], only the color coding of the MFM image is inverted; hence, reaffirming that the probe exhibits high anisotropy and high coercivity. In order to accurately determine the minimum dc write current that is required to saturate the write-pole tip, the MFM response is plotted for different dc write currents along two orthogonal lines: (a) cross-track is marked with a black-dotted line and (b) down-track is marked with a red-dotted line [see Fig. 6.2.4(h)]. For the down-track analysis, the phase difference between the minimum and maximum of each MFM line scan is measured and then compared [see Fig. 6.2.5(a)]. For the cross-track direction, the full-width–halfmaximum (FWHM) is measured for each MFM line scan and then compared [see Fig. 6.2.5(b)]. The MFM line-scan

investigation of both directions reveals that the maximum force interaction between the MFM probe, and hence the maximum magnetic field of the write-pole generates, occurs for dc write currents above 25 mA. Consequently, the MFM images for the dc write currents between 25 and 45 mA have been omitted from the presented figures and MFM line scans. Two standard parameters in the characterization of modern magnetic recording transducers are the distance along the down-track direction (connecting the write-pole tip and the front shield) at which the magnetic recording field drops from a maximum to a minimum and the FWHM of the magnetic field profile along the cross-track direction at the recording side of the writepole tip. The former relates to the sharpness of bit transitions and the latter to the track width. Minimization of both parameters is vital for higher density magnetic recording. The MFM line scans for the write current of 45 mA shows that for the particular head under investigation, the magnetic gradient distance along the down-track direction is ～75 nm, and the FWHM of the magnetic field profile along the cross-track direction is～120 nm.
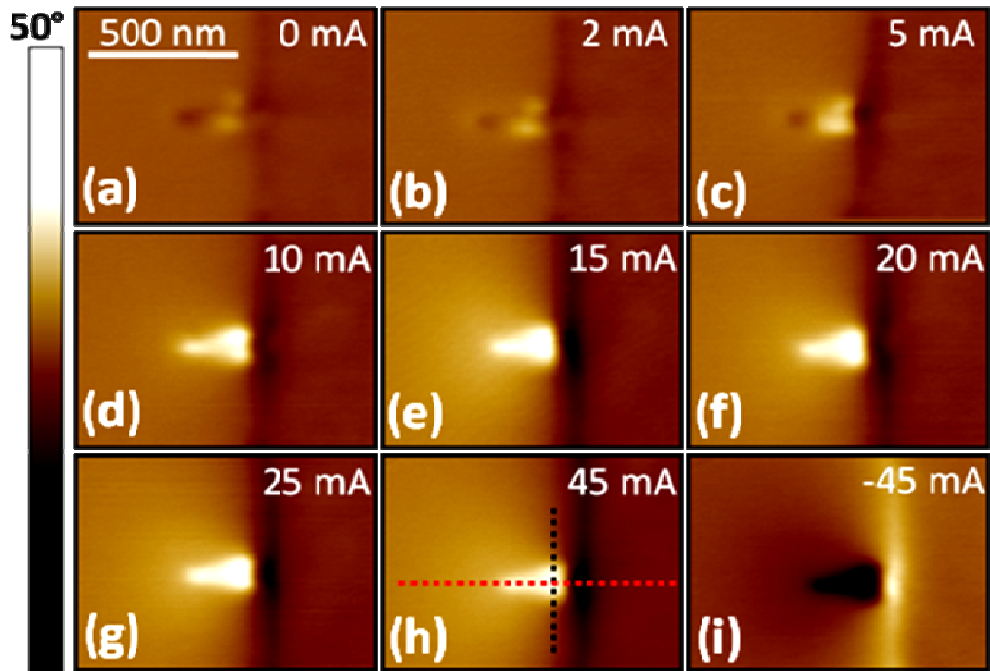
Figure 6.2.4: MFM analysis of a modern perpendicular magnetic transducer, using the newly developed UHC-LM MFM probe. The sequence of MFM images has been taken to perform a write-pole saturation test by applying a range of dc write currents.

Figure 6.2.5: MFM line scans of the write-pole tip taken along its (a) downtrack direction and (b) cross-track direction. The magnetic gradient distance between the write-pole and front shield is ～75 nm, and the FWHM of the magnetic field profile is ～120 nm.

Conclusion

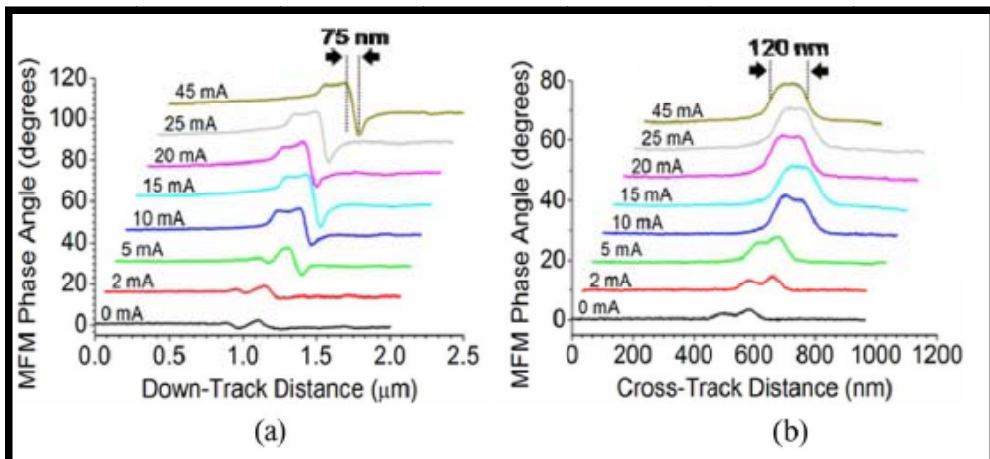In this dissertation, I give an outline of four categories for realizing the hard magnetic disk drive system with high areal density. First, I mention the general concepts as the history of hard disk drive from the initiative to the future prediction, the market trend and the real world's demanding of and secondly, I discuss the reason of selecting lithography method with direct electron beam, the basic physical phenomena in electron, and the general knowledge in mechanical background of electron beam lithography equipment. Next, investigate optimal magnetic materials within various circumstances including, pressure, magnetization in in-plane and out-of-plane and so on. And characterize lithographic optimal condition including of finding proper resist and adequate condition such as step height and various constraints tendency, dosage versus dimension versus distance, and dosage versus exposing area changing and so on. Based on those two optimal conditions, I experimentally realize high areal density with 3 dimensional magnetic multilayers and present all result with SEM, AFM, MFM, MOKE and VSM. During proceeding tangible experiments, my group invented new probe in order to perform high sensitivity and high coercivity probe.

References

[1] www.intel.com

[2] G. Moore, "Cramming more components onto integrated circuits", Electronics, 38, 8, 1965.

[3] The International Technology Roadmap for Semiconductors (ITRS) annual report – 2009

[4] Robert E. Rottmayer, Sharat Batra, Dorothea Buechel, William A. Challener, Julius Hohlfeld, Yukiko Kubota, Lei Li, Bin Lu, Christophe Mihalcea, Keith Mountfield, Kalman Pelhos, Chubing Peng, Tim Rausch, Michael A. Seigler, Dieter Weller, and XiaoMin Yang, "Heat-Assisted Magnetic Recording", IEEE Transaction onMagnetics, Vol. 42, no. 10, 2006.

[5] A. Lyberatos and J. Hohlfeld, "Model of thermal erasure in neighboring tracks during thermomagnetic writing," *J. Appl. Phys.*, vol. 95, no. 4, pp. 1949–1957, 2004.

[6] T. W. McDaniel, "Ultimate limits to thermally assisted magnetic recording," J. Phys.: Condensed Matter, vol. 17, no. 7, pp. R315–R332, Feb. 23, 2005.

[7] S. Batra,W. Scholz, and T. Roscamp, "Effect of thermal fluctuation field on the noise performance of a perpendicular recording system," *Jpn. J.Appl. Phys*, vol. 99, pp. 1-1–1-3, 2006.

[8] Maik Duwensee, Shoji Suzuki, Judy Lin, David Wachenschwanz, and Frank E. "Air Bearing Simulation of Discrete Track Recording Media", IEEE Transaction on Magnetics, vol. 42, no. 10 2006

[9] T. McDaniel, W. Challener, "Issues in heat-assisted perpendicular recording." IEEE Transaction on Magnetics. 39, 4, 1972-1979, 2003.

[10] Maik Duwensee, Shoji Suzuki, Judy Lin, David Wachenschwanz, and Frank E. Talke, "Air Bearing Simulation of Discrete Track Recording Media", IEEE Transactions on Magnetics, vol. 42, no, 10, 2006.

[11] S. Y. Chou, P. R. Krauss, P. J. Renstrom, "Imprint of sub 25nm vias and trenches in polymers", *Appl. Phys. Lett.* **1995**, *67*, 3114.

[12] Peter R. Kraussa and Stephen Y. Chou, "Nano-compact disks with 400 Gbit/in2 storage density fabricated using nanoimprint lithography and read with proximal probe", Appl. Phys. Lett. **71** (21), 24 November 1997

[13] L. Jay Guo, "Nanoimprint Lithograhy: Methods and Materials Requirements.". Adv. Matter, 19, 495-513, 2007.

[14] S. Y. Chou, P. R. Krauss, and P. J. Renstrom, "Imprint Lithography with 25-Nanometer Resolution"Science **272**, 85, 1996.

[15] S. Y. Chou, P. R. Krauss, and P. J. Renstrom,"Nanoimprint lithography" J. Vac. Sci. Technol. B 14, 4129, 1996.

[16] S Zankovych, T Hoffmann, J Seekamp, J-U Bruch and C M Sotomayor Torres, "Nanoimprint lithography: challenges and prospects.", Nanotechnology 12, 91–95, 2001.

[17] M. Albrecht, C. T. Rettner, A. Moser, M. E. Best, and B. D. Terris, "Recording performance of high-density patterned perpendicular media," Appl. Phys. Lett. 81 (15), 2875-7 (2002)

[18] O. Hellwig, J.K. Bosworth, E. Dobisz, D. Kercher, T. Hauet, G. Zeltzer, J. D. Risner-Jamtgaard, D. Yaney, and R. Ruiz, "Bit patterned media based on block copolymer directed assembly with narrow magnetic switching field distribution" APL, 96,052511, 2010

[19] Joan K. Bosworth, Elizabeth Dobisz and Ricardo Ruiz, " 20 nm Pitch Directed Block Copolymer Assembly Using Solvent Annealing for Bit Patterned Media" J of Photopolymer science and technology, Vol 23,2, 2010

[20] R. E. Fontana, Jr., S. A. MacDonald, H. A. A. Santini, C. Tsang, "Process consideration for critical features in high areal density thin film magnetoresistive heads: a review," IEEE Trans. Magn., vol. 35, no. 2, p. 806, 1998.

[21] www.hgst.com, - annual report "Density Multiplication and improved lithography by Direct block copolymer assembly for patterned media at 1 Tbit/in^2 and beyond" 2009.

[22] E. Grochowski, R. D. Halem, "Technological impact of magnetic hard disk drives on storage systems.", IBM systems journal, vol 42, no 2, 2003.

[23] "IBM Archives: IBM 350 disk storage unit". Retrieved 2007.

[24] M. Yu, Y. L, A. Moser D. Weller, and D. J. Sellmye, "Nanocomposite CoPt:C films for extremely high-density recording", APL, vol 75, no 25, 1999.

[25] S. N. Piramanayagam, ' Perpendicular recording media for hard disk drives", JAP 102, 011301, 2007.

[26] D. A. Thompson, J. S. Best, "The future of magnetic data storage technology", IBM J. RES. Dev. vol. 44, no. 3, 2000.

[27] S.N. Piramanayagam, K. Srinivasan, "Recording media research for future hard disk drives", Journal of Magnetism and Magnetic Materials 321, 485– 494, 2009.

[28] Vassil Skumryev, Stoyan Stoyanov, Yong Zhang, George Hadjipanayis, Dominique Givord and Josep Nogués, "Beating the superparamagnetic limit with exchange bias" Nature 423, 850-853, 2003.

[29] S. Khizroev and D. Litvinov, "Perpendicular magnetic recording: Writing Processing ", J. Appl. Phys. 95, 4521, 2004.

[30] D. Litvinov and S. Khizroev, "Perpendicular magnetic recording: PlayBack", J. Appl. Phys. 97, 071101, 2005.

[31] D. Litvinov and S. Khizroev, "Perpendicular Magnetic Recording" Kluwer Academic, Dordrecht, 2005.

[32] C. Davisson, L.H. Germer "Diffraction of electrons by a crystal of nickel". Physical Review **30** (6): 705–740, 1927.

[33] W.L. Bragg, "The Diffraction of Short Electromagnetic Waves by a crystal", Proceedings of the Cambridge Philosophical Society, 17, 43–57, 1913.

[34] Reimer, "Scanning Electron Microscopy,", Springer-Verlag, Berlin, 1985.

[35] A. N. Broers, J. M. E. Harper, and W. W. Molzen, "250 A linewidths with PMMA electron resist" APL 33, 392, 1978.

[36] James S. Greeneich, "Solubility rate of Poly-Methl Methacrylate), PMMA, electron-resist", Journal of Electrochem. Soc.: Solid-state science and technology, vol, 121, 12, pp. 1669-1671, 1974.

[37] F. De Carlo, D.C. Mancini, B. Lai, J.J. Song, "Characterization of exposure and processing of thick PMMA for deep x-ray lithography using hard x-rays", Microsystem Technologies 4, 86-88,, 1998.

[38] J.S. Jeng, .S. Chen, "The comparative study of thermal stability among silicon dioxide, fluorinated silicate glass, hydrogen silsesquioxane, and organosilicate glass dielectrics on silicon", Thin Solid Films 516, 6013–6019, 2008.

[39] Reynard, J, "Integration of fluorine-doped silicon oxide in copper pilot line for 0.12-μm technology". Microelectronic Engineering **60,** 113, 2002.

[40] Anda E.Grigorescu, Marco C. van der Krogt, Cees W. Hagen, "Sub-10 nm structures written in ultra-thin HSQ resist layers, using Electron Beam Lithography", Proc. of SPIE Vol. 6519, 65194A, 2007

[41] http://www.microchem.com/products/pdf/PMMA_Data_Sheet.pdf

[42] In-Bok Baek, Jong-Heon Yang, Won-Ju Cho, Chang-Geun Ahn, Kiju Im, and Seongjae Lee "Electron beam lithography patterning of sub-10 nm line using hydrogen silsesquioxane for nanoscale device applications", J. Vac. Sci. Technol. B **23**, 3120, 2005

[43] R. Tiron and L. Mollard et al "Ultrahigh-resolution pattern using electron-beam lithography HF wet etching", J. Vac. Sci. Technol. B 25,4, 2007

[44] Haifang Yang,Aizi Jin, Qiang Luo,Junjie Li,Changzhi Gu, Zheng Cui,"Electron beam lithography of HSQ/PMMA bilayer resists for negative tone lift-off process", Microelectronic Engineering 85, 814–817, 2008

[45] M. H. Kryder, E. C. Gage, T. W. McDaniel, W. A. Challener, R. E. Rottmayer, G. Ju, Y.-T. Hsia, M.F. Erden, "Heat Assisted Magnetic Recording," IEEE Trans. Mag., **96** (11),1810-35, 2008.